

**UNIVERSITY OF CALIFORNIA,  
IRVINE**

“Development and Verification of a Steady-State Internal Reforming Molten  
Carbonate Fuel Cell Model for Tri-generation of Hydrogen, Electricity, and Heat”

**THESIS**

submitted in partial satisfaction of the requirements  
for the degree of

**MASTER OF SCIENCE**

in Civil and Environmental Engineering

by

Roxana Bekemohammadi

Thesis Committee:

Professor Jacob Brouwer, Chair

Professor Scott Samuelsen

Professor Diego Rosso

**2013**

UMI Number: 1547267

All rights reserved

INFORMATION TO ALL USERS

The quality of this reproduction is dependent upon the quality of the copy submitted.

In the unlikely event that the author did not send a complete manuscript and there are missing pages, these will be noted. Also, if material had to be removed, a note will indicate the deletion.



UMI 1547267

Published by ProQuest LLC (2013). Copyright in the Dissertation held by the Author.

Microform Edition © ProQuest LLC.

All rights reserved. This work is protected against unauthorized copying under Title 17, United States Code



ProQuest LLC.  
789 East Eisenhower Parkway  
P.O. Box 1346  
Ann Arbor, MI 48106 - 1346

© 2013 Roxana Bekemohammadi

## DEDICATION

To my extraordinary mother

## TABLE OF CONTENTS

LIST OF FIGURES .....	VIII
LIST OF TABLES .....	XI
ABBREVIATIONS .....	XIV
SYMBOLS.....	XVIII
ACKNOWLEDGEMENTS.....	XXII
ABSTRACT OF THESIS.....	XXIV
CHAPTER 1: INTRODUCTION .....	2
1.1 Overview.....	2
1.2 Motivation.....	6
1.3 Goals .....	8
1.4 Objectives .....	9
CHAPTER 2: BACKGROUND AND LITERATURE REVIEW .....	10
2.1 Basic Operation of Hydrogen Fuel Cells .....	10
2.2 Reversible Fuel Cell Voltage .....	11
2.2.1 Fuel Cell Thermodynamics.....	11
2.2.2 Standard-State Reversible Fuel Cell Voltage .....	16
2.2.3 Nernst Equation: Reversible Fuel Cell Voltage Variation with Concentration and Pressure .....	18

2.3	Fuel Cell Types .....	20
2.4	High-Temperature Fuel Cells .....	23
2.4.1	Molten Carbonate Fuel Cells .....	24
2.5	Hydrogen Production Methods .....	26
2.5.1	Steam-Methane Reforming .....	26
2.5.2	Steam-Methane Reforming Chemistry .....	26
2.5.3	Centralized Steam Methane Reforming .....	27
2.5.4	Water-Gas Shift .....	28
2.6	Hydrogen Separation Technologies .....	29
2.6.1	Pressure Swing Adsorption .....	29
2.7	Tri-Generation of Hydrogen, Electricity, and Heat Using a Fuel Cell .....	30
2.7.1	Previous Research .....	31
2.7.2	Hydrogen Energy Station .....	32
2.7.3	Hydrogen Energy Station Demonstration at Orange County Sanitation District ..	33
2.8	Summary .....	36
Chapter 3: Approach .....		38
Chapter 4: Model Development .....		41
4.1	Process Simulation .....	43
4.2	Process Description .....	47

4.3	Process Models .....	53
4.3.1	Molten Carbonate Fuel Cell.....	53
4.3.1.1	Internal Reformation.....	54
4.3.1.2	Thermal Management of Fuel Cell Stack .....	56
4.3.1.3	Pre-Reformer Model .....	58
4.3.1.4	Simplified Fuel Cell Stack Model.....	60
4.3.1.5	Indirect Internal Reformation Model .....	62
4.3.1.6	Direct Internal Reformation Model .....	63
4.3.1.7	Previous Research: Fuel Cell Modeling using Aspen Plus® .....	64
4.3.1.8	Anode Discretization .....	65
4.3.1.9	Electrochemistry .....	67
4.3.1.10	Voltage.....	73
4.3.1.11	Power Generation and Parasitic Loads .....	78
4.3.2	Hydrogen Concentrator Unit (HCU) .....	82
4.3.3	Hydrogen Separation Unit (HSU).....	84
4.3.3.1	Syngas Compressor.....	86
4.3.3.2	Electric Chillers .....	88
4.3.3.3	Pressure Swing Adsorption (PSA) System.....	91
4.4	Efficiency of Tri-Generating High-Temperature Fuel Cell.....	93

Chapter 5: Model Verification .....	95
5.1 Verification of FuelCell Energy Direct FuelCell® Model .....	96
5.2 Verification of Tri-generating FuelCell Energy Direct FuelCell® .....	102
5.2.1 Verification of Tri-generating Direct FuelCell® using Natural Gas .....	102
5.2.2 Verification of Tri-generating Direct FuelCell® using Anaerobic Digester Gas .....	113
Chapter 6: Model Evaluation .....	124
6.1 Nernst Voltage .....	128
6.2 Voltage Losses .....	130
6.3 Fuel Cell Operating Voltage .....	136
6.4 Gross Power .....	138
6.5 Parasitic Loads .....	140
6.6 Net Power .....	146
6.7 Hydrogen Production Rate .....	149
6.8 Waste Heat Availability .....	150
6.9 Electrical Efficiency .....	154
6.10 Hydrogen Production Efficiency .....	157
6.11 Combined Hydrogen and Power Efficiency .....	160
Chapter 7: Discussion .....	163
Chapter 8: Summary .....	169



Chapter 9: Conclusions .....	170
Chapter 10: Recommendations for Future Work.....	173
Bibliography .....	174

## LIST OF FIGURES

Figure 1. Generic fuel cell representation[16] .....	10
Figure 2. Molten carbonate fuel cell. ....	24
Figure 3. Process flow diagram of the installed tri-generation system.....	35
Figure 4. Scope of tri-generation model .....	42
Figure 5. U.S. patent application drawing of tri-generating HTFC system coupled with a hydrogen utilization device [28] .....	48
Figure 6. General process flow diagram of modeled tri-generation system .....	51
Figure 7. FuelCell Energy Direct FuelCell <sup>®</sup> stack design [41].....	55
Figure 8. Reaction chemistry in an internal reforming molten carbonate fuel cell .....	57
Figure 9. Schematic of non-uniform catalyst distribution along the length of an anode.....	58
Figure 10. FuelCell Energy DFC <sup>®</sup> stack design shown for a single group of fuel cells.....	61
Figure 11. DFC <sup>®</sup> design simplified as single fuel cell grouped with reforming unit .....	62
Figure 12. Hydrogen concentrator unit modeled in Aspen Plus <sup>®</sup> .....	83
Figure 13. Aspen Plus <sup>®</sup> model of the hydrogen separation unit.....	85
Figure 14. Two-stage compressor with water-cooling modeled in Aspen Plus <sup>®</sup> .....	86
Figure 15. Electric chiller refrigeration cycle modeled in Aspen Plus <sup>®</sup> .....	89

Figure 16. Pressure sing adsorption system modeled in Aspen Plus® .....	92
Figure 17. The fuel cell voltage dependence on current density for NG operation.....	112
Figure 18. The fuel cell voltage dependence on current density for ADG operation.....	122
Figure 19. Nernst voltage for eight cases at varying fuel utilization .....	128
Figure 20. Cathode polarization for tri-generation fuel cell system at various fuel utilizations and hydrogen recovery percentages.....	131
Figure 21. Anode polarization for tri-generation fuel cell system at various fuel utilizations and hydrogen recovery percentages.....	133
Figure 22. Total polarization losses for modeled scenarios at varying fuel utilizations.....	135
Figure 23. Fuel cell operating voltage for varying fuel utilizations for eight tri-generation cases .....	137
Figure 24. Gross power generation for tri-generating MCFC at various fuel utilizations.....	138
Figure 25. Gross power generation for tri-generating MCFC at 0.6 to 0.7 fuel utilization.....	139
Figure 26. HSU load for varying fuel utilizations and hydrogen recovery percentages.....	141
Figure 27. mBOP load for varying fuel utilizations and hydrogen recovery percentages.....	143
Figure 28. mBOP load for fuel utilizations between 0.6 and 0.7.....	144
Figure 29. DC—AC conversion load for varying fuel utilizations and hydrogen recovery.....	145

Figure 30. DC—AC conversion load for 0.6—0.7 fuel utilization .....	146
Figure 31. Net power for varying fuel utilizations for eight tri-generation cases.....	147
Figure 32. Net power production for 0.6—0.7 fuel utilization.....	148
Figure 33. Hydrogen production rate for tri-generating MCFC at varying fuel utilizations .....	149
Figure 34. Available waste heat generated by tri-generating fuel cell system .....	151
Figure 35. Electrical efficiency for each scenario for various fuel utilizations .....	155
Figure 36. Hydrogen production efficiency for each scenario for various fuel utilizations .....	158
Figure 37 Combined hydrogen and power production efficiency for various fuel utilizations..	161

## LIST OF TABLES

Table 1. Coefficients for molar heat capacity expression in Equation (2-9). .....	14
Table 2. Molar enthalpy of formation and entropy values at standard temperature of 298.15 K. 15	
Table 3. Distinguishing characteristics of five major fuel cell types.....	21
Table 4. Applications, advantages, and disadvantages of five major fuel cell types.....	22
Table 5. Operating temperature classification of five major fuel cell types.....	22
Table 6 Aspen Plus <sup>®</sup> unit operation models .....	44
Table 7. Reactions accounted for in the IIR equilibrium reactor.....	59
Table 8. List of IHI 10-kW molten carbonate fuel cell stack components and materials [47].....	74
Table 9. Values of parameters appearing in empirical polarization equations [47] .....	78
Table 10. Aspen Plus <sup>®</sup> process unit models used to model the hydrogen concentrator unit .....	84
Table 11. Aspen Plus <sup>®</sup> process unit models used to model the two-stage syngas compressor.....	88
Table 12 Aspen Plus <sup>®</sup> process unit models used to model the electric chillers .....	90
Table 13. Aspen Plus <sup>®</sup> process unit models used to simulate the PSA unit .....	93
Table 14. Operating properties for DFC <sup>®</sup> verification.....	98
Table 15. Input stream conditions for DFC <sup>®</sup> verification.....	98
Table 16. Input stream composition for verification of DCF <sup>®</sup> model .....	99

Table 17. Measured and modeled stream compositions for anode exhaust.....	100
Table 18. Measured and modeled stream compositions for cathode exhaust.....	101
Table 19. Model operating conditions for tri-generation fuel cell using natural gas.....	103
Table 20. Input stream conditions for tri-generation fuel cell using natural gas .....	104
Table 21. Input stream composition for verification of tri-generating DCF <sup>®</sup> model operating on natural gas .....	104
Table 22 Measured and modeled anode exhaust composition for natural gas case.....	105
Table 23. Composition of measured and modeled HTS reactor exhaust.....	106
Table 24. Modeled inlet and outlet HTS molar flow rate of species .....	107
Table 25. Measured and modeled exhaust composition of LTS reactor.....	108
Table 26. Modeled inlet and outlet LTS molar flow rate of species.....	109
Table 27. Measured and modeled cathode exhaust molar flow rate and percent error .....	110
Table 28. Measured and modeled voltage and power of the tri-generation system using NG ...	113
Table 29. Model operating conditions for tri-generation fuel cell using ADG .....	114
Table 30. Input stream conditions for tri-generation fuel cell using ADG.....	115
Table 31. Input stream composition for tri-generating DCF <sup>®</sup> model operating on ADG.....	115
Table 32 Measured and modeled anode exhaust composition for ADG case .....	116

Table 33. Composition of measured and modeled HTS reactor exhaust.....	117
Table 34. Measured and modeled exhaust composition of LTS reactor.....	118
Table 35 Measured and modeled cathode inlet composition and associated percent error .....	119
Table 36. Measured and modeled cathode inlet composition and percent error .....	120
Table 37. Measured and modeled voltage and power for tri-generation system using ADG.....	123
Table 38. List of scenarios resulting from parametric studies .....	126
Table 39. Operating conditions for parametric studies of tri-generating fuel cell.....	127
Table 40. Input stream conditions for parametric studies of a tri-generating fuel cell.....	127
Table 41. Range of fuel utilizations for thermally balancing tri-generation fuel cell system ....	152
Table 42. Fuel utilization for optimal electrical efficiency.....	156
Table 43. Fuel utilization for optimal hydrogen production efficiency.....	159
Table 44. Minimum Fuel utilization for optimal hydrogen production efficiency.....	163
Table 45. Optimal operating fuel utilization for different system outcomes .....	166
Table 46. Range of fuel utilizations for modeled scenarios.....	167
Table 47. Hydrogen, electricity, and heat generation for operating fuel utilization range .....	168

## ABBREVIATIONS

A	Amperes
ADG	Anaerobic Digester Gas
AGO	Anodic Gas Oxidizer
APCI	Air Products and Chemicals, Incorporated
BOP	Balance-of-Plant
B-V	Butler-Volmer
C	Celsius
CA	California
CHP	Combined Heat and Power
CNG	Compressed Natural Gas
CO	Carbon Monoxide
CO <sub>2</sub>	Carbon Dioxide
DFC <sup>®</sup>	Direct FuelCell <sup>®</sup>
DG	Distributed Generation
DIR	Direct internal Reformation



DOE	Department of Energy
EHS	Electrochemical Hydrogen Separator
EPA	Environmental Protection Agency
FCE	FuelCell Energy
GHGs	Greenhouse Gases
GW	Gigawatt
H <sub>2</sub>	Hydrogen
H <sub>2</sub> O	Water
H <sub>2</sub> ES	Hydrogen Energy Station
HEX	Heat Exchanger
HHV	Higher Heating Value
HSMR	Hydrogen Separation Membrane Reactor
HSU	Hydrogen Separation Unit
HTFC	High-Temperature Fuel Cell
HTS	High-Temperature Shift
IIR	Indirect Internal Reformation

kW	Kilowatts
kWh	Kilowatt-Hour
LCA	Life Cycle Analysis
LHV	Lower Heating Value
LTS	Low-Temperature Shift
mBOP	Mechanical Balance-of-Plant
MCFC	Molten Carbonate Fuel Cell
MPa	Megapascal
NFCRC	National Fuel Cell Research Center
NO <sub>x</sub>	Nitric Oxides
OCV	Open Circuit Voltage
OCSD	Orange County Sanitation District
PSIA	Pound-force per Square Inch, Absolute
PSIG	Pound-force per Square Inch, Gauge
PSA	Pressure Swing Adsorption
RU	Reformer Unit

S/C	Steam-to-Carbon Ratio
SMR	Steam-Methane Reforming
SOFC	Solid Oxide Fuel Cell
SO <sub>x</sub>	Sulfur Oxides
WGS	Water-Gas Shift

## SYMBOLS

$\mu$	Chemical Potential
$A_{cell}$	Active area of a single fuel cell
$A_{stack}$	Active area of the fuel cell stack
$a$	Activity
$c$	Concentration
$D$	Diffusivity
$E$	Nernst voltage
$E_e$	Electric field
$e^-$	Electrons
$\varepsilon$	Effectiveness
$\varepsilon_{DC-AC}$	DC-AC converter efficiency
$E_a$	Activation energy
$E^o$	Open circuit voltage
$F$	Fuel
$F$	Faraday's constant

$G$	Gibbs free energy
$H$	Enthalpy
$H_f$	Enthalpy of formation
$H_2$	Hydrogen product
$i$	Electric current
$j$	Current density
$\dot{n}$	Molar flow rate
$n_c$	Number of fuel cells in a single stack
$P$	Pressure
$P_e$	Electric power
$P_{Gross}$	Gross AC power
$P_{HSU}$	Hydrogen separation unit load
$P_{mBOP}$	Mechanical balance-of-plant load
$P_{PSA}$	Pressure swing adsorption unit pressure
$P_s$	Stack pressure
$p$	Partial pressure

$q$	Charge
$\dot{q}$	Rate of charge transfer
$Q$	Heat
$R$	Gas constant
$R_a$	Anode polarization
$R_c$	Cathode polarization
$R_{ir}$	Internal resistance
$S$	Entropy
$T$	Temperature
$T_{PSA}$	Pressure swing adsorption unit temperature
$T_s$	Stack temperature
$U_F$	Fuel utilization factor
$U_{O_2}$	Air utilization factor
$V$	Voltage
$W$	Work
$x$	Molar Fraction

$z$	Number of electrons transferred in the reaction
$\eta$	Efficiency

## ACKNOWLEDGEMENTS

Dr. Brouwer: thank you for teaching me everything I know about fuel cells, compassion for myself and others, the strength in persistent positivity, letting me talk about your hair to the point that it is a known trademark, and never growing a mustache in my presence.

Professor Samuelsen: I have been consistently amazed at your leadership. The organization you built is truly among the best. You provided me an unforgettable journey. I will always be a proud APEPer and will continue to always support the organization. Thank you for keeping the mustache.

Shane, thank you for fatefully running into me. You changed my life when you introduced me to APEP. You have never ceased to be a great friend.

Pere, thank you for your patience, great research, and being a great mentor and friend.

Steve, thank you for being a great friend.

Rich, you are the most amusing and delightful aspect of APEP.

Tim, thank you for being you. There is always another round and a pair of cowboy boots.

To the rest of the APEP family, thank you for being a part of my life.

My mother: Thank you for your selflessness, passion, strength, and resilience. I owe my success solely to your efforts.

To my true friends: Sherman, Merna, Ingrid, Sehra, Christian, Julia, Angie, Robbie, Ryan, and Lisa.



Alicia, Renee, Hong Hoa, Ghazal, and Sayaka: thank you APEP girls for coloring my experience and supporting me.

David, thank you for supporting me through what was the most difficult year of my life. You are irreplaceable.

Mr. CG Bear, thank you for guiding me. You provided invaluable direction.

## ABSTRACT OF THESIS

Development and Verification of a Steady-State Internal Reforming Molten Carbonate Fuel Cell

Model for Tri-generation of Hydrogen, Electricity, and Heat

By

Roxana Bekemohammadi

Master of Science in Civil and Environmental Engineering

University of California, Irvine, 2013

Professor Jacob Brouwer, Chair

A steady-state molten carbonate fuel cell 0-D model was constructed in Aspen Plus<sup>®</sup>. The model simulated the tri-generation of hydrogen, electricity, and heat using a Direct FuelCell<sup>®</sup> molten carbonate fuel cell technology developed by FuelCell Energy. The simulation incorporated operating data from an actual installation. The internal reforming MCFC model was uniquely integrated with hydrogen concentrating and purifying equipment to facilitate tri-generation of hydrogen, electricity, and heat.

A parametric study for the fuel utilization and recovered hydrogen were performed and presented. The tri-generation system performance was characterized for two different fuels, natural gas and anaerobic digester gas, and varying hydrogen recoveries. The optimal range for fuel utilization for each fuel at a particular hydrogen recovery percentage was found. The operating fuel utilization range at a current density of 1200 A/m<sup>2</sup> for a thermally-balanced tri-generation MCFC system operating on NG was found to be: 0.90 for a hydrogen recovery of 90

percent; 0.87—0.90 for a hydrogen recovery of 80 percent; 0.81—0.90 for a hydrogen recovery of 70 percent; and 0.5—0.90 for a hydrogen recovery of 60 percent. The operating fuel utilization range at a current density of  $1200 \text{ A/m}^2$  for a thermally-balanced tri-generation MCFC system operating on ADG was found to be: 0.82—0.90 for a hydrogen recovery of 90 percent; 0.78—0.90 for a hydrogen recovery of 80 percent; 0.69—0.90 for a hydrogen recovery of 70 percent; and 0.5—0.90 for a hydrogen recovery of 60 percent.



## Chapter 1:      **Introduction**

### **1.1 Overview**

Efficiency, reliability, and sustainability are three characteristics that support the vast implementation of fuel cell technology. Fuel cells outperform conventional means of energy production in terms of efficiency. Stationary fuel cells are emerging as a reliable alternative to combustion heat engines for continuous power generation. Most importantly, fuel cells have the potential to be economically, environmentally, and socially sustainable.

Efficiency is an integral aspect of power generation and determines the usefulness of a technology in transforming the energy bound in a fuel to useful products. The comparison of combustion-based and stationary fuel cell power production is necessary to establish the value of fuel cell technology in the future. Heat engines must convert chemical energy into thermal and then mechanical energy to produce electrical energy. Each conversion reduces the efficiency of the heat engine. Electrochemical devices, such as fuel cells, convert chemical energy directly into electrical energy. FuelCell Energy reports that its Direct FuelCell<sup>®</sup> (DFC<sup>®</sup>) product, a high-temperature fuel cell (HTFC), characteristically has 47 % electric power generation efficiency with the potential of reaching 80% depending upon design and operating factors [1]. In contrast, a gas turbine and reciprocating engine of comparable capacity has an electrical power generation efficiency of 25 % and 35 % respectively [1]. The discussion of efficiency is incomplete without the consideration of capacity range. Fuel cells currently outperform gas turbines and combustion-based engines in the power capacity range of 1 kilowatt (kW) to 3 megawatts (MW), which is suitable for on-site power generation. However, large power plants require power outputs far

greater than 3 MW. Fuel cells in the future with power capacities greater than 3 MW are also anticipated to have greater efficiencies than gas turbines and combustion-based engines. Future technological improvements can further increase fuel cell efficiencies and power capacity, which would allow for the implementation of fuel cells in large central power plants.

New reliable energy alternatives are necessary to redefine the energy landscape. Solar, wind turbines, geothermal, and hydropower are four energy alternatives. All four are constrained by inconsistent power availability or geographic limitations. Solar energy is reliant on seasonal and diurnal patterns, as well as location. Wind turbines are restrained by minimum wind velocities, weather unpredictability, and location. Geothermal and hydropower energy are limited mostly by geographical location. In stark contrast, stationary fuel cells can provide electricity and heat virtually anywhere, anytime given the availability of a suitable fuel. Fuel cells are a reliable source of power generation for a baseload power plant, with 95 % power availability [1]. The transmission and distribution of power with traditional grid resources are typically interrupted up to two hours a year [2], whereas a grid-connected stationary fuel cell may have 3.2 to 32 seconds per year of power failure [3]. Consequently, electricity from the grid or alternative energy devices such as solar, wind turbines, geothermal, and hydropower are likely to be less reliable than grid-connected fuel cells. The combination of the grid in parallel with fuel cell generation of electricity at the site of its use can provide reliability in excess of eight “9’s,” which is referred to as “distributed generation (DG).”

DG is economically advantageous for industrial and commercial consumers. Energy, capacity, and ancillary costs associated with buying electricity from the grid can be avoided or decreased with DG systems. The energy cost reflects the electricity consumed. A capacity fee is

charged for power peak demands by the user [2]. Ancillary charges are for “reactive power and voltage control, loss compensation, scheduling and dispatch, load following, system protection, and energy imbalance” [4]. The cost to run a DG system, like a stationary fuel cell, only depends on maintenance and operating costs. Furthermore, the general trend of transmission and distribution costs have been steadily increasing as the cost of DG systems are decreasing [2]. Thus, DG systems are a cost effective option for facilities that demand large amounts of reliable electricity.

Stationary fuel cells have distinct economic benefits as a distributed generator. For example, a California wastewater treatment facility (WWTF) with a stationary fuel cell on-site serves to illustrate the profitability of DG systems. A combined cooling, heating and power (CCHP) system with a 750 kW HTFC produces an average power cost of 11.5 ¢/kWh over five years of initial operation at a wastewater treatment facility [5]. Southern California Edison (SCE) time-of-use energy rates range from 6.5-11.0 ¢/kWh for large business and industrial customers whose monthly maximum demand is over 500 kW, which does not include monthly per meter, facilities-related demand, time-related demand and seasonal time-related charges [6]. A hypothetical large wastewater treatment facility in Southern California that requires 550 kWh for operation 29 days a month at off-peak rates during the winter season pays 39.5 ¢/kWh with four meters. This is a conservative estimate since facilities-related and time-related demand charges are not included; operation only at off-peak rates is unrealistic; an average energy consumption of 550 kWh is reasonable for a large WWTF [7]; and four meters on site is relatively low. The stationary fuel cell produces power that is 28 ¢/kWh less than the price of electricity from the grid. Although SCE’s energy cost is lower than the cost of the stationary fuel cell system, the

additional charges (e.g., capacity, ancillary, etc.) associated with grid use increases the costs significantly. The HTFC cost can decrease further as the cost of fuel cells decrease with increased commercialization and in the example of a wastewater treatment facility, the incorporation of an HTFC for on-site power generation is economically sustainable.

The emission of greenhouse gases (GHGs), such as carbon dioxide ( $\text{CO}_2$ ) and methane ( $\text{CH}_4$ ), and criteria air pollutants, like nitric oxides ( $\text{NO}_x$ ) and sulfur oxides ( $\text{SO}_x$ ), are significant for their role in air quality, climate change, and environmental sustainability. A CCHP system with a stationary fuel cell power generator reduces  $\text{NO}_x$  emissions by 12.1 tons per year and  $\text{CO}_2$  emissions by 7,334 tons per year relative to power from the electrical grid [5]. In comparison, a CCHP that integrates a gas engine emits more  $\text{NO}_x$  with respect to the electrical grid, but it reduces  $\text{CO}_2$  emissions by 6,357 tons per year. An HTFC also emits negligible amounts of  $\text{SO}_x$  and no particulate pollutants [5]. Thus, distributed power generation by an HTFC is advantageous for air quality, climate change, and sustainability.

Environmental and economic sustainability partially capture the dynamics of a strong energy landscape, but socio-political considerations complete the sustainability triad. A technological solution cannot be practical, beneficial, and manageable without the sustainability triad. For instance, the necessity for nations to acquire material resources to produce power has created much political and social instability. Since petroleum has been the main source of fuel since the early 20<sup>th</sup> century, the acquisition of the scarce commodity has spawned numerous global conflicts and in many ways changed history. An example that resonates well with Americans today is the 1973 oil embargo enacted by the Organization of Arab Petroleum Exporting Countries (OAPEC). That event single-handedly influenced political alliances, the Yom Kippur



War outcome, future U.S. energy and monetary policy, and aggravated the 1973-1974 stock market crash [8]. If power production could take place ubiquitously and with the sustainability triad in mind, then the power of oil illustrated during the embargo in 1973 would permanently become a tale of the past. Stationary fuel cells may align well with the notion of the triad and prove to be practical, beneficial, and manageable for all peoples. An HTFC can generate power locally anywhere in the world, thus empowering nations equally and sustaining social and political peace. Fuel cell energy can single-handedly influence the future political and social health of the world.

## 1.2 Motivation

The world's energy needs are forecasted to double by 2050, which poses major challenges specifically to security and climate change. The United States Department of Energy (DOE) recognizes that a "hydrogen economy" could potentially solve both challenges [9]. A hydrogen economy could result in the reduction of greenhouse gases, provide clean, efficient, high-quality energy services, use versatile feedstock (e.g., renewable, fossil fuels, etc.), and remove the country's dependence on petroleum from abroad [2]. However, the current limitations of hydrogen storage, transportation, distribution, and dispensing contribute to the difficulty of developing a hydrogen infrastructure and allowing, as a result, "seamless transitions from production to storage to use" [9]. One reason for this difficulty is the low energy density of hydrogen gas [10]. Hydrogen must be compressed or liquefied for storage, transportation, and distribution, which currently requires substantial electrical power [11]. Typically high capital costs limit compressed high-pressure gas storage to 1,300 kg of hydrogen, which can fuel a fuel cell vehicle for 65,000-78,000 miles [11]. In order for the cost of hydrogen to decrease by a

factor of four to successfully compete with the fossil fuel economy, major technological advances are necessary [9]. Safety is another concern when hydrogen is stored at high pressures. Compressed gas vessels or storage tanks, with pressures as high as 70 megapascals (MPa) are used in vehicles. These high-pressure vessels may cause serious injuries in the event of an accident if not properly designed, installed, and operated. Thus, the advancement of a hydrogen infrastructure depends upon the improvement of cost, safety, and energy efficiency associated with the generation, storage, and transportation of hydrogen.

Hydrogen generation at the point of use enhances the viability of a hydrogen infrastructure and eliminates the costs, safety hazards, and large carbon footprints associated with the storage and transportation of hydrogen. Tri-generation HTFC systems offer this advantage by locally producing hydrogen, waste heat, and electricity at an overall efficiency of 80-85%, with the benefit of ultra-low emissions. All three products are profitable for a facility. Electricity and hydrogen production can vary to satisfy the needs of the plant. Excessive electricity production could be sold to the local grid (depending on the local utility company), promoting additional revenue. The tri-generation of hydrogen from a high-temperature fuel cell has the potential to reliably produce cost-effective hydrogen continuously. The tri-generation HTFC system “has the potential to meet the DOE hydrogen cost targets, while producing power for less than \$0.10/kWh” [12]. Hydrogen produced on-site could also support hydrogen processes for pharmaceutical, electrical, semiconductor industries, as well as power stations, hydrogenation of oils and greases, metal processing, and oil refineries [13]. Waste heat can preheat fuel and air entering the fuel cell or also aid neighboring systems at the plant [14].

The National Fuel Cell Research Center (NFCRC) first established the HTFC tri-generation concept in 2000 and has been engaged in a variety of modeling efforts to characterize the system performance. Previous NFCRC modeling and analyses have found that tri-generation of power, heat, and hydrogen is thermodynamically advantageous in comparison to separate generation of electricity and hydrogen [15]. Further investigation is needed to assess how well high-temperature fuel cells can internally reform alternative fuels, such as anaerobic digester gas (ADG). As of today, fuel cell performance has not been evaluated with ADG, but a synthetic blend.

### 1.3 Goals

The tri-generation of hydrogen, electricity, and heat using an internal reforming molten carbonate fuel cell is a promising technological solution to meeting the demand for distributed power generation and hydrogen as a transportation fuel in a highly efficient and environmental benign manner. There is a need to characterize the performance of a tri-generating molten carbonate fuel cell for various operating conditions to fully comprehend the appropriate implementation of this unique approach to power and hydrogen generation. The intention of this investigation is to perform such a characterization. Hence, the specific goals of the current research are to:

- 1. Develop an accurate and robust simulation of an internal reforming molten carbonate fuel cell system tri-generating hydrogen, electricity, and heat*
- 2. Verify the accuracy of the simulation by comparison to data from the world's first high-temperature tri-generation system*

3. *Evaluate the performance of a tri-generating molten carbonate fuel cell system operating on natural gas and renewable anaerobic digester gas*

## 1.4 Objectives

To achieve these goals, the following four objectives must be fulfilled:

1. *Review the literature associated with high-temperature fuel cell tri-generation and related technologies*
2. *Develop a steady-state model to simulate the tri-generating molten carbonate fuel cell system at OCSD based upon previous simulation strategies*
3. *Verify the steady-state model of a tri-generating molten carbonate fuel cell system*
4. *Evaluate the performance of tri-generating molten carbonate fuel cell system under varying operating conditions*

..

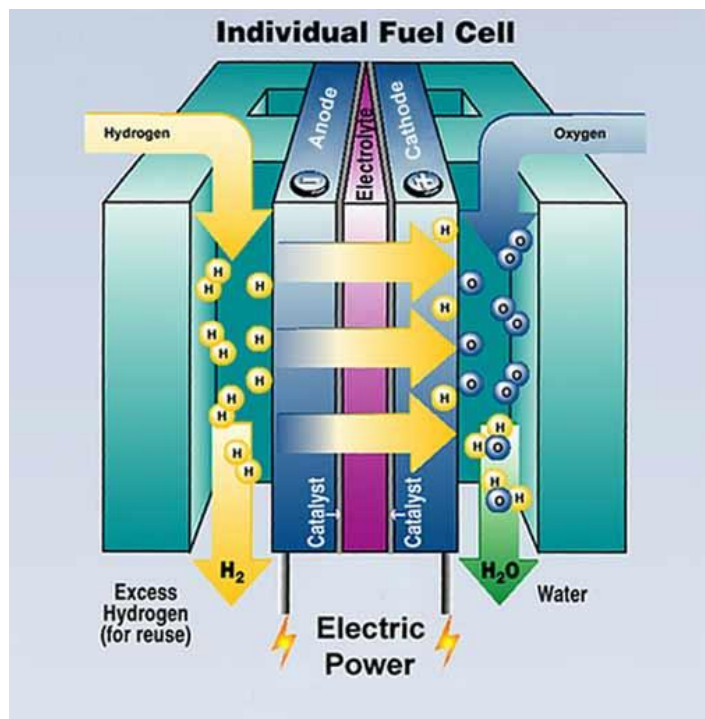
## Chapter 2:      **Background and Literature Review**

### **2.1 Basic Operation of Hydrogen Fuel Cells**

Fuel cells are electrochemical devices that operate similarly to flow batteries. A fuel cell consists of two conductive electrodes separated by an electrolyte. The electrode where oxidation occurs is considered the anode. The cathode is the conductive electrode where the reduction reaction occurs. Ions move through the

electrolyte from one electrode to another depending on the electrochemical reactions unique to a fuel cell type. The half-cell reaction at the anode results in a molecule, typically hydrogen, increasing its oxidation state by losing electrons. The electrons released at the anode are forced to flow through an external circuit to produce electric current, before reaching the cathode to complete the redox reaction. At the cathode, the half-cell reaction results in a molecule,

typically oxygen, reducing its oxidation state by gaining electrons fed through the external circuit. Figure 1[16] illustrates basic hydrogen fuel cell operation. Hydrogen gas enters through a



**Figure 1. Generic fuel cell representation [16]**

channel with direct contact with the anode. Electrons are produced when diatomic hydrogen, the reducing agent, reacts with the ionic charge carrier or decomposes into its elemental form.

## 2.2 Reversible Fuel Cell Voltage

### 2.2.1 Fuel Cell Thermodynamics

Fuel cells are electrochemical devices that convert chemical energy into electrical energy. The study of thermodynamics allows for the quantification and identification of energy flows in a fuel cell system. Thermodynamic potentials, derived from the first and second laws of thermodynamics, describe and quantify flows of chemical, thermal, and electrical energy that enable the characterization of fuel cell performance. The most important thermodynamic potential used in the study of fuel cells is Gibbs free energy ( $G$ ). The change in Gibbs free energy determines the work potential of a fuel cell [17]. The definition of Gibbs free energy is expressed in Equation (2-1):

$$G = U + PV - TS \quad \text{Equation (2-1)}$$

where  $U$  represents the internal energy of a system,  $P$  is pressure,  $V$  stands for volume,  $T$  denotes temperature, and  $S$  represents the entropy of a system. The quantity  $PV$  corresponds to the expansion work done by a system. The amount of heat added to the system is defined by the product of temperature,  $T$ , and entropy,  $S$ . Equation (2-2) expresses the enthalpy ( $H$ ) of a system as the sum of the internal energy and expansion work:

$$H = U + PV \quad \text{Equation (2-2)}$$

Substituting Equation (2-2) into Equation (2-1) yields another definition for Gibbs free energy, as seen in Equation (2-3):

$$G = H - TS \quad \text{Equation (2-3)}$$

Differentiating Equation (2-3) gives Equation (2-4) below:

$$dG = dH - TdS - SdT \quad \text{Equation (2-4)}$$

Assuming variation in the system is isothermal, Equation (2-4) becomes:

$$dG = dH - TdS \quad \text{Equation (2-5)}$$

Equation (2-5) accurately represents the change in energy of a fuel cell system because a fuel cell is ideally operated at constant temperature and pressure. The change in the molar or intrinsic Gibbs free energy ( $\Delta\bar{g}$ ) is presented in Equation (2-6):

$$\Delta\bar{g} = \Delta\bar{h} - T\Delta\bar{s} \quad \text{Equation (2-6)}$$

Enthalpy describes the heat released or absorbed in a reversible process at constant-pressure. The heat released or absorbed during a chemical reaction is called the heat of reaction or enthalpy of reaction ( $\Delta H_{\text{rxn}}$ ). The enthalpy of reaction is the difference between the enthalpy (H) of the products and reactants, as illustrated in Equation (2-7):

$$\Delta H_{\text{rxn}} = \sum v_P H_{\text{Products}} - \sum v_R H_{\text{Reactants}} \quad \text{Equation (2-7)}$$

where  $v_R$  is the reactant stoichiometric coefficient and  $v_P$  is the product stoichiometric coefficient of the corresponding molecule in the reaction. Equation (2-7) on a molar basis becomes:

$$\Delta \bar{h}_{\text{rxn}} = \sum v_P \bar{h}_{\text{Products}} - \sum v_R \bar{h}_{\text{Reactants}} \quad \text{Equation (2-8)}$$

Enthalpy and entropy are not directly measurable quantities in thermodynamics. Therefore, constant-pressure heat capacity ( $C_p$ ), a measurable thermodynamic quantity, is used to describe the enthalpy and entropy of an isothermal, isobaric system. Molar heat capacities ( $\bar{c}_p$ ) for individual molecules are listed in publicly-accessible thermodynamic tables. These empirical values can be curve-fit to express molar heat capacities at constant pressure as a function of temperature  $T$ . Equation (2-9) is a generalized expression for molar heat capacities,

$$\bar{c}_p(T) = a_0 + a_1 T^{b_1} + a_2 T^{b_2} + a_3 T^{b_3} \quad \text{Equation (2-9)}$$

where  $a_0, a_1, a_2, a_3, b_1, b_2, b_3$  are coefficients of a corresponding molecule. Table 1 lists the coefficient values for compounds of interest in this research [17].



**Table 1. Coefficients for molar heat capacity expression in Equation (2-9).**

Species (gaseous)	$a_0$	$a_1$	$a_2$	$a_3$	$b_1$	$b_2$	$b_3$
H <sub>2</sub> O	143.05	-58.0400	8.27510	-0.03698900	0.25	0.50	1.00
H <sub>2</sub>	56.505	-22,222.6	116,500	-560,700.0	-0.75	-1.00	-1.50
O <sub>2</sub>	37.432	2.01020 x 10 <sup>-5</sup>	-178,570	2,368,800	1.50	-1.50	-2.00
CO <sub>2</sub>	-3.7357	3.05290	-0.0410340	2.419800 x 10 <sup>-6</sup>	0.50	1.00	2.00
CO	69.145	-0.0222820	-2,007.70	5,589.640	0.75	-0.50	-0.75

The expression for  $\bar{c}_p$  as a function of temperature is necessary to evaluate the molar enthalpy ( $\bar{h}$ ) of a species at an arbitrary temperature T, as shown in Equation (2-10):

$$\bar{h}(T) = \bar{h}_f(T_0) + \int_{T_0}^T \bar{c}_p(T) dT \quad \text{Equation (2-10)}$$

where  $T_0$  is the reference temperature and  $\bar{h}_f(T_0)$  is the reference enthalpy of formation at  $T_0$ .

The formation enthalpy is defined as the bond enthalpy of a molecule. The integral of the heat capacity represents the sensible enthalpy relative to the reference condition.

The equations for entropy are similarly defined. The entropy of reaction ( $\Delta S_{rxn}$ ) is represented by Equation (2-11):

$$\Delta S_{rxn} = \sum v_P S_{Products} - \sum v_R S_{Reactants} \quad \text{Equation (2-11)}$$

The molar entropy of reaction ( $\Delta \bar{s}_{rxn}$ ) is represented by Equation (2-12):

$$\Delta \bar{s}_{\text{rxn}} = \sum \nu_P \bar{s}_{\text{Products}} - \sum \nu_R \bar{s}_{\text{Reactants}} \quad \text{Equation (2-12)}$$

The molar entropy ( $\bar{s}$ ) of a species at an arbitrary temperature T is shown in Equation (2-13):

$$\bar{s}(T) = \bar{s}(T_0) + \int_{T_0}^T \frac{\bar{c}_p(T)}{T} dT \quad \text{Equation (2-13)}$$

To quantify changes in thermodynamic states, a standard-state condition or reference point needs to be defined. The standard-state condition will refer to a standard reference temperature and pressure of 298.15 K and 1 atm. The values of the molar enthalpy and entropy at the reference temperature ( $T_0$ ) 298.15 K for compounds of interest are listed in Table 2.

**Table 2. Molar enthalpy of formation and entropy values at standard temperature of 298.15 K**

Species (gaseous)	$\bar{h}_f$ (J/mol)	$\bar{s}$ (J/mol·K)
H <sub>2</sub> O	-241,827	188.83
H <sub>2</sub>	—	130.59
O <sub>2</sub>	—	205.14
CO <sub>2</sub>	-393,522	213.80
CO	-110,529	197.65

The molar Gibbs free energy of a reaction ( $\Delta\bar{g}_{rxn}$ ) is found by combining Equation (2-6) Equation (2-8), and Equation (2-12) to form Equation (2-14):

$$\Delta\bar{g}_{rxn} = \Delta\bar{h}_{rxn} - T\Delta\bar{s}_{rxn} \quad \text{Equation (2-14)}$$

Thus,  $\Delta\bar{g}_{rxn}$  values can be calculated from  $\Delta\bar{h}_{rxn}$  and  $\Delta\bar{s}_{rxn}$  values derived from curve-fit heat capacity equations for individual species in Table 1 and standard-state values in Table 2.

### 2.2.2 Standard-State Reversible Fuel Cell Voltage

Fuel cells are constant-temperature, constant-pressure systems that produce only electrical work by moving electrons through an external circuit. The maximum electrical work a fuel cell can perform is the negative value of the change in Gibbs free energy, as presented in Equation (2-15):

$$W_{elec} = -\Delta\bar{g}_{rxn} \quad \text{Equation (2-15)}$$

where  $W_{elec}$  represents electrical work on a molar basis. Equation (2-16) is another definition for  $W_{elec}$  on a molar basis:

$$W_{elec} = q \cdot E_e \quad \text{Equation (2-16)}$$

where  $q$  is the charge moving through an electrical potential difference or an electric field  $E_e$ . Since the charge is attributed to the movement of electrons, charge can be defined as:

$$q = z \cdot F \quad \text{Equation (2-17)}$$

where  $z$  is the number of moles of electrons ( $e^-$ ) moved through the circuit and  $F$  is Faraday's constant (96,485 C /mol  $e^-$ ). The combination of Equation (2-15), Equation (2-16), and Equation (2-17) leads to the relationship between voltage and Gibbs free energy depicted in Equation (2-18):

$$\Delta \bar{g}_{rxn} = -z \cdot F \cdot E_e \quad \text{Equation (2-18)}$$

The reversible open circuit voltage (OCV) for a fuel cell is a simple rearrangement of Equation (2-18):

$$E = -\frac{\Delta \bar{g}_{rxn}}{z \cdot F} \quad \text{Equation (2-19)}$$

The standard-state reversible open circuit voltage for a fuel cell ( $E^\circ$ ) is calculated by evaluating the change in Gibbs free energy at standard-state conditions for the reaction:

$$E^\circ = -\frac{\Delta \bar{g}_{rxn}^\circ}{z \cdot F} \quad \text{Equation (2-20)}$$

Equation (2-20) is valid for an ideal reversible fuel cell operating at constant temperature and pressure at standard-state conditions.

### 2.2.3 Nernst Equation: Reversible Fuel Cell Voltage Variation with Concentration and Pressure

Voltage is dependent on concentration and pressure because of its proportional relationship to the Gibbs free energy, which is also dependent on those parameters. Gibbs free energy relates to concentration and pressure by a thermodynamic quantity called chemical potential ( $\mu$ ). The change in Gibbs free energy due to changes in concentration of chemical species  $i$  is equivalent to the chemical potential of the species  $i$  in a system at constant pressure and temperature:

$$\mu_i^\alpha = \left( \frac{\partial G}{\partial n_i} \right)_{T,P,n_{j \neq i}} \quad \text{Equation (2-21)}$$

where  $\mu_i^\alpha$  is the chemical potential of species  $i$  in phase  $\alpha$  and  $n_i$  is the numbers of molecules of species  $i$ . The chemical potential is associated with concentration by Equation (2-22):

$$\mu_i = \mu_i^0 + RT \ln(a_i) \quad \text{Equation (2-22)}$$

where  $\mu_i^0$  is the reference chemical potential of species  $i$  at standard-state conditions and  $a_i$  is the activity of species  $i$ . For ideal gases, the activity of a species  $i$  is the ratio of the partial pressure of the gas to the standard-state pressure:

$$a_i = \frac{p_i}{p^0} \quad \text{Equation (2-23)}$$

where  $p_i$  is the partial pressure of the gas and  $p^0$  is the standard-state pressure. Rearranging Equation (2-21) and substituting in Equation (2-22) for  $\mu_i^\alpha$  and Equation (2-23) for  $a_i$ , the change in Gibbs free energy ( $\partial G$ ) for a system of  $i$  chemical species becomes:

$$dG = \sum_i \left( \mu_i^0 + RT \ln \left( \frac{p_i}{p^0} \right) \right) dn_i \quad \text{Equation (2-24)}$$

Equation (2-24) can be further simplified by changing Gibbs free energy from an extensive to intensive variable, which results in Equation (2-25):

$$\Delta \bar{g}_{rxn} = \sum v_P \mu_P^0 - \sum v_R \mu_R^0 + RT \ln \frac{\prod \left( \frac{p_P}{p^0} \right)}{\prod \left( \frac{p_R}{p^0} \right)} \quad \text{Equation (2-25)}$$

where  $\mu_P^0$  is the chemical potential of a distinct product at standard-state conditions,  $\mu_R^0$  is the chemical potential of a distinct reactant at standard-state conditions,  $p_P$  is the partial pressure of a distinct product, and  $p_R$  is the partial pressure of a distinct reactant. The sum of the chemical potentials at standard-state conditions for the reaction is equivalent to the standard-state molar Gibbs free energy change for the reaction. Therefore, the Gibbs free energy is related to concentration and pressure through Equation (2-26) :

$$\Delta \bar{g}_{rxn} = \Delta \bar{g}_{rxn}^0 + RT \ln \frac{\prod \left( \frac{p_P}{p^0} \right)}{\prod \left( \frac{p_R}{p^0} \right)} \quad \text{Equation (2-26)}$$

Substituting Equation (2-26) into Equation (2-19) results in the Nernst voltage,  $E$ , is defined below:

$$E = E^0 - \frac{R \cdot T}{z \cdot F} \ln \frac{\prod \left( \frac{p_P}{p^0} \right)}{\prod \left( \frac{p_R}{p^0} \right)} \quad \text{Equation (2-27)}$$

Therefore, the reversible fuel cell voltage varies as a function of pressure and concentration as described by the Nernst equation.

## 2.3 Fuel Cell Types

Various types of fuel cells exist and are distinguished by unique physical and chemical features. Most fuel cell types are named after the electrolyte used. Each fuel cell has distinct half-cell reactions at the cathode and anode. These electrochemical reactions determine the ionic charge carrier, which is the mobile ion traveling through the electrolyte from the cathode to the anode if it has a negative charge and vice versa if the charge is positive. Hydrogen fuel cells can also be distinguished by the materials used throughout the cell. The materials used determine the fuel composition, operational ranges, performance of the fuel cell, as well as many other characteristics. For instance, the mobility of the ionic charge carrier depends on the chemical properties of the electrolyte, which affects the fuel cell voltage and power. Catalysts are another material consideration that limits the fuel composition, operating temperature, and overall fuel cell performance. There are five fuel cell technologies that have been successfully developed and marketed:

1. Proton Exchange Membrane Fuel Cell (PEMFC)
2. Alkaline Fuel Cell (AFC)
3. Phosphoric Acid Fuel Cell (PAFC)
4. Molten Carbonate Fuel Cell (MCFC)
5. Solid Oxide Fuel Cell (SOFC)

General physical and chemical characteristics of these fuel cells are summarized in Table 3 below.

**Table 3. Distinguishing characteristics of five major fuel cell types**

Fuel Cell Type	Electrolyte	Electrodes	Catalyst	Charge Carrier	Temperature
PEMFC	Polymer Exchange Membrane	Carbon	Platinum	H <sup>+</sup>	40-100°C
AFC	Potassium Hydroxide	Transition Metals	Platinum	OH <sup>-</sup>	65-220°C
PAFC	Liquid Phosphoric Acid	Carbon	Platinum	H <sup>+</sup>	205°C
MCFC	Molten Carbonate Salts	Nickel and Nickel Oxide	Electrode Material	CO <sub>3</sub> <sup>2-</sup>	650°C
SOFC	Solid Ceramics	Ceramics (Metal Oxides) and Ceramic-Metal Cermets	Electrode Material	O <sup>2-</sup>	600-1000°C

The physical and chemical characteristics of a fuel cell determine the strengths and weaknesses of that particular fuel cell technology and ultimately dictate its range of applicability. For example, polymer exchange membrane, alkaline, and phosphoric acid fuel cells use platinum to catalyze electrochemical reactions to reach acceptable reaction rates. Since platinum is susceptible to carbon monoxide (CO) and sulfur poisoning, its use restricts fuel cells to only highly-purified or pure hydrogen. The low availability of hydrogen further restricts the applicability of fuel cells that utilize platinum as a catalyst. Therefore, the lack of fuel flexibility is a disadvantage for polymer exchange membrane, alkaline, and phosphoric acid fuel cells. More of the advantages, disadvantages, and applications of the five major fuel cell types are detailed in Table 4



**Table 4. Applications, advantages, and disadvantages of five major fuel cell types**

Fuel Cell Type	Applications	Advantages	Disadvantages
<b>PEMFC</b>	<ul style="list-style-type: none"> <li>• Backup power</li> <li>• Portable power</li> <li>• Distributed generation</li> <li>• Transportation</li> <li>• Specialty vehicles</li> </ul>	<ul style="list-style-type: none"> <li>• Solid electrolyte reduces corrosion and electrolyte management problems</li> <li>• Low temperature</li> <li>• Quick start-up</li> </ul>	<ul style="list-style-type: none"> <li>• Expensive catalysts</li> <li>• Sensitive to fuel impurities</li> <li>• Low-temperature waste heat</li> </ul>
<b>AFC</b>	<ul style="list-style-type: none"> <li>• Military</li> <li>• Space</li> </ul>	<ul style="list-style-type: none"> <li>• Cathode reaction faster in alkaline electrolyte, leads to high performance</li> <li>• Low cost components</li> </ul>	<ul style="list-style-type: none"> <li>• Sensitive to CO<sub>2</sub> in fuel and air</li> <li>• Electrolyte management</li> </ul>
<b>PAFC</b>	<ul style="list-style-type: none"> <li>• Distributed generation</li> </ul>	<ul style="list-style-type: none"> <li>• Higher temperature enables CHP</li> <li>• Increased tolerance to fuel impurities</li> </ul>	<ul style="list-style-type: none"> <li>• Pt catalyst</li> <li>• Long start up time</li> <li>• Low current and power</li> </ul>
<b>MCFC</b>	<ul style="list-style-type: none"> <li>• Electric utility</li> <li>• Distributed generation</li> </ul>	<ul style="list-style-type: none"> <li>• High efficiency</li> <li>• Fuel flexibility</li> <li>• Can use a variety of catalysts</li> <li>• Suitable for CHP</li> </ul>	<ul style="list-style-type: none"> <li>• High temperature corrosion and breakdown of cell components</li> <li>• Long start up time</li> <li>• Low power density</li> </ul>
<b>SOFC</b>	<ul style="list-style-type: none"> <li>• Auxiliary power</li> <li>• Electric utility</li> <li>• Distributed generation</li> </ul>	<ul style="list-style-type: none"> <li>• High efficiency</li> <li>• Fuel flexibility</li> <li>• Can use a variety of catalysts</li> <li>• Solid electrolyte</li> <li>• Suitable for CHP &amp; CHHP</li> <li>• Hybrid/GT cycle</li> </ul>	<ul style="list-style-type: none"> <li>• High temperature corrosion and breakdown of cell components</li> <li>• High temperature operation requires long</li> </ul>

There are many ways to categorize fuel cells based on the differences outlined above, but operating temperature is a commonly used distinguishing factor. Fuel cells can be classified as low-temperature and high-temperature fuel cells. The hydrogen fuel cells discussed are categorized in either of these classes in Table 5:

**Table 5. Operating temperature classification of five major fuel cell types**

	<b>PEMFC</b>	<b>AFC</b>	<b>PAFC</b>	<b>MCFC</b>	<b>SOFC</b>
<b>Temperature</b>	40—100 °C	65—220 °C	190—220 °C	550—650 °C	600—1000 °C
<b>Classification</b>	Low	Low	Low	High	High

These classes have generalized advantages and disadvantages. Several advantages of low-temperature and high-temperature fuel cells are compared below:

- **Low-temperature fuel cells** are better at dynamic load following than high-temperature fuel cells;
- **High-Temperature fuel cells** have lower activation losses due to the temperature dependence of electrochemical reaction rates compared to low-temperature fuel cells;
- **Low-temperature fuel cells** are more durable than high-temperature fuel cells;
- **High-Temperature fuel cells** produce recoverable, high-quality waste heat for combined heat and power (CHP) applications;
- **Low-temperature fuel cells** startup notably faster than high-temperature fuel cells;
- **High-temperature fuel cells** are fuel-flexible unlike low-temperature fuel cells.

The diverse advantages and disadvantages of these particular fuel cells provide opportunities to apply fuel cell technology in various applications. This research focuses on high-temperature fuels for the tri-generation of hydrogen, electricity, and power.

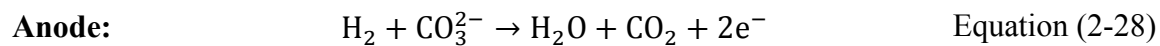
## 2.4 High-Temperature Fuel Cells

Molten carbonate and solid oxide fuel cells operate above 600 °C and are classified as high-temperature fuel cells.

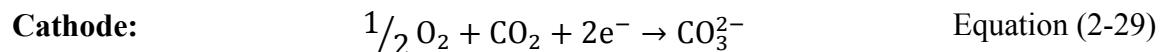
### 2.4.1 Molten Carbonate Fuel Cells

The molten carbonate fuel cell is a high-temperature fuel cell operating typically between 600—700 °C. The electrolyte is mainly composed of a mixture of alkali metal carbonates such as lithium carbonate ( $\text{Li}_2\text{CO}_3$ ) and potassium carbonate ( $\text{K}_2\text{CO}_3$ ), which are solid salts at room temperature. The high operating temperature allows for the liquefaction of the salts, resulting in a highly conductive molten mixture with mobile carbonate ions ( $\text{CO}_3^{2-}$ ) providing ionic conduction. A ceramic matrix of lithium aluminate ( $\text{LiAlO}_2$ ), also called lithium aluminium oxide, supports the molten salt slurry. The anode is typically constructed of nickel chromium/nickel aluminum (Ni-Cr/Ni-Al) alloy while the cathode consists of lithiated nickel oxide (NiO). Molten carbonate fuel cells operate at high enough temperatures that inexpensive nickel-based electrodes sufficiently catalyze the electrochemical fuel cell reactions without the use of expensive precious metals like platinum typically seen in low-temperature fuel cells.

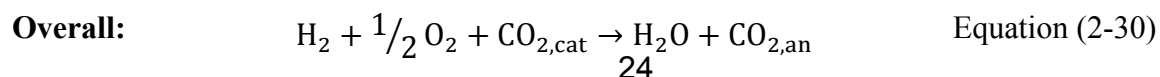
The electrochemical reactions in the molten carbonate fuel cell take place at the anode and cathode. The oxidation reaction at the anode and reduction reaction in the cathode are shown below:



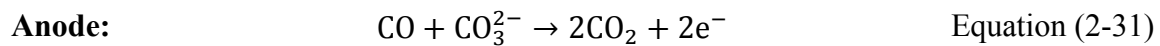
**Figure 2. Molten carbonate fuel cell.**



The overall net reaction for the electrochemical half reactions is:



The basic operation of a molten carbonate fuel cell is pictured in Figure 2. The mobile charge carrier ( $\text{CO}_3^{2-}$ ) is produced at the cathode and consumed at the cathode. In contrast to low-temperature fuel cells that have low tolerance for carbon oxides, molten carbonate fuel cells uniquely consume carbon oxides electrochemically. For instance,  $\text{CO}_2$  is a reactant in the cathode compartment and  $\text{CO}$  can electrochemically react with  $\text{CO}_3^{2-}$  to form  $\text{CO}_2$  in the anode compartment.



The rate at which this reaction proceeds is unknown, but is expected to be much slower than the rate of hydrogen electrochemical oxidation. Herein it was assumed that, the nickel-based anode catalyst promotes the oxidation of  $\text{CO}$  via the water-gas shift reaction (refer to 2.5.4 Water-Gas Shift), where the hydrogen produced subsequently reacts with the carbonate ion.

In order to provide  $\text{CO}_2$  to the cathode, the  $\text{CO}_2$  produced at the anode is externally recycled to the cathode or another external stream rich with  $\text{CO}_2$  is fed to the cathode. If the anode exhaust is recycled, the  $\text{H}_2$  and  $\text{CO}$  are oxidized in a burner and mixed with fresh air before it is returned to the cathode. The heat released during the oxidation process can be used to preheat the fuel or air.

## 2.5 Hydrogen Production Methods

Hydrogen is the most abundant element in the universe, accounting for 90 % of the atoms in the universe. It also makes up 15 % of the Earth's crust, the third most abundant element on Earth. Nearly all hydrogen atoms on Earth are bound to other elements, forming hydrocarbons and water [18]. It rarely exists in its diatomic molecular form on Earth. Thus, hydrogen is extracted from a variety of sources like coal, natural gas, biomass, solar, wind, and nuclear energy through various production methods. Only three hydrogen production methods will be discussed: steam-methane reforming with water-gas shifting, electrolysis, and biological hydrogen production.

### 2.5.1 Steam-Methane Reforming

Today, the United States produces 9 million tons of hydrogen gas [19], which about 95 percent of it is derived from natural gas via a steam-reforming process [20]. Steam methane reforming is typically coupled with another chemical process, water-gas shift, which increases the hydrogen yield or concentration in the stream exiting the reformer. Water-gas shift chemistry is described in section 2.5.4 Water-Gas Shift.

### 2.5.2 Steam-Methane Reforming Chemistry

Steam-methane reforming is the process of reacting methane with steam over a catalyst at high temperature to produce hydrogen and carbon monoxide. The steam-methane reformation reaction is shown below:



The reaction is driven forward to produce hydrogen and carbon monoxide at high temperatures (550—900 °C) due to its endothermicity [21]. The reforming reaction results in a volume expansion, which means that methane conversion is greater at lower pressures according to Le Chatelier's principle [21]. However, reformers typically operate between 30—40 bar for more compact reactor design, although operation at those high pressures negatively affect the molar percentage of hydrogen in the resulting stream, as referred to as hydrogen yield [22]. The reversible reaction normally reaches equilibrium over an active catalyst like nickel [21]. The water-gas shift reaction nearly always occurs over steam-methane reforming catalyst. The relationship between reforming and water-gas shift chemistry will be discussed in 2.5.4 Water-Gas Shift.

### 2.5.3 Centralized Steam Methane Reforming

In the United States, most of the hydrogen produced today is manufactured via steam reforming of natural gas. In industrial applications, steam reformers produce 25 to 100 million standard cubic feet of hydrogen per day [23]. To distribute hydrogen from large central plants, the gas must either be compressed or liquefied. Although a central SMR plant can be almost as efficient as gasoline production, the high costs and low energy efficiency of compressing, transporting, and dispensing hydrogen present significant challenges [24]. These issues stem from the physical and thermodynamic properties of molecular hydrogen. Due to its low volumetric energy density, molecular hydrogen gas must be compressed or liquefied in order to be transported in practical quantities. The electric energy needed to compress hydrogen to 5000

psi is 4 to 8 percent of its energy content (depending on the starting pressure) and 30 to 40 percent of its energy content to liquefy and store hydrogen [24]. Distributed steam methane reforming is considered a favorable alternative to central SMR, as it avoids a portion of the energy penalties associated with compressing, transporting, and dispensing hydrogen.

#### 2.5.4 Water-Gas Shift

The water-gas shift (WGS) reaction is used to increase the hydrogen yield in a synthesis gas typically after steam methane reforming. Specifically, water-gas shift refers to the reaction of carbon monoxide with steam to yield carbon dioxide and hydrogen:



This reaction is favored at temperatures of less than about 600 °C, and can take place as low as 200 °C, with sufficiently active catalysts [25]. Although the direction of the reaction depends on temperature, it is unaffected by changes in pressure unlike the steam methane reformation reaction [22]. It is mildly exothermic reaction, with an adiabatic temperature rise of 8 to 10 °C per percent of CO converted to CO<sub>2</sub> [25]. The gas exiting the shift reactor contains mostly H<sub>2</sub> (70—80 %) plus CO<sub>2</sub>, CH<sub>4</sub>, H<sub>2</sub>O, and small quantities of CO [25]. The shift reaction is often accomplished in two stages. A high-temperature shift (HTS) reactor operating at about 350—475 °C with the inlet temperature ranging 320 to 360°C, accomplishes most of the conversion [25]. It is then followed by a low-temperature shift (LTS) reactor operating at about 200—250 °C which brings the CO concentration down to a few percent by volume or less [25]. The inlet gas temperature should be at least 20 °C above its dew point to avoid deactivation of the catalyst by

water condensation [25]. At least one heat exchanger is necessary to cool the exhaust from the HTS before entering the LTS reactor.

## 2.6 Hydrogen Separation Technologies

### 2.6.1 Pressure Swing Adsorption

Pressure swing adsorption (PSA) is a chemical process that uses variation in pressure to separate certain species. Gases under high pressure tend to be attracted to solid surfaces and “adsorb” onto them. Every gas molecule has a different affinity for solid surfaces. The higher the pressure, the more gas is adsorbed on reactor beds; when the pressure is reduced, the gas is released, or desorbed. When the bed reaches the end of its capacity to adsorb a particular gas, it can be regenerated by reducing the pressure, releasing the adsorbed gas [26].

A typical PSA system involves a cyclic process where a number of connected cylindrical beds containing adsorbent materials are successively pressurized and depressurized in order to produce a continuous stream of purified product gas at high pressures and the waste stream or “tail gas” at low pressures [26]. For hydrogen production, hydrogen-rich gases are pumped into a cylinder at high-pressure. The cylinder contains a bed of adsorbent material. The impurities in the inlet gas, such as carbon dioxide, are adsorbed onto the surfaces of the adsorbent bed, leaving purified hydrogen in the cylinder. The purified product stream exits the PSA at a slightly lower pressure than the feed [26]. Pressure in the cylinder is then reduced, releasing the impurities from the adsorbent material. A small amount of purified hydrogen is used to flush the waste gas out of the system to regenerate the adsorbent material for another purification cycle; the exiting mixture or tail gas leaves the PSA at a significantly lower pressure [26].



## 2.7 Tri-Generation of Hydrogen, Electricity, and Heat Using a Fuel Cell

Fuel cell, hydrogen production, and hydrogen separation technologies were discussed throughout Chapter 2. In contrast to the traditional methods of producing hydrogen discussed in 2.5 Hydrogen Production Methods, tri-generation using a fuel cell is a unique way to produce hydrogen. Tri-generation describes a system that produces three valuable outputs from one or more natural resources. A fuel cell is an electrochemical device that generates two valuable products: electric power and thermal energy. Based on practical limitations of fuel cell stacks, not all of the hydrogen gas supplied is consumed electrochemically in the fuel cell. In fact, no more than 90 percent of the hydrogen available in the cell is consumed to avoid practical issues that adversely affect the performance of a fuel cell system, such as very low hydrogen partial pressures, cell starvation, and slight mal-distribution of multi-component fuels like partially reformed fuel throughout the stack [27]. Therefore, there is a portion of hydrogen exiting the fuel cell. The unreacted hydrogen can be as valuable as heat or electricity. The excess hydrogen could be used as fuel for another energy conversion device like a combustion engine [28] or fuel cell [29], recycled to the fuel cell to more efficiently generate electric power and heat [27, 30], burnt to provide heat energy for the system [27, 28, 29, 30], or separated and stored for an application outside the system [28, 31].

Fuel cells can be integrated with various technologies to comprise of a single tri-generating system. The configuration of the tri-generation system components depends on the desired output of each product and the thermodynamic limitations of the whole system. Any of the fuel cell types discussed in 2.3 Fuel Cell Types has the ability to tri-generate because the practical limitations of using 100 percent of the fuel is ubiquitous. However, this study focuses

on tri-generation systems using high-temperature fuel cells. The next section will discuss previous research conducted on the tri-generation of hydrogen, electricity, and heat using a high-temperature fuel cell.

### 2.7.1 Previous Research

Leal et al. performed energy and exergy analyses for various configurations of a high-temperature fuel cell co-producing hydrogen discussed in “Production of hydrogen using high-temperature fuel cell: energy and exergy analysis” [10]. The intention of the study was to assess the thermodynamic performance of tri-generating HTFC system designs. The impact of various reformer placements in an HTFC configuration was compared to internal reforming HTFCs in terms of hydrogen and electricity production. The study found that co-production of power and hydrogen using an internal reforming high-temperature fuel—may it be molten carbonate or solid oxide—was thermodynamically advantageous compared to separate generation of electricity by a fuel cell and hydrogen by a methane steam reformer. Margalef et al. expanded upon Leal et al.’s work in “Conceptual design and configuration performance analyses of polygenerating high temperature fuel cells” by introducing hydrogen separation using a pressure swing adsorption unit into the HTFC configurations [32]. Again, the internal reforming cases proved to be most efficient. Thus, Leal et al. [10] and Margalef et al. [32] substantiated the use of an internal reforming HTFC with or without a PSA as a more efficient design strategy for the co-production of hydrogen.

Polytechnic University of Turin Researchers Flavio Nicolin and Vittorio Verda have published several papers modeling a tri-generating molten carbonate fuel cell system operating on biogas (not exclusive to ADG) [33, 34, 35]. Their system is designed with a molten carbonate

fuel cell that produces electricity for export and/or system, hydrogen for export and/or heat generation for the external reformer, high-quality waste heat and oxidant for a micro-turbine generating more electricity. The system design is similar to Margalef et al [32], but utilizes an additional energy conversion device, in this case a micro-turbine, to increase the overall efficiency of the system.

Tri-generation of hydrogen, electricity, and heat using an internal reforming molten carbonate fuel cell integrated with a hydrogen purification unit has not been modeled and evaluated to date, which provides a unique opportunity to contribute to this research field. Furthermore, the characterization of FuelCell Energy's Direct FuelCell<sup>®</sup> internal reforming MCFC system tri-generating hydrogen, electricity, and heat has not been published to date. A verified model of a tri-generation DFC<sup>®</sup> is valuable to the research community, as well as for real-world applications. The Direct FuelCell<sup>®</sup> is the most widely used commercial molten carbonate fuel cell system in the world currently and the demand for tri-generation Direct FuelCell<sup>®</sup> will increase in the future. Therefore, research in this area is necessary.

### 2.7.2 Hydrogen Energy Station

The configuration of a tri-generation system depends on the use of the hydrogen product, as discussed in 2.7.1 Previous Research. Today, hydrogen is mostly produced via centralized steam methane reformation. Although SMR technology is mature, it is not efficient on a small-scale and includes a sizable energy penalty to transport liquefied or compressed hydrogen to the point of use [36]. Small-scale, high-efficiency, low emissions hydrogen generation method capable of operating on a variety of feedstock would be beneficial to developing a hydrogen

fueling infrastructure for hydrogen-powered vehicles. Hydrogen energy stations could address that need.

The hydrogen energy station concept is based on the tri-generation of hydrogen, electricity, and heat using a high-temperature fuel cell coupled with a hydrogen fueling station. The innovative design allows for small-scale, distributed generation of hydrogen, eliminating the sizable energy penalty for transport. The system could produce negligible  $\text{NO}_x$  and  $\text{SO}_x$  emissions. It may produce less  $\text{CO}_2$  than centralized steam-methane reformation if a molten carbonate fuel cell is used as the high-temperature fuel cell, since  $\text{CO}_2$  is electrochemically consumed in the molten carbonate fuel cell [37].

### **2.7.3 Hydrogen Energy Station Demonstration at Orange County Sanitation District**

The hydrogen energy station concept was conceived at the National Fuel Cell Research Center in 2000. The California Air Resources Board, South Coast Air Quality Management District and Department of Energy are supporting the collaborative effort of the NFCRC, Air Products and Chemicals, Inc. and FuelCell Energy, to demonstrate this technology at the Orange County Sanitation District, a wastewater treatment facility located near the NFCRC. The tri-generation fuel cell system is undergoing beta-testing while operating on renewable anaerobic digester gas. The electricity and heat produced by the system supports operations at OCSD, and the hydrogen is piped 2000 feet to a hydrogen fueling station also located at Orange County Sanitation District to help support about 70 fuel cell vehicles in southern Orange County. This

demonstration marks the world's first renewable hydrogen energy station, which the DOE has identified as the "fuel station of the future" [38].

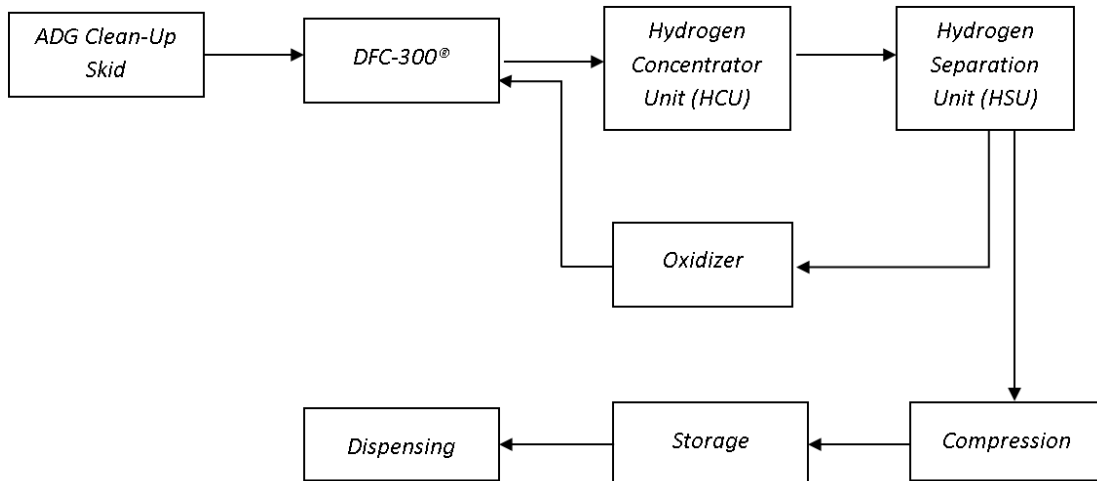
The tri-generation system employs novel integration and control strategies of pre-commercial and commercial equipment. The pre-commercial equipment includes an ADG clean-up module and an Air Products and Chemicals, Inc. hydrogen purification unit using pressure-swing adsorption. The 300 kW FCE internal reforming molten carbonate fuel cell, water-gas shift reactors, electric chillers, and compressors are commercial products uniquely controlled and integrated for tri-generation operation.

The Hydrogen Energy Station employs novel integration and control strategies to operate commercial technologies in "tri-generation mode." The main commercial units uniquely controlled and integrated for tri-generation operation include:

- anaerobic digester gas clean-up module;
- APCI hydrogen purification unit using pressure-swing adsorption;
- APCI hydrogen refueling station;
- FCE 300kW internal reforming molten carbonate fuel cell;
- water-gas shift reactors;
- electric chillers; and
- compressors.

The system at OCSD is illustrated in Figure 3. It includes a FuelCell Energy 300 kw Direct FuelCell® (DFC300®) power plant that is capable of tri-generating hydrogen, waste heat, and electricity. The anaerobic digester gas generated at OCSD will be processed through a

“clean-up skid” that will remove sulfur compounds and siloxanes, which poison molten carbonate fuel cells. The electricity produced by the fuel cell will power the system and additional equipment at OCSD. The hydrogen produced by the DFC300<sup>®</sup> will be concentrated, purified, compressed, and then stored for hydrogen refueling located at the entrance of OCSD. The waste heat generated during the process will not be utilized at the project site.



**Figure 3. Process flow diagram of the installed tri-generation system.**

The FuelCell Energy 300 kW Direct FuelCell<sup>®</sup> was initially fueled with natural gas; in July 2011, this was transitioned to anaerobic digester gas. ADG, a renewable biogas produced by anaerobic digesters common at wastewater facilities, is methane-rich and typically used for co-generation of electricity and heat. The Hydrogen Energy Station not only co-generates electricity and heat from ADG, but produces *renewable hydrogen* with negligible NO<sub>x</sub> and SO<sub>x</sub> emissions. Thus, the electricity and heat produced by the system supports operations at OCSD, and the

hydrogen is piped 2000 feet to a hydrogen fueling station located at the entrance of OCSD, supporting approximately 70 fuel cell vehicles in the area.

## 2.8 Summary

In summary, tri-generation of hydrogen, electricity, and heat using an internal reforming molten carbonate fuel cell integrated with a hydrogen purification unit has not been modeled and evaluated to date, which provides a unique opportunity to contribute to this research field. Furthermore, the characterization of FuelCell Energy's Direct FuelCell<sup>®</sup> internal reforming MCFC system tri-generating hydrogen, electricity, and heat has not been published to-date.

The demonstration of this technology at Orange County Sanitation District provides an invaluable opportunity for the generation and provision of data from the actual tri-generation fuel cell system. These data are essential for the development, verification, and evaluation of a Direct FuelCell<sup>®</sup> internal reforming molten carbonate fuel cell system tri-generating hydrogen, electricity, and heat. The Direct FuelCell<sup>®</sup> is the most widely used commercial molten carbonate fuel cell system in the world currently and the demand for tri-generation Direct FuelCell<sup>®</sup> will increase in the future. As a result, a verified model of a tri-generation DFC<sup>®</sup> is valuable to the research community, as well as for real-world applications. Additional depth is achieved by the ability to assess two different fuels: natural gas and anaerobic digester gas; both of which are regaining interest due to an increasing focus on emissions-saving strategies and cleaner fuels. Therefore, research in this area is necessary.





## Chapter 3:      **Approach**

The following tasks were developed to address the objectives listed in 1.4 Objectives in order to complete the research goals outlined in 1.3. Goals:

1. *Review the literature associated with high-temperature fuel cell tri-generation and related technologies*

The literature related to molten carbonate fuel cell modeling; tri-generation of hydrogen, electricity, and heat using a fuel cell; empirical data available for FuelCell Energy's Direct FuelCell<sup>®</sup> technology; Direct FuelCell<sup>®</sup> modeling; molten carbonate fuel cell polarization losses; molten carbonate fuel cell electrolyte compositions; fuel cell modeling in Aspen Plus<sup>®</sup>; internal indirect and direct reformation; water-gas shift chemistry and reactors; and pressure swing adsorption were all necessary and reviewed for the thorough assessment of previous research methodologies and outcomes.

2. *Develop a steady-state model to simulate the tri-generating molten carbonate fuel cell system at OCSD based upon previous simulation strategies*

A steady-state solid oxide fuel cell 0-D model constructed in Aspen Plus<sup>®</sup> was converted to an internal reforming molten carbonate fuel cell model by first changing the electrochemistry and system integration. The model was further adapted to simulate the tri-generation system by incorporating operating characteristics of the equipment installed at OCSD. The internal reforming molten carbonate fuel cell model was uniquely integrated with hydrogen concentrating and purifying equipment to facilitate tri-generation of hydrogen, electricity, and heat. Modeling the Direct FuelCell<sup>®</sup> technology

developed by FuelCell Energy comprised the bulk of the equipment specification effort. This process is detailed in 4.3 Process Models. The tri-generation system model was based off the design of and equipment employed at the OCSD energy station installation. The ADG clean-up skid and the process of preparing purified hydrogen for fueling (compression, storage, and dispensing) were determined to be outside of the scope of the study and excluded from the model. The intention of the model was to evaluate the tri-generation concept without bounding the results to a specific end-of-use for the purified hydrogen, such as refueling, nor a specific fuel process

3. *Verify the steady-state model of a tri-generating molten carbonate fuel cell system*

In order for the tri-generation model to be verified, simulated tri-generation operation on natural and anaerobic digester gas must match real system data. The molten carbonate fuel cell system, the largest and most significant unit in the model, must be proven accurate at typical operating conditions where hydrogen is not separated and exported, which has been termed as “normal operation.” This is the first step to verifying the model because previously published research on a tri-generation system using a DFC<sup>®</sup> molten carbonate fuel cell system does not exist for comparison. Thus, it was assumed that verifying the performance of the modeled DFC<sup>®</sup> in “normal operation” would also confirm that the modeled fuel cell contained sufficient physical, chemical, and electrochemical details to allow simulation in “tri-generation mode.” Consequently, results pertaining to the fuel cell performance in “tri-generation mode” would warrant discussions unburdened by the question of accurate fuel cell model development. Once the modeled DFC<sup>®</sup> system in “normal operation” is verified, collected data from the

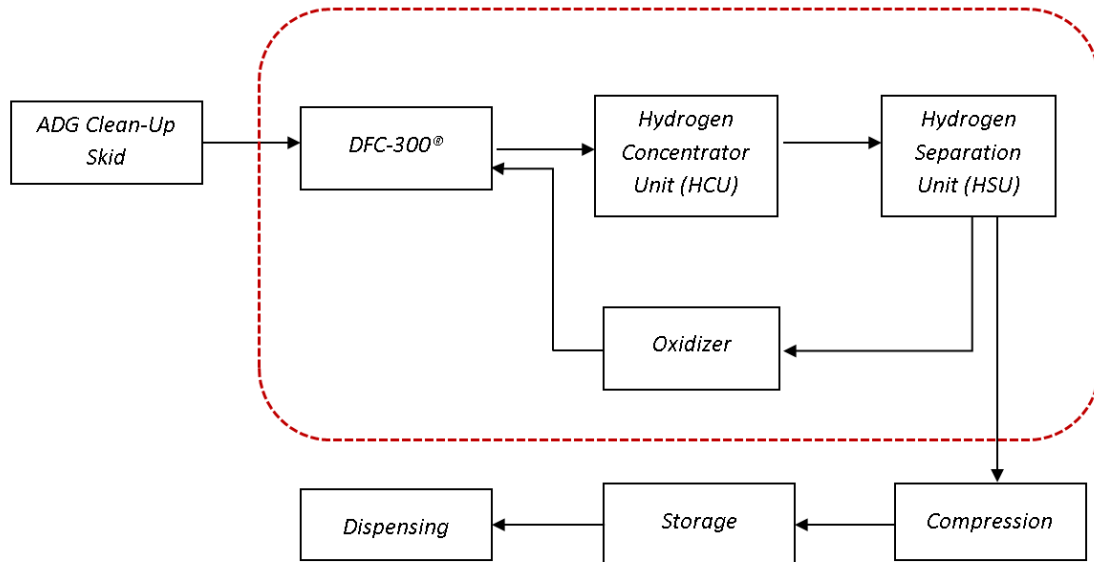
hydrogen energy station at OCSD would be used to verify the tri-generation model operating on two different fuels: natural gas and anaerobic digester gas.

4. *Evaluate the performance of tri-generating molten carbonate fuel cell system under varying operating conditions*

The set points for fuel utilization and recovered hydrogen were varied for the MCFC tri-generation model for both natural gas and anaerobic digester gas. The rest of the operating conditions for the system were static. The output variables, such as voltage, power, recoverable heat, oxygen utilization, increased cooling air demand, were analyzed for varying fuel utilizations and recovered hydrogen.

## **Chapter 4:      Model Development**

A steady-state, non-dimensional model of the tri-generation system was built using the process flow simulation software, Aspen Plus<sup>®</sup> Version 7.2. The model consists of a molten carbonate fuel cell uniquely integrated with hydrogen concentrating and purifying equipment to facilitate tri-generation of hydrogen, electricity, and heat. The tri-generation system model was based off the design of and equipment employed at the OCS D energy station installation. However, the ADG clean-up skid and the process of preparing purified hydrogen for fueling (compression, storage, and dispensing) were determined to be outside of the scope of the study. The intention of the model was to evaluate the tri-generation concept without bounding the results to a specific end-of-use for the purified hydrogen, such as refueling, nor a specific fuel processing technology like biogas purification. Thus, the FuelCell Energy DFC300<sup>®</sup> fuel cell system, hydrogen concentrator unit, and hydrogen separation unit were accounted for in the model, as illustrated in Figure 4.



**Figure 4. Scope of tri-generation model**




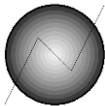

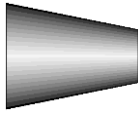


Piping, redundant equipment, electrical components, valves, blowers, and pumps were also excluded from the model.

Limited equipment specifications for several major components of the OCSD tri-generation system were incorporated into the model. The specifications were either provided by project partners or acquired through journal publications, United States patents, and conference papers and presentations. The intention of the study was to capture the overall performance of the installed tri-generation system accurately at certain operating conditions using known equipment specifications and system design; it is, however, not bound solely by the tri-generation design and equipment specifications incorporated at Orange County Sanitation District.

## 4.1 Process Simulation

Chemical process models can be constructed and optimized in Aspen Plus<sup>®</sup> using built-in functions. However, Aspen Plus<sup>®</sup> does not provide a built-in fuel cell model. Researchers have successfully modeled fuel cell systems by extending the functionality of the software by uniquely integrating chemical process models, user-defined calculator blocks, and design specifications to mimic physical processes. The tri-generation system was similarly constructed in Aspen Plus<sup>®</sup>. Table 6 below lists the Aspen Plus<sup>®</sup> chemical process models used in the simulations.

Table 6 Aspen Plus® unit operation models

Unit Operation Model Name & Type	Symbol	Description	Requirements
REquil <i>Equilibrium reactor</i>		Calculates chemical equilibrium	<ul style="list-style-type: none"> <li>• Reaction stoichiometry is known</li> <li>• Some or all reactions reach chemical equilibrium</li> </ul>
RGibbs <i>Equilibrium reactor</i>		Calculates equilibrium using Gibbs free energy minimization	<ul style="list-style-type: none"> <li>• Known reaction stoichiometry is NOT needed</li> <li>• Some or all reactions reach chemical equilibrium</li> </ul>
HeatX <i>Two-stream heat exchanger</i>		Exchanges heat between two streams	<ul style="list-style-type: none"> <li>• Outlet temperature of the hot or cold stream, or</li> <li>• Vapor fraction of the hot or cold stream, or</li> <li>• Temperature change of the hot or cold stream</li> </ul>
Heater <i>Heater or cooler</i>		Determines thermal and phase conditions of outlet stream	<ul style="list-style-type: none"> <li>• Heat duty, or</li> <li>• Outlet temperature, or</li> <li>• Outlet pressure</li> </ul>
Flash2 <i>Knock out drum</i>		Produces one vapor outlet stream, one liquid outlet stream	<ul style="list-style-type: none"> <li>• Heat duty, or</li> <li>• Outlet temperature, or</li> <li>• Outlet pressure</li> </ul>
Compr <i>Compressor</i>		Changes stream pressure when power requirement is needed or known	<ul style="list-style-type: none"> <li>• Type of compression if compressor performance is unknown</li> <li>• Discharge conditions (e.g., pressure ratio, discharge pressure, pressure increase, power demand)</li> <li>• Efficiency (default—0.72)</li> </ul>
Valve <i>Expansion valve</i>		Determines the thermal and phase condition of the stream at the valve outlet	<ul style="list-style-type: none"> <li>• Valid stream phases</li> <li>• Outlet pressure, or</li> <li>• Pressure drop</li> </ul>
Sep2 <i>Separator</i>		Separates inlet stream components into two outlet streams, based on specified flows, split fractions, or purities	<ul style="list-style-type: none"> <li>• Fraction of a component in the feed going to either outlet stream</li> <li>• Mass/mole flow rate of a component in the outlet stream</li> <li>• Mass/mole fraction of component in an outlet stream</li> <li>• Pressure drop</li> <li>• Outlet temperature</li> </ul>

Aspen Plus® calculator blocks provide the flexibility necessary to build a custom simulation by performing user-defined calculations written in an embedded Microsoft Excel® spreadsheet or Fortran subroutine. The calculator block function was used extensively to model the fuel cell. The consumption and generation of the charge carrier at the anode and cathode respectively could not be simulated using an existing Aspen Plus® process model. Instead, calculator blocks performed mass balance, voltage, and power calculations in order to compensate for the fuel cell electrochemical reactions that could not be modeled using existing process models.

The Aspen Plus® model could not converge if too many physical parameters were interdependent. Thus, design specifications were also used to implement causal relationships whilst avoiding model divergence. For instance, a design specification was used to affix heat duties to a heater or cooler process model when a heat exchanger process unit could not be used to model the exchange of heat between some streams without causing the model to diverge.

The simulation was designed to depend on the following input variables:

- fuel utilization factor
- current density
- steam-to-carbon ratio (S / C) or water flow rate
- PSA recovery
- temperature and pressure operating conditions for all equipment
- fuel composition and flow rate
- air composition and flow rate



The model predicted the following variables:

- Nernst voltage
- Fuel cell operating voltage
- fuel cell polarization losses
- gross DC power
- net power
- exported hydrogen flow rate
- stream compositions
- fuel cell system parasitic loads
  - mechanical balance-of-plant
  - DC-AC conversion
- hydrogen separation unit load
- high-quality recoverable waste heat
- hydrogen, electrical, and overall efficiency

The main assumptions for the entire system were:

- adiabatic conditions
- ideal gas properties true
- Negligible pressure drop in heat exchangers

## 4.2 Process Description

Researching patent applications was one method of adapting the actual design of the installed tri-generation system into the model. Several issued patents and patent application publications with the assignee, FuelCell Energy, Inc., describing various tri-generation designs that would improve fuel cell operation and efficiency were discussed in 2.7 Tri-Generation of Hydrogen, Electricity, and Heat Using a Fuel Cell. One patent application discussed, “Fuel cell power production system with an integrated hydrogen utilization device” [28], contained an invention very similar to the tri-generation concept, but also included a “hydrogen utilization device.” The hydrogen utilization device could be an internal combustion engine, combustion turbine, recuperative turbine, or a microturbine. The fuel cell system tri-generates hydrogen, electricity, and heat and exports hydrogen in the same manner as the tri-generation system analyzed in this study. The purified hydrogen is exported, as is the case in this study, but a portion of the hydrogen is also used to fuel an additional power generation device to produce additional power. Both designs still included the hydrogen concentrator and hydrogen separation units that are fundamental to facilitating tri-generation for a high-temperature fuel cell system. In other words, removing the hydrogen utilization device from the patent design produced essentially the same integration strategy necessary for constructing a hydrogen energy station. Thus, the design presented in “Fuel cell power production system with an integrated hydrogen utilization device” patent application for FuelCell Energy, Inc. served as the basis of the tri-generation system modeled in Aspen Plus<sup>®</sup>. A drawing of the tri-generation system claimed in the referenced patent application is shown in Figure 5 [28] below.

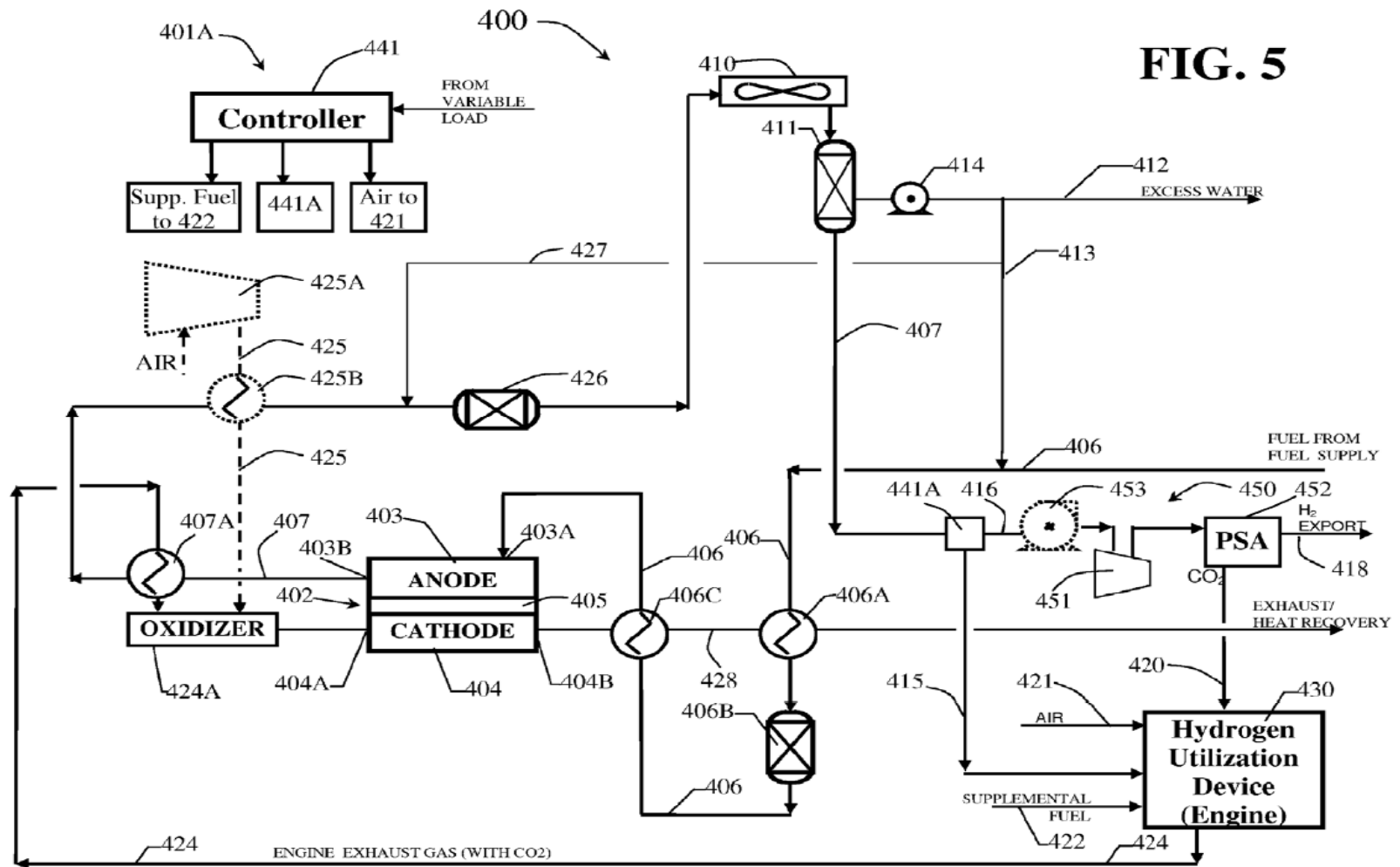


Figure 5. U.S. patent application drawing of tri-generating HTFC system coupled with a hydrogen utilization device [28]

There are four variations on the general drawing in the patent application with the last drawing, “FIG 5,” representing the high-temperature fuel cell system modified for increased hydrogen production to fuel the hydrogen utilization device and/or for export (pictured as Figure 5 above). The modification for increased hydrogen production is marked by the “additional components for extracting and exporting hydrogen fuel from the anode exhaust gas” [28], otherwise defined as the hydrogen concentrator and separation units in this study.

Main components of the tri-generating fuel cell system without a hydrogen utilization device include:

- anode (403)
- cathode (404)
- pre-reformer (406B)
- syngas compressor (451)
- water-gas shift reactors (426)
- air compressor (425A)
- heat exchanger (410, 407A, 406A, 406C, 425B)
- water knock-out drum (411)
- oxidizer (424A)
- water pump (414)
- splitter (441A)
- blower (453)
- PSA (452)

where the unique numeric identifier in parentheses is associated to each component in Figure 5. The blower and water pump are not modeled, but assumed in the fuel cell mechanical balance-of-plant load. The splitter was not modeled because the actual system is assumed to always separate hydrogen from the anode exhaust; the purified hydrogen stream could be recycled to the anode if not exported in order to increase the cell voltage [27, 30]. The rest of the components were taken account in the model. The process flow diagram of the modeled tri-generation system is displayed in Figure 6.

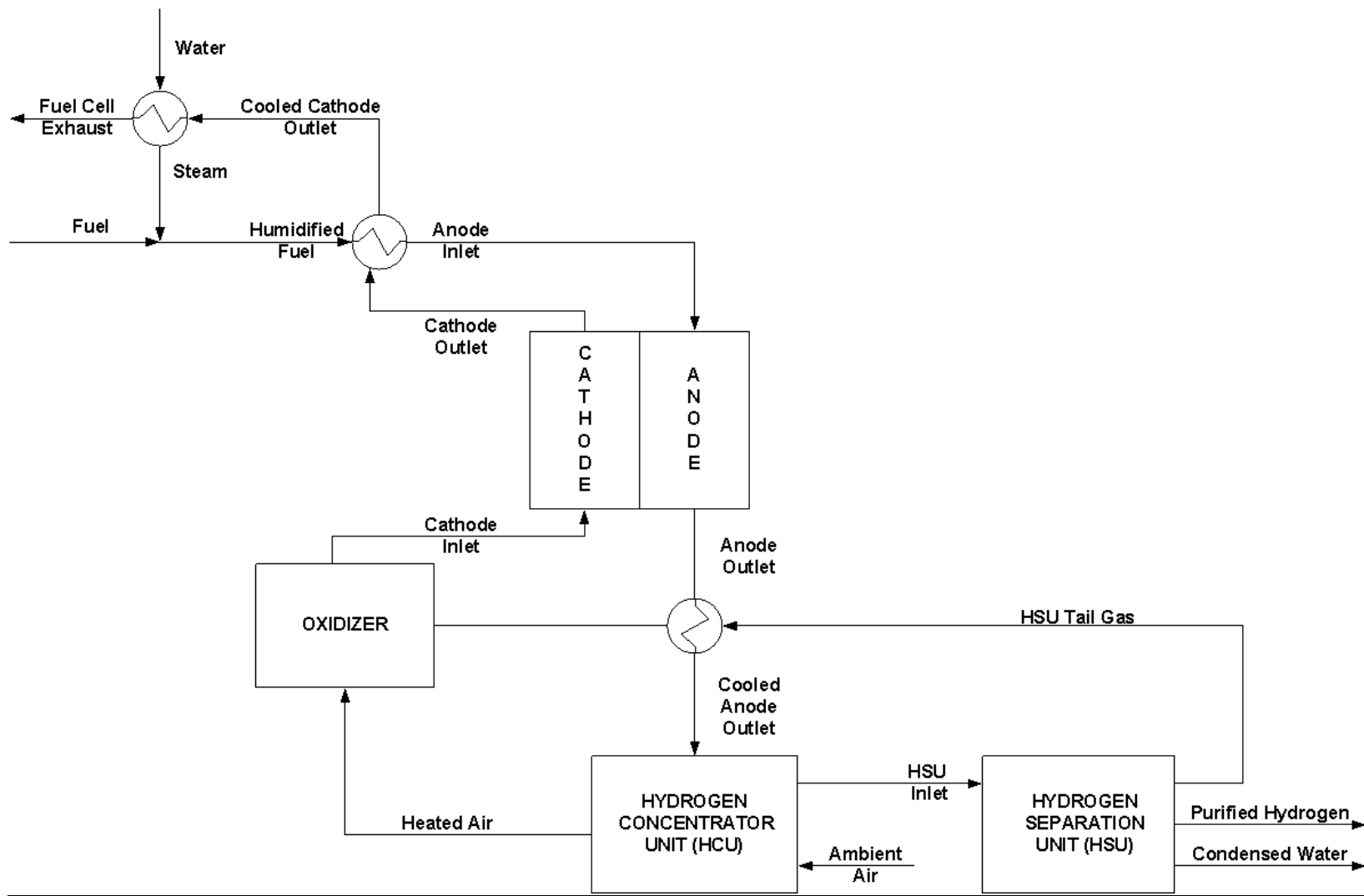


Figure 6. General process flow diagram of modeled tri-generation system

The modeled tri-generation system in Figure 6 operated in the following manner:

- 1) Humidified fuel entered the anode compartment of the fuel cell.
- 2) The anode outlet was cooled to an appropriate temperature for the HCU by transferring heat to the HSU Tail Gas in a heat exchanger.
- 3) The cooled anode outlet was shifted and cooled in the HCU.
- 4) The cooled and shifted anode outlet entered the HSU, where the stream was compressed to the PSA operating pressure and cooled by an electric chiller to the PSA operating temperature.
- 5) The hydrogen separated from the anode outlet was exported.
- 6) The cooled, hydrogen-depleted anode exhaust leaves the HSU as the HSU Tail Gas and is heated by the hot anode outlet stream before entering the oxidizer.
- 7) Ambient air is heated inside the HCU and routed to the oxidizer.
- 8) The heated HSU Tail Gas and warm air reacted in the oxidizer and exits as the fuel cell oxidant.
- 9) The cathode inlet, which is commonly referred to as the fuel cell oxidant, entered the cathode at the appropriate conditions for the cathodic molten carbonate electrochemical reaction.
- 10) The cathode outlet was used to heat the humidified fuel stream entering the anode. The cooled cathode outlet was then used to heat the water used to humidify the fuel.
- 11) (not shown) Portion of the condensed water exiting HSU is recycled to humidify fuel.

## 4.3 Process Models

The following sections describe the methods used to simulate each component of the DFC<sup>®</sup> molten carbonate tri-generation system using Aspen Plus<sup>®</sup>.

### 4.3.1 Molten Carbonate Fuel Cell

The modeled molten carbonate fuel cell system in this study aimed to accurately characterize the performance of molten carbonate fuel cell technology developed by FuelCell Energy, particularly operating at conditions that enabled the tri-generation of hydrogen, electricity, and heat. Capturing the attributes of a DFC<sup>®</sup> system proved to be an extensive modeling effort that is reflected in the following 11 sub-sections. Although chemical and physical processes occurred simultaneously in the fuel cell stack, the processes were separately simulated in Aspen Plus<sup>®</sup> by implementing various calculation methodologies. Before delving into the various modeling strategies described in the next 11 sub-sections, the assumptions for the fuel cell model must first be identified. Thus, the following assumptions were employed:

#### **Assumptions:**

- Anode and cathode compartments operated at same pressure, therefore the stack pressure was equivalent;
- Negligible pressure drop in anode and cathode compartments;
- Ion transport sufficiently fast enough to assume no mass storage;
- Equi-potential electrode surface;
- Only hydrogen electrochemically reacted in anode and contributed to voltage;
- steam methane reforming reaction reached chemical equilibrium;



- every fuel cell operated at the same temperature of 676.7 °C, which is justified by the steady-state temperature profile modeled by Luke et al. [39];
- temperature distribution was uniform throughout fuel cell;
- The anode and cathode temperatures are equal [40];
- Nernst potential was independent of hydrostatic pressure graduations;
- Water-gas shift equilibrium reaction reached chemical equilibrium;
- Carbon monoxide in anode participated in water-gas shift reaction only, not electrochemical oxidation, because the water-gas shift rate of reaction is faster than electrochemical oxidation;
- Heat exchange between adjacent cells is negligible;
- Fuel cell stack was adiabatic due to the practical design consideration of insulating high-temperature equipment;
- The bulk model does not spatially resolve the temperature distribution along the cell.

#### *4.3.1.1 Internal Reformation*

Fuel processing is necessary for all types of fuel cells. Internal reformation is possible with high-temperature fuel cells. The way that the fuel is reformed internally depends on the stack design. FuelCell Energy has developed a stack design for its DFC<sup>®</sup> products that incorporates indirect and direct internal reformation. However, external reformation is still necessary for high-temperature fuel cells for certain fuels. The external reformer for an internal reforming high-temperature fuel cell may not need to be as substantial in duty or footprint, as less reformation is needed. A pre-reformer is typically used alongside DFC<sup>®</sup> products for several

reasons that will be discussed below. The fuel cell model in this study aimed to replicate the internal reformation stack design commonly used by FCE, which is illustrated in Figure 7 [41] below, as well as a generic pre-reformer for fuel-flexibility.

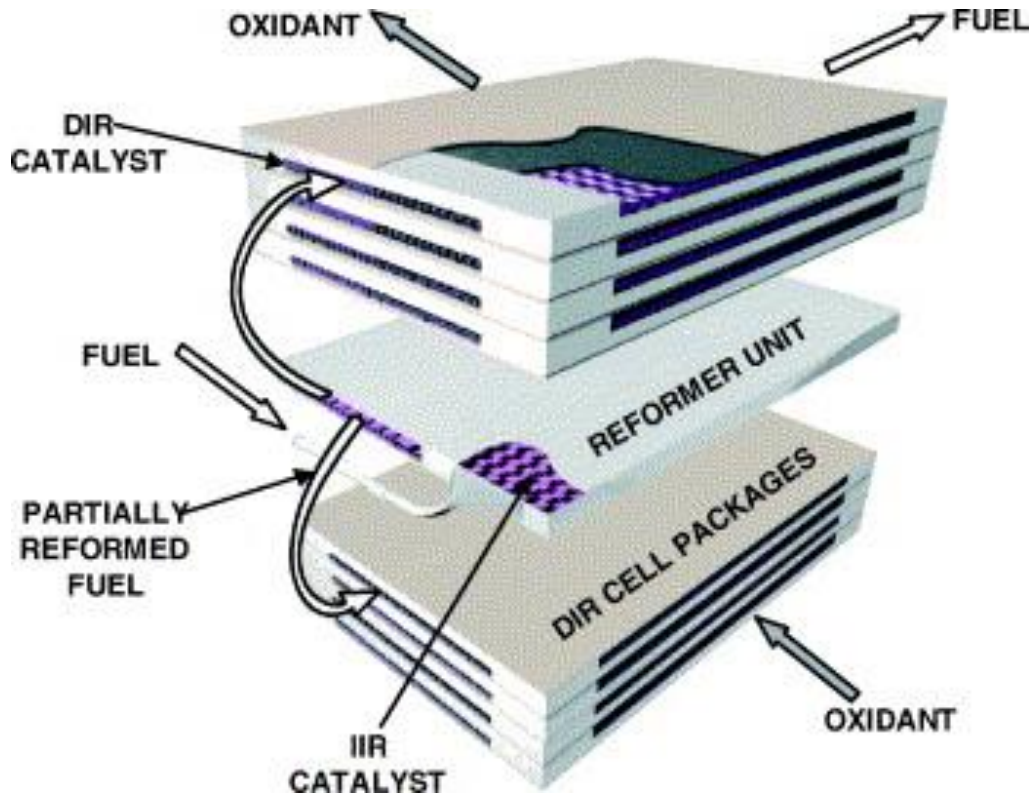


Figure 7. FuelCell Energy Direct FuelCell® stack design [41]

Indirect internal reformation (IIR) takes place in a reformer unit (RU) containing nickel-based catalyst (IIR catalyst in Figure 7) every 10 fuel cells in the stack. IIR occurs in the absence of electrochemical reactions [40] in an effort to extend catalyst life without compromising the thermal management benefits [42] of internal reformation. Approximately 50—60 percent of the

fuel is converted to hydrogen in the IIR step before entering the fuel cell anode compartment [40]. The partially reformed fuel or “reformat” from the IIR step is further reformed in the anode compartment by direct internal reformation (DIR). This process is shown schematically in Figure 7: the partially reformed fuel enters the anode compartment of each fuel cell in the DIR cell package. The anode is loaded with DIR catalyst that promotes both the reformation and electrochemical reactions. The hydrogen produced in the anode and IIR plate is consumed by the electrochemical reaction in the anode.

#### *4.3.1.2 Thermal Management of Fuel Cell Stack*

The reformation reaction is endothermic and consumes the heat released by the exothermic electrochemical reactions. Balancing internal reformation and electrochemical reactions is a significant thermal management strategy for the fuel cell stack [42]. A schematic of the sources of heat generation and consumption in an internal reforming molten carbonate fuel cell can be seen in Figure 8.

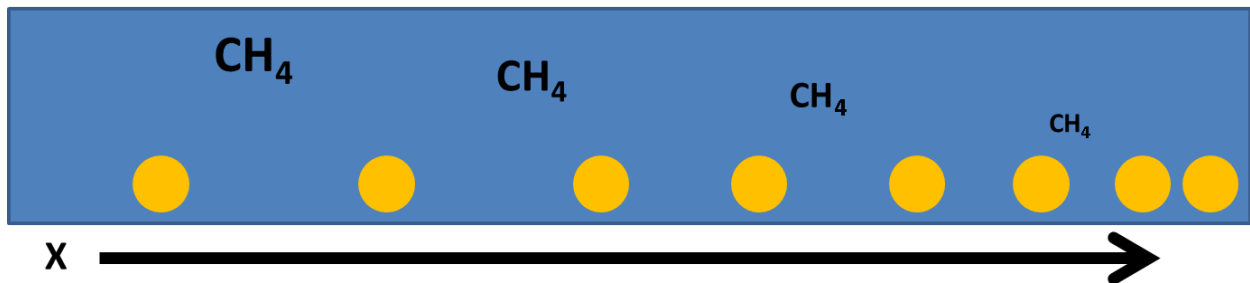
<b>Reformation Reaction</b> <b>Endothermic</b>	$\text{CH}_4 + \text{H}_2\text{O} \rightarrow 3\text{H}_2 + \text{CO}$	<b>REFORMING UNIT (RU) &amp; ANODE</b>
<b>Water-Gas Shift Reaction</b> <b>Slightly Exothermic</b>	$\text{CO} + \text{H}_2\text{O} \rightarrow \text{H}_2 + \text{CO}_2$	
<b>Fuel Cell Reaction</b> <b>Exothermic</b>	$2\text{H}_2 + 2\text{CO}_3^{2-} \rightarrow 2\text{H}_2\text{O} + 2\text{CO}_2 + 4\text{e}^-$	<b>ANODE</b>
<b>Electrolyte</b>		
<b>Fuel Cell Reaction</b> <b>Exothermic</b>	$\text{O}_2 + 2\text{CO}_2 + 4\text{e}^- \rightarrow 2\text{CO}_3^{2-}$	<b>CATHODE</b>

**Figure 8. Reaction chemistry in an internal reforming molten carbonate fuel cell**

The reformation reaction occurring in the reforming unit and anode (shown together in Figure 8) are endothermic and occur quickly. The exothermic electrochemical fuel cell reactions take place further along the cell and provide heat to the endothermic reformation reactions chemistry shown in Figure 8. These reaction qualities are important to note, as they influence the fuel cell and stack design, as well as the stack thermal management strategy.

Non-uniform catalyst loading of DIR catalyst is a notable example of a thermal management strategy that affected the design of the anode electrode. Direct internal reformation occurs across the anode compartment with the assistance of reforming catalyst. The reformate quickly reacts at the entrance of the anode, decreasing the temperature at the anode inlet. As a result, the exothermic electrochemical reactions increase the temperature further along the anode. Fast reforming reaction rates at the anode inlet and very little reforming at the anode exit resulted in large temperature gradients in the cell. As a result, incorporating DIR highly complicates

thermal management in the stack. FuelCell Energy integrated non-uniform reforming catalyst distribution in its anode design as a thermal management strategy [43]. Reforming catalyst were placed further along the cell as a means to decelerate reforming reaction at anode inlet and achieve heat balance. Figure 9 is a schematic that reiterates the result of distributing reforming catalyst in a non-uniform fashion.



**Figure 9. Schematic of non-uniform catalyst distribution along the length of an anode**

The yellow circles represent the reforming catalyst, the blue rectangle represents the anode, and “CH<sub>4</sub>” represents methane concentration in the anode. The reforming catalyst is concentrated at the anode exit, allowing for the methane concentration to gradually decrease over the length of the anode. Thus, the non-uniform catalyst distribution method ensures that the steam methane reforming, water-gas shift, and electrochemical reactions ensue along the length of the anode.

#### *4.3.1.3 Pre-Reformer Model*

Internal reformation eliminates the use of an external reformer or “pre-reformer” for methane-rich fuels. A pre-reformer is necessary for fuels composed of C<sub>2</sub> and higher

hydrocarbons. Although natural gas is mostly composed of methane (C1), it also contains 1 to 4 percent of higher hydrocarbons that can promote coking on the reforming catalyst [42]. Pre-reforming of natural gas at 400—500 °C breaks down higher hydrocarbons and produces hydrogen that keeps internal reforming catalyst in a reducing environment [42]. The purpose of the pre-reformer is to convert 100 percent of the higher hydrocarbons to methane to avoid coking on downstream reforming catalyst without reforming a significant amount of hydrogen [42].

A pre-reformer was incorporated into the fuel cell system, since one of the operating fuels, natural gas, contained concentrations of ethane and propane that could not be neglected. Also, pre-reformers are already integrated in FuelCell Energy systems due to its practical and frequent necessity. The REquil reactor unit in Aspen Plus<sup>®</sup> was used to model the pre-reformer because the partially reformed fuel is at or very close to equilibrium [42]. REquil reactors should be used when reaction stoichiometry is known and all reactions reach equilibrium. The following five reactions shown in Table 7 were specified to reach equilibrium in the REquil reactor simulating the pre-reformer.

**Table 7. Reactions accounted for in the IIR equilibrium reactor**

Reaction Name	Reaction Stoichiometry
Steam Methane Reformation	$\text{CH}_4 + \text{H}_2\text{O} \rightarrow \text{CO} + 3 \text{H}_2$
Steam Ethane Reformation	$\text{C}_2\text{H}_6 + 2 \text{H}_2\text{O} \rightarrow 2 \text{CO} + 5 \text{H}_2$
Steam Propane Reformation	$\text{C}_3\text{H}_8 + 3 \text{H}_2\text{O} \rightarrow 3 \text{CO} + 7 \text{H}_2$
Water-Gas Shift	$\text{CO} + \text{H}_2\text{O} \rightarrow \text{CO}_2 + \text{H}_2$
Methanation	$\text{CO} + 3 \text{H}_2 \rightarrow \text{CH}_4 + \text{H}_2\text{O}$

The REquil unit also requires operating conditions and valid phases in order to solve stoichiometric chemical and phase equilibrium equations. The following operating conditions were assumed for the pre-reformer:

- Vessel operates at 15.4 psia
- Isobaric
- Adiabatic
- Inlet fuel always enters at 500 °C
- Inlet and outlet stream always in vapor phase

The partially reformed fuel exits the pre-reformer at a lower temperature because the endothermicity of the reformation reactions are always much greater than the exothermicity of the water-gas shift and methanation reaction. It must be heated to the set point temperature for the anode inlet. The cathode exhaust was used to further heat the partially reformed fuel through a heat exchanger.

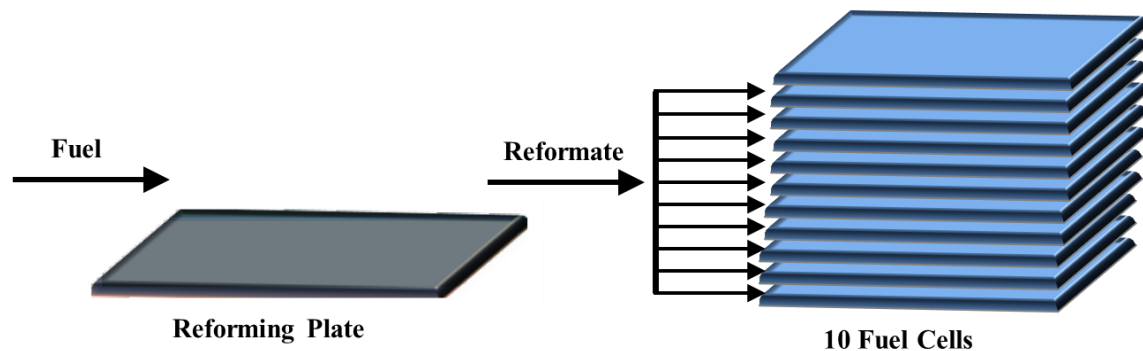
#### *4.3.1.4 Simplified Fuel Cell Stack Model*

In order to model FuelCell Energy's molten carbonate fuel cell system, internal reformation needed to be incorporated into the fuel cell model. The DFC<sup>®</sup> stack was designed to indirectly reform the fuel internally via reforming unit placed between every 10 fuel cells in the stack. The partially reformed fuel exiting the reforming unit enters the anode to be further reformed through direct internal reformation and electrochemically oxidized.

Many researchers have employed empirical data gathered from single cell tests to extrapolate fuel cell stack performance [10, 15, 17, 21, 44, 45, 46]. In other words, fuel cell studies have scaled up single representative cell models to describe the entire stack performance. That approach was taken to model the DFC<sup>®</sup> stack design. However, indirect internal reformation posed as a complication to the use of the single cell modeling approach.

Indirect internal reformation was incorporated in the single fuel cell model by a series of logical assertions.

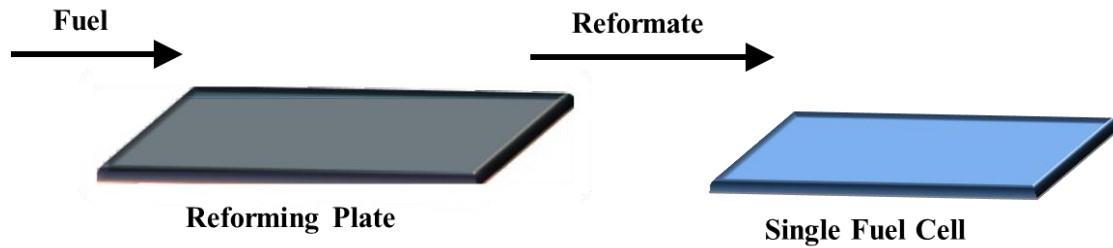
Figure 10 depicts ten fuel cells receiving partially reformed fuel from a single



**Figure 10. FuelCell Energy DFC<sup>®</sup> stack design shown for a single group of fuel cells**

reforming unit. Dozens of these reforming unit/fuel cell groups are assembled in series to form a single DFC<sup>®</sup> stack. It can be assumed that each of these groups perform identically and the stack performance is proportional to the number of reforming unit/fuel cell groups composing the stack. Further simplifying the reforming unit/fuel cell group into a reforming unit with a single cell, as seen in Figure 11, would greatly reduce the rigor of the model without significantly reducing its robustness.





**Figure 11. DFC<sup>®</sup> design simplified as single fuel cell grouped with reforming unit**

In single fuel cell modeling, the fuel and oxidant flow rate, composition, temperature, pressure, and other chemical properties are assumed to be identical for every cell. In the same manner, it was assumed that the reformate entering each cell, as illustrated in

Figure 10, was uniform. Also, each fuel cell in the reforming unit/fuel cell group is assumed to perform identically by the same reasoning used for single fuel cell models. If the partially reformed fuel entering each fuel cell was identical in composition and each fuel cell performed identically, then it may be assumed that a reforming unit and single fuel cell can represent a reforming unit/fuel cell group, as seen in Figure 11. A stack can then be considered an aggregate of these identical fuel cells with performance and stream properties scaled to the number of cells.

#### ***4.3.1.5 Indirect Internal Reformation Model***

The model simulated indirect internal reformation in the fuel cell stack using a single reformer unit based on reasons discussed in 4.3.1.4 Simplified Fuel Cell Stack Model. The reforming unit was represented by the Aspen Plus<sup>®</sup> REquil reactor unit. The REquil reactor for the reforming unit was set up almost exactly like the pre-reformer discussed in 4.3.1.3 Pre-

Reformer Model. The same reactions listed in Table 7 were used. The following operating conditions were assumed for the reforming unit:

- Vessel operates at 15.4 psia
- Isobaric
- Vessel operates at fuel cell stack temperature of 676.7 °C
- Isothermal
- Inlet fuel always enters at fuel cell stack temperature
- Inlet and outlet stream always in vapor phase

The stream exiting the pre-reformer was heated to the fuel cell stack temperature before being reformed further in the reforming unit. The resulting reformat stream enters the anode at the fuel cell stack temperature. Since the reactor operating temperature and inlet and outlet stream temperature are equal, the heat generated or consumed must come from the surroundings to meet the reactor operating conditions. Since the reformation reactions are endothermic, heat must be provided to the reforming unit in order for the outlet stream temperature to equal the inlet stream temperature. That heat needed for the endothermic reactions was assumed to come from the heat generated by the fuel cell electrochemical reactions, which is true to actual DFC<sup>®</sup> thermal management of the IIR and fuel cells.

#### *4.3.1.6 Direct Internal Reformation Model*

The reformat entering the single fuel cell was channeled to the anode compartment. Direct internal reformation occurs across the anode compartment with the assistance of reforming catalyst. Since DIR and IIR are describe the same process at different locations in the

fuel cell stack, both internal reformation stages were modeled the same way. The DIR model is placed after the calculator block modeling the electrochemical reaction occurring at the anode.

#### *4.3.1.7 Previous Research: Fuel Cell Modeling using Aspen Plus®*

Previous fuel cell models using Aspen Plus® software simulated internal reformation and fuel cell electrochemistry using process operation model reactors such as REquil and RGibbs and calculator blocks. Kivisarri et al. [44] modeled an internal reforming molten carbonate fuel cell system in Aspen Plus®. He assumed that both the steam methane reformation and water-gas shift reaction were carried out irreversibly to the right in a reactor model, resulting in the anode inlet stream containing zero methane and carbon monoxide. The anode and cathode are modeled using the same reactor process model. The anode exhaust entered a RGibbs reactor for the purpose of reestablishing water-gas shift and steam methane reformation equilibrium.

Li et al. [45] used a similar approach when modeling an internal reforming solid oxide fuel cell system in Aspen Plus®. He used a RGibbs reactor to model internal reformation. The methane reformation and water-gas shift reaction were assumed to have reached equilibrium at the same temperature as the inlet anode stream. Assuming the SMR and WGS reactions reach equilibrium is a more realistic approach instead of complete conversion adopted by Kivisarri et al. The equilibrium concentration of hydrogen in the anode fed will always be equal or smaller than the concentration of hydrogen resulting from complete conversion of carbon monoxide and methane. Therefore, performance variables like voltage, power, efficiency, heat generation, and exhaust compositions will not be accurate regardless of a downstream equilibrium reactor incorporated in fuel cell system modeled by Kivisarri et al. The electrochemical reactions are

also modeled differently. Li et al. used a calculator block to determine the outlet cathode and anode stream composition based on a pre-defined fuel utilization factor. Like Kivisarri et al., a RGibbs equilibrium reactor was used to correct the composition of the outlet stream and bring it to equilibrium. Li et al. further explained that using an equilibrium reactor was also necessary to compensate for the limitations of the method used to replicate the electrochemical reactions. The fuel species were consumed proportionally due to calculation of outlet species concentration solely being based on the fuel utilization factor. Whereas, the rate at which each constituent was actually consumed in a real anode varies and is not solely dependent on fuel utilization.

#### *4.3.1.8 Anode Discretization*

Modeling a FuelCell Energy fuel cell system using the methodologies described in 4.3.1.7 Previous Research: Fuel Cell Modeling using Aspen Plus<sup>®</sup> would neglect the key features of the technology. The desire to incorporate direct internal reformation and non-uniform reforming catalyst distribution led to investigation of accurately modeling DIR in the anode with Aspen Plus<sup>®</sup>.

Due to the non-uniform catalyst distribution along the length of an anode (refer to 4.3.1.2 Thermal Management of Fuel Cell Stack), reforming, water-gas shift, and electrochemical reactions simultaneously transpire along the length of the anode. All three sets of reactions are interdependent: a product in one reaction is a reactant in another. For example, the water produced by electrochemical oxidation drives the steam methane and water-gas shift reactions forward based on Le Châtelier's principle for a system at equilibrium. The resulting hydrogen is utilized further along the anode and produces water vapor before the anode exit. Since

equilibrium compositions are dependent on concentration, equilibrium for the stream shifts along the length of the anode. Therefore, modeling DIR and electrochemical reactions separately in whatever order introduces an error in the calculation of the exhaust composition. Introducing non-dimensional discretization of the anode is one modeling strategy to better capture the simultaneous reactions in the anode and minimize the error in the calculated exhaust stream composition.

Non-dimensional discretization of a system has been modeled before. De Simon et al. [46] employed non-dimensional discretization in an Aspen Plus<sup>®</sup> model to more accurately represent the simultaneous processes that occurred in a “modular integrated reformer” using several built-in operation models. A modular integrated reformer was a reformer and catalytic burner assembled together. The unit was modeled by dividing the modular integrated reformer into four parts in order to simulate three simultaneous processes: steam methane reforming, catalytic oxidation, and heat exchange. The discretized model approximated the performance of the modular integrated reformer well according to De Simon et al.

This study hypothesized that non-dimensional discretization of the anode would better approximate the simultaneous reactions occurring in the anode compartment of a FCE DFC<sup>®</sup> system. The anode was broken into two phases. The first phase included all of the DIR reactions, which were listed in Table 7. The second phase included the electrochemical oxidation of hydrogen, which was shown in Equation (2-28). The combination of two phases represented a non-dimensional portion of the anode compartment. Although the discretization is non-dimensional, each portion of the anode characterized a stage of progress for the simultaneous reactions or, in other words, the extent of reaction in the anode. All of the reactions are promoted

along the entire length of the anode, thus the extent to which the species react reflect physically how far along the species are in the anode. The first combination of the two phases was considered the first stage of the anode. Each sequential combination was associated with a stage of greater total reactant consumption. The final design of the anode compartment consisted of seven modeled stages where electrochemical and DIR reactions occurred. The seven-stage anode design was evaluated by comparing the last anode exhaust composition to the last DIR exhaust composition. The two exhaust stream compositions were identical. The comparison between a single-stage anode exhaust composition and DIR exhaust composition was drastically different. The single-stage DIR exhaust actually contained much more hydrogen and carbon dioxide. That indicated that not enough reformation occurred in the IIR step and that the anode exhaust was far from equilibrium. The cathode, however, does not need to be discretized because it is assumed that only the electrochemical reduction of hydrogen takes place in the cathode. And since the molten carbonate fuel cell has the unique electrochemistry that utilizes the anode exhaust as the cathode feed, any steam composition improvements in the anode compartment positively affects the accuracy of the cathode exhaust composition. Further discussion and verification of the anode discretization scheme will take place in 5.1 Verification of FuelCell Energy Direct FuelCell<sup>®</sup> Model.

#### *4.3.1.9 Electrochemistry*

Aspen Plus<sup>®</sup> does not have the capability of physically representing a fuel cell nor does it solve fuel cell electrochemistry material and energy balances. Calculator blocks in Aspen Plus<sup>®</sup> provided a means to compensate for the anode and cathode electrochemical reactions artificially. The electrode reaction stoichiometry and fuel utilization factor determined the composition of

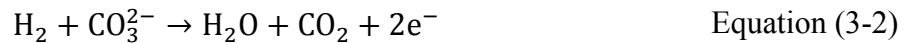
the exhaust. This method to modeling the electrochemical reactions of the molten carbonate fuel cell model is similar in fashion as the reforming solid oxide fuel cell system Li et al studied.

The definition of fuel utilization,  $U_F$ , is the ratio of hydrogen reacted in the cell to the total amount of hydrogen fed to the anode, which is shown in Equation (3-1).

$$U_F = \frac{\dot{N}_{H_2 IN} - \dot{N}_{H_2 OUT}}{\dot{N}_{H_2 IN}} \quad \text{Equation (3-1)}$$

The molar flow rate of hydrogen entering the anode is  $\dot{N}_{H_2 IN}$  and the exiting hydrogen rate is  $\dot{N}_{H_2 OUT}$ . The difference between the two quantities represents the amount of hydrogen electrochemically consumed at the anode, which is equivalent to the amount of carbon dioxide electrochemically consumed in the cathode. The anode compartment was separated into seven stages, where DIR and anode electrochemical reactions occurred at each stage. Each anode stage operates at the same temperature and fuel utilization. The fuel utilization specified by the user in the model.

Equation (3-2) illustrates the electrochemical reaction that occurs in the anode:



The molar flow rate of each species in the anode exhaust was calculated stoichiometrically based on the electrochemical reaction shown above and fuel utilization. The following equations were programed into each anode calculator block:

$$\dot{N}_{H_2_{OUT}} = \dot{N}_{H_2_{IN}}(1 - U_F) \quad \text{Equation (3-3)}$$

$$\dot{N}_{CO_2_{OUT}} = \dot{N}_{CO_2_{IN}} + \dot{N}_{H_2_{IN}}(U_F) \quad \text{Equation (3-4)}$$

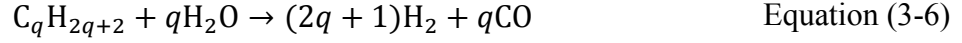
$$\dot{N}_{H_2O_{OUT}} = \dot{N}_{H_2O_{IN}} + \dot{N}_{H_2_{IN}}(U_F) \quad \text{Equation (3-5)}$$

where  $\dot{N}_{CO_2_{IN}}$  is the molar flow rate of carbon dioxide entering the anode and  $\dot{N}_{H_2O_{IN}}$  is the molar flow rate of steam entering the anode. All other molecules entering the anode do not react and exit at the same rate. Although methane is reformed in the anode, the reaction is not included in the user-defined calculator block representing the anode due to the assumption that the DIR reactions are accurately modeled by a REquil equilibrium reactor described in 4.3.1.6 Direct Internal Reformation Model. The calculator block is used to only compensate for physical and chemical processes that extend beyond the capabilities of Aspen Plus<sup>®</sup>. The anode calculator block similarly neglects the water-gas shift of carbon monoxide, since it is accounted for in the same reformation equilibrium reactors.

The cathode is a single calculator block. The same approach is taken to determine the exhaust composition. The utilization factor used in the cathode calculation differs from the utilization factor specified as an input and basis of the anode exhaust calculation. In fact, the actual fuel utilization is not equal to the specified fuel utilization input, but to the sum the hydrogen electrochemically reduced through each anode stage divided by the maximum quantity of hydrogen produced by reformation.



The maximum production of hydrogen depends on the thermodynamics of the steam methane reformation and water-gas shift reaction at specified operating conditions. The general steam reformation is presented in Equation (3-6):



for saturated hydrocarbons, also known as alkanes. Saturated hydrocarbons have the molecular form  $C_qH_{2q+2}$ , where  $q$  is a whole number. The water-gas shift reaction that commonly accompanies the steam reformation reaction is depicted below as Equation (3-7):



The hydrogen produced from direct internal reformation is described in Equation (3-8):

$$\dot{N}_{H_2 IN,REF} = \sum_{q=1}^r (2q + 1) \left[ \dot{N}_{C_qH_{2q+2} IN} - \dot{N}_{C_qH_{2q+2} OUT} \right] \quad \text{Equation (3-8)}$$

where molar flow rate of the alkane entering the anode is  $\dot{N}_{C_qH_{2q+2} IN}$  and molar flow rate of the alkane exiting the anode is  $\dot{N}_{C_qH_{2q+2} OUT}$ . The expression,  $(2q + 1)$ , corresponds to the generic stoichiometric yield of hydrogen for an alkane reformed. This quantity is calculated for each modeled anode stage.

The hydrogen generated from the water-gas shift reaction is described in Equation (3-9):

$$\dot{N}_{H_2 IN,WGS} = \dot{N}_{CO IN} - \dot{N}_{CO OUT} \quad \text{Equation (3-9)}$$

The inlet carbon monoxide flow rate,  $\dot{N}_{CO IN}$ , is defined as:

$$\dot{N}_{CO\ IN} = \dot{N}_{CO\ FUEL} + \dot{N}_{CO\ REF} \quad \text{Equation (3-10)}$$

where  $\dot{N}_{CO\ FUEL}$  is the molar flow rate of CO innate to the fuel and  $\dot{N}_{CO\ REF}$  the carbon monoxide molar flow rate generated from all reformation reactions. Equation (3-11) presents the stoichiometric relationship between  $\dot{N}_{CO\ REF}$  and reformation reactions.

$$\dot{N}_{CO\ REF} = \sum_{q=1}^r q \left[ \dot{N}_{C_q H_{2q+2}\ IN} - \dot{N}_{C_q H_{2q+2}\ OUT} \right] \quad \text{Equation (3-11)}$$

Substituting Equation (3-11) and Equation (3-10) into Equation (3-9) defines the hydrogen yield via water-gas shift reaction in Equation (3-12).

$$\dot{N}_{H_2\ IN, WGS} = \dot{N}_{CO\ FUEL} + \sum_{q=1}^r q \left[ \dot{N}_{C_q H_{2q+2}\ IN} - \dot{N}_{C_q H_{2q+2}\ OUT} \right] - \dot{N}_{CO\ OUT} \quad \text{Equation (3-12)}$$

The total hydrogen that can be electrochemically consumed in the anode is the sum of the hydrogen produced by reformation and water-gas shift. Thus, the sum of Equation (3-8) and Equation (3-12) results in the total hydrogen available to the entire anode,  $\dot{N}_{H_2\ IN, TOTAL}$ , which is shown below as Equation (3-13).

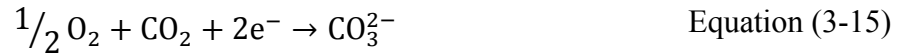
$$\dot{N}_{H_2\ IN, TOTAL} = \sum_{q=1}^r (3q + 1) \left[ \dot{N}_{C_q H_{2q+2}\ IN} - \dot{N}_{C_q H_{2q+2}\ OUT} \right] + \dot{N}_{CO\ FUEL} - \dot{N}_{CO\ OUT} \quad \text{Equation (3-13)}$$

The actual or real fuel utilization,  $U_{F\ Real}$ , is defined as:

$$U_{F\ Real} = \frac{\left( \sum_{m=1}^n \dot{N}_{H_2\ m\ IN} \right) U_F}{\sum_{q=1}^r (3q + 1) \left[ \dot{N}_{C_q H_{2q+2}\ IN} - \dot{N}_{C_q H_{2q+2}\ OUT} \right] + \dot{N}_{CO\ FUEL} - \dot{N}_{CO\ OUT}} \quad \text{Equation (3-14)}$$

where  $\dot{N}_{H_2 IN}^m$  is the amount of hydrogen entering stage  $m$  of the anode. The numerator represents the quantity of hydrogen electrochemically reacted in throughout the entire anode compartment.

The calculator block for the cathode electrochemical reaction is executed after the anode calculator blocks are run and a value for the real fuel utilization has been calculated. A reminder of the cathode electrochemical reaction is shown in Equation (3-15) below.



The calculated real fuel utilization determines the percentage of oxygen and carbon dioxide react in the cathode. The cathode exhaust molar flow rates are calculated as such:

$$\dot{N}_{O_2 OUT} = \dot{N}_{O_2 IN} - \dot{N}_{H_2 IN} (U_{FREAL}) \quad \text{Equation (3-16)}$$

$$\dot{N}_{CO_2 OUT} = \dot{N}_{CO_2 IN} - \frac{1}{2} \dot{N}_{H_2 IN} (U_{FREAL}) \quad \text{Equation (3-17)}$$

Lastly, to achieve mass balance, the quantity of carbonate ions reacting in the anode compartment must be equal to the number of carbonate ions that are generated at the cathode. The rate of consumption and generation is equal by definition of steady state operation. Although the carbonate ion was not included in the model and many calculator blocks stood to represent the fuel cell electrochemistry via user-defined mass balances, the model always achieved mass balance.

#### 4.3.1.10 Voltage

The voltage was calculated first for a single direct internal reforming fuel cell based on the simplified fuel cell stack model discussed in 4.3.1.4. The fuel cell system voltage was not calculated directly since the known voltage for a single fuel cell is representative of the fuel cell stack performance. However, electricity was calculated based on the fuel cell voltage and fuel utilization, which will be discussed in 4.3.1.11 Power Generation and Parasitic Loads. The calculations determining the fuel cell voltage was programmed into an Aspen Plus<sup>®</sup> user-defined calculator block and will be detailed below.

The reversible cell voltage was calculated using the average fuel cell stack temperatures, averaged partial pressure for each species in the anode and cathode compartments, and computed standard-state reversible open circuit voltage. However, an operational fuel cell undergoes irreversible losses that reduce the reversible voltage. As a result, polarization equations needed to be incorporated into the voltage calculator block to compute the fuel cell operating voltage. Polarization equations that characterize losses in the DFC<sup>®</sup> fuel cell have not been published and challenged the objective of the study to predict the performance of the tri-generation system for varying operating conditions. Instead, polarization equations for a molten carbonate fuel cell stack manufactured by Ishikawajima-Harima Heavy Industries Co. Ltd (IHI), not FuelCell Energy, were used as an initial method to describe the losses in the DFC<sup>®</sup> fuel cell. Yoshida et al. [47] published the expressions for internal, anode reaction, and cathode reaction resistance separately that characterized the irreversible losses associated with the IHI 10 kW molten carbonate fuel cell. Table 8 lists the materials used to construct the fuel cell stack.

**Table 8. List of IHI 10-kW molten carbonate fuel cell stack components and materials [47]**

<b>Component</b>	<b>Material</b>
<b>Electrolyte / matrix</b>	$\text{Li}_2\text{CO}_3 / \text{Na}_2\text{CO}_3 = 60 / 40 \% / \text{LiAlO}_2$
<b>Anode / current collector</b>	Ni-AlCr alloy / Ni
<b>Cathode / current collector</b>	In situ NiO / SUS316L

The materials used for the IHI molten carbonate fuel cell match the usual materials used for the DFC<sup>®</sup> fuel cell according to Hilmi et al. [48]. Although it is widely recognized that lithium and potassium or lithium and sodium carbonate mixtures are molten salts commonly used for molten carbonate fuel cell electrolytes, the exact composition of the DFC<sup>®</sup> electrolyte for the installed MCFC tri-generation system is unknown. Furthermore, based on FCE published materials, it does not seem like the DFC<sup>®</sup> electrolyte composition has been standardized due to continuous and swift improvements in fuel cell materials development and integration.

It is assumed that the installed 300 kW DFC<sup>®</sup> at OCS D uses a conventional molten carbonate fuel cell electrolyte eutectic mixture of 52 mol-% lithium carbonate ( $\text{Li}_2\text{CO}_3$ ) and 48 mol-% sodium carbonate ( $\text{Na}_2\text{CO}_3$ ). Cathode polarization for the stated electrolyte mixture was obtained from the FuelCell Energy patent application US2012/0021328 A1 [49] as a base-case reference, confirming that FCE once used the conventional eutectic mixture. The installed fuel cell stack was refurbished before undergoing alpha-testing in the 2009-2010 timeframe and state-of-the-art MCFC electrolyte mixtures discussed in US2012/0021328 A1 [49] were most likely not incorporated into the circa 2009 commercial DFC<sup>®</sup> systems. Thus, the 52- $\text{Li}_2\text{CO}_3$ /48- $\text{Na}_2\text{CO}_3$

electrolyte is a pragmatic and conservative assumption for this study, but it may also limit the range of valid predications for the MCFC tri-generation system installed at OCSD.

The assumed correct electrolyte eutectic mixture of 52-Li<sub>2</sub>CO<sub>3</sub>/48-Na<sub>2</sub>CO<sub>3</sub> is slightly different in composition from the IHI electrolyte mixture of 60-Li<sub>2</sub>CO<sub>3</sub>/40-Na<sub>2</sub>CO<sub>3</sub>. The cathode polarization found in the patent application provides an opportunity to compare the modeled cathode resistance for a 60-Li<sub>2</sub>CO<sub>3</sub>/40-Na<sub>2</sub>CO<sub>3</sub> electrolyte to actual data for a 52-Li<sub>2</sub>CO<sub>3</sub>/48-Na<sub>2</sub>CO<sub>3</sub> electrolyte and gauge the difference in performance between the two electrolyte mixtures. “Fig. 7” from the FuelCell Energy patent application US2012/0021328 A1 [49] showed the cathode polarization to be approximately 0.075 volts at 650 °C and a current density of 160 A/m<sup>2</sup> for a DFC<sup>®</sup> fuel cell with a 52-Li<sub>2</sub>CO<sub>3</sub>/48-Na<sub>2</sub>CO<sub>3</sub> electrolyte. It is anticipated that greater loss will be seen in the cathode for a 52-Li<sub>2</sub>CO<sub>3</sub>/48-Na<sub>2</sub>CO<sub>3</sub> electrolyte versus the 60-Li<sub>2</sub>CO<sub>3</sub>/40-Na<sub>2</sub>CO<sub>3</sub> electrolyte. The stability of the cathode is affected by the electrolyte mixture because of chemical interactions between the cathode electrode and electrolyte. The common cathode electrode, lithiated nickel oxide (NiO), can dissolve slowly by reacting with the electrolyte [48]. The NiO cathode is less soluble in more basic environments and simply increasing the concentration of lithium in the electrolyte decreases the dissolution of NiO electrode [50, 51]. The slightly higher concentration of lithium in the 60-Li<sub>2</sub>CO<sub>3</sub>/40-Na<sub>2</sub>CO<sub>3</sub> electrolyte was found to result in a lower solubility concentration of NiO at 0.3±0.05 μmole/ cm<sup>3</sup> in contrast to a NiO solubility concentration of 0.05 to 0.09 μmole/ cm<sup>3</sup> for the 52-Li<sub>2</sub>CO<sub>3</sub>/48-Na<sub>2</sub>CO<sub>3</sub> electrolyte [52]. Greater NiO dissolution negatively affects the cathode resistance and overall performance of the fuel cell [48], thus a factor will be used to increase the modeled cathode overpotential calculated through the cathode polarization expression suggested by

Yoshiba et al [47]. The multiplier will be determined through the verification process described in 5.2 Verification of Tri-generating FuelCell Energy Direct FuelCell®.

The fuel cell undergoes irreversible losses associated with activation, concentration, and ohmic polarizations. The polarization losses are dependent on temperature, current density, species partial pressures, cell materials, and many other conditions. Fuel cell operating cell voltage is commonly determined by adopting empirically-determined polarization loss equations. Many of these empirical relationships are dependent on species partial pressures, activation energy, and temperature, which are spatially distributed in an actual cell. These expressions are typically correlated with cell average quantities. The polarization loss expression for the cathode, anode, and internal resistance of the cell (also known as the ohmic polarization) used for this study are from Yoshiba et al.'s "Improvement of electricity generating performance and life expectancy of MCFC stack by applying Li/Na carbonate electrolyte: Test results and analysis of 0.44 m<sup>2</sup>/10-kW-and 1.03 m<sup>2</sup>/10kW-class stack" [47]. The cell voltage,  $V$ , that includes the irreversible losses is expressed in Equation (3-18) [47]:

$$V = E - (R_a + R_c + R_{ir})j \quad \text{Equation (3-18)}$$

where  $E$  is the Nernst voltage,  $R_a$  is the anode polarization,  $R_c$  is the cathode polarization,  $R_{ir}$  is the internal resistance, and  $j$  is current density. The Nernst voltage for the molten carbonate fuel cell is described in Equation (3-19).

$$E = E^o + \frac{RT}{2F} \ln \frac{p_{H_2,a} p_{O_2,c}^{1/2} p_{CO_2,c}}{p_{H_2O,a} p_{CO_2,a}} \quad \text{Equation (3-19)}$$

The anode polarization incorporated into the molten carbonate fuel cell simulation is as follows:

$$R_a = A_a T \exp\left(\frac{\Delta H_a}{RT}\right) p_{H_2,a}^{-1/2} \quad \text{Equation (3-20)}$$

where  $A_a$  is the frequency factor of anode resistance and  $\Delta H_a$  is the activation energy of anode resistance [47]. The cathode reaction resistance is expressed as:

$$R_c = A_{c1} T \exp\left(\frac{\Delta H_{c1}}{RT}\right) p_{O_2,c}^{-3/4} p_{CO_2,c}^{1/2} + \frac{A_{c2} T \exp\left(\frac{\Delta H_{c2}}{RT}\right)}{\left\{x_{CO_2,c} + A_{c3} x_{H_2O,c} \exp\left(\frac{\Delta H_{c3}}{RT}\right)\right\}} \quad \text{Equation (3-21)}$$

where  $x_{CO_2,c}$  is the molar fraction of  $CO_2$  in the cathode,  $x_{H_2O,c}$  is the molar fraction of  $H_2O$  in the cathode,  $A_{c1}$ ,  $A_{c2}$ ,  $A_{c3}$ , are frequency factors of cathode resistance, and  $\Delta H_{c1}$ ,  $\Delta H_{c2}$ ,  $\Delta H_{c3}$  are activation energies of cathode resistance [47]. The internal resistance, or ohmic loss, for the cell is independent of species partial pressure; it is described as a function of temperature as follows:

$$R_{ir} = A_{ir} \exp\left(\frac{\Delta H_{ir}}{RT}\right) \quad \text{Equation (3-22)}$$

where  $A_{ir}$  represents frequency factor of internal resistance and  $\Delta H_{ir}$  is the activation energy of internal resistance [47]. The frequency factors and activation energies were determined by correlating empirical data gathered from bench scale cell tests using an Arrhenius equation [47].

The parameters in Equations (3-20), (3-21), (3-22) are listed in Table 9.



**Table 9. Values of parameters appearing in empirical polarization equations [47]**

Parameter	Equation	Value	Units
$A_a$	3-20	$9.5 \times 10^{-11}$	$[\Omega \text{ m}^2 \text{ atm}^{0.5} \text{ K}^{-1}]$
$A_{c1}$	3-21	$6.91 \times 10^{-19}$	$[\Omega \text{ m}^2 \text{ atm}^{0.25} \text{ K}^{-1}]$
$A_{c2}$	3-21	$3.75 \times 10^{-13}$	$[\Omega \text{ m}^2 \text{ K}^{-1}]$
$A_{c3}$	3-21	$1.07 \times 10^{-10}$	[—]
$A_{ir}$	3-22	$1.38 \times 10^{-6}$	[—]
$\Delta H_a$	3-20	27.9	$[\text{kJ mol}^{-1}]$
$\Delta H_{c1}$	3-21	179.2	$[\text{kJ mol}^{-1}]$
$\Delta H_{c2}$	3-21	67.2	$[\text{kJ mol}^{-1}]$
$\Delta H_{c3}$	3-21	95.2	$[\text{kJ mol}^{-1}]$
$\Delta H_{ir}$	3-22	23.8	$[\text{kJ mol}^{-1}]$

#### 4.3.1.11 Power Generation and Parasitic Loads

The 300 kW Direct FuelCell<sup>®</sup> fuel cell stack houses approximately 400 fuel cells or 40 IIR-DIR combinations. The electric power for the fuel cell stack,  $P_e$ , is a product of total current generation and cell voltage, but it can also be calculated as follows:

$$P_e = V \cdot A_{stack} \cdot j \quad \text{Equation (3-23)}$$

where  $A_{stack}$  is the active area of the fuel cell stack. If the active area is identical for each fuel cell in the stack, the following relationship is true:

$$A_{stack} = n_c \cdot A_{cell} \quad \text{Equation (3-24)}$$

where  $A_{cell}$  is the active area of a single fuel cell and  $n_c$  is the number of fuel cells in a single stack. Substituting Equation (3-24) into Equation (3-23), redefines power as:

$$P_e = V \cdot n_c \cdot A_{cell} \cdot j \quad \text{Equation (3-25)}$$

However, an exact active cell area nor the exact number of fuel cells per stack is known. The number of electrons transferred for the electrochemical reaction, the cell voltage, and the consumption rate of the reactants is known. Thus, an expression for power that depends on pre-defined values or measurable variables is needed.

The electric current is defined in Faraday's law as,

$$i = \dot{q} \quad \text{Equation (3-26)}$$

where  $\dot{q}$  is the rate of charge transfer, which is directly related to the rate of the electrochemical reaction. Equation (3-27) expands on Equation (3-26) by using Faraday's constant to convert a charge in coulombs to a mol of electrons,

$$i = z \cdot F \cdot \dot{n} \quad \text{Equation (3-27)}$$

where current can now be expressed in terms of molar flow rate,  $\dot{n}$ . The current is related to the current density in the following manner:

$$i = n_c \cdot A_{cell} \cdot j \quad \text{Equation (3-28)}$$

Therefore, Equation 3-25 is redefined as Equation (3-29) below:

$$P_{gross} = V \cdot z \cdot F \cdot \dot{n} \quad \text{Equation (3-29)}$$

This expression was used to calculate the gross power generated by the fuel cell stack in the simulation. The variable,  $\dot{n}$ , is the molar rate of oxygen consumed in the fuel cell stack.

It should be noted that the power generated by the fuel cell system is in the form of DC electricity. The power calculated via Equation (3-29) represents the generation of DC power. The fuel cell system employs an inverter to convert the DC power into AC power. The electrical efficiency of the DC-AC converter,  $\varepsilon_{DC-AC}$ , is assumed to be 90 percent. There are also other parasitic loads associated with the fuel cell subsystems or balance-of-plant (BOP).

The mechanical balance-of-plant (mBOP) is a subsystem of the fuel cell system. It typically consists of fuel processing, pumps, compressors, blowers, and other equipment. The mBOP load,  $P_{mBOP}$ , was characterized by correlating empirical data for the mBOP load and gross AC power from the OCSD installation; it is shown below:

$$P_{mBOP} = -2.581 \exp(0.0078 \cdot P_e \cdot \varepsilon_{DC-AC}) \text{ [kW]} \quad \text{Equation (3-30)}$$

Other significant loads on the system power output are associated with the hydrogen separation unit. The pressure swing adsorption unit, two-stage compressors, and electric chillers loads are significant parasitic losses on the tri-generation system. An expression for the hydrogen separation unit load,  $P_{HSU}$ , was characterized by correlating empirical data for the HSU load and mass flow rate of hydrogen from the OCSD installation; it is depicted in Equation (3-31):

$$P_{HSU} = -\left\{17.732 \ln\left(H_2 \left[\frac{\text{lbs}}{\text{hr}}\right]\right) + 23.3\right\} \text{ [kW]} \quad \text{Equation (3-31)}$$

where  $H_2$  is the mass flow rate of hydrogen purified and exported from the system in lbs per hour.

The power available for export by the tri-generation system is represented as  $P_{net}$  in Equation (3-32):

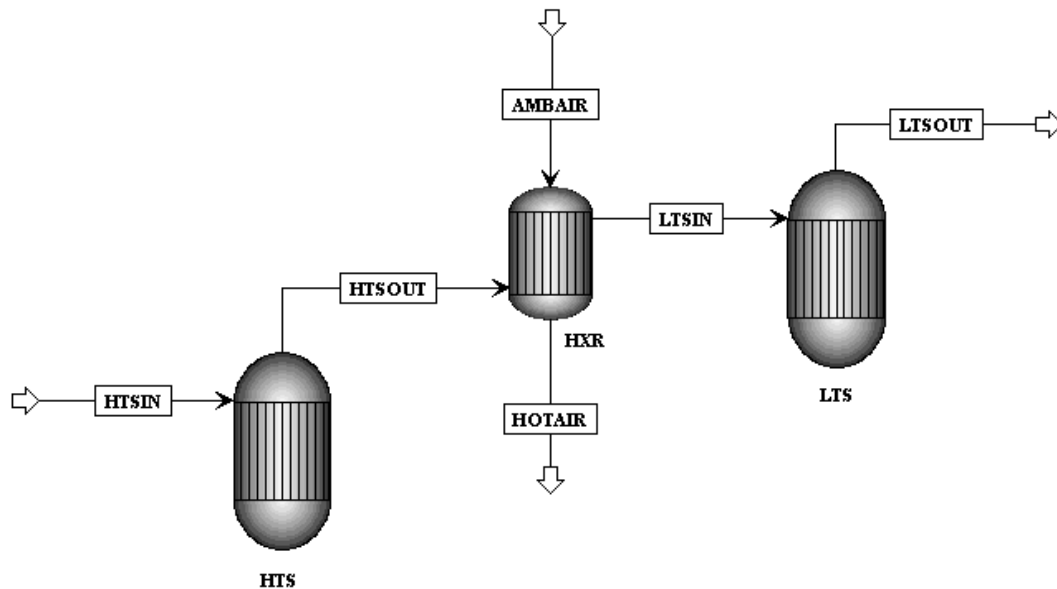
$$P_{net} = (P_e \cdot \varepsilon_{DC-AC}) + P_{mBOP} + P_{HSU} \quad [\text{kW}] \quad \text{Equation (3-32)}$$

which is takes into account the power conversion, mBOP, and HSU losses.

#### 4.3.2 Hydrogen Concentrator Unit (HCU)

The anode exhaust is rich in hydrogen and carbon monoxide. Promoting the water-gas shift reaction would increase the hydrogen concentration in the stream. The reaction rate at 350 °C achieves a practical hydrogen yield, although at lower temperatures (190—210 °C) the reaction favors the products further [36]. A hydrogen concentrator unit composed of high and low temperature water-gas shift reactors allowed for the greatest hydrogen yield. Since there is a significant temperature difference of 140—160 °C, a heat exchanger was necessary to remove heat from the high-temperature shift reactor exhaust. The oxidant that entered the fuel cell cathode demanded air at the fuel cell operating temperature. To optimize the system thermal management scheme, the same flow rate of air needed by the cathode was used to cool the shifted stream. The air entered at ambient conditions and left the heat exchanger at a much lower temperature than the fuel cell operating temperature, thus requiring more heating outside of the


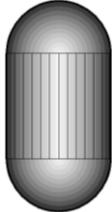

hydrogen concentrator before entering the cathode. The shifted stream was always cooled to the specified operating temperature (190 °C) of the low-temperature shift reactor. The low-temperature shift reactor exhaust was further cooled by the electric chiller. The process flow diagram of the modeled system is illustrated in Figure 12.



**Figure 12. Hydrogen concentrator unit modeled in Aspen Plus®**

The anode exhaust (HTSIN) entered the high-temperature shift reactor (HTS). The shifted stream (HTSOUT) was cooled in the air-cooled heat exchanger (HXR) by exchanging heat with ambient air (AMBAIR). The heated air (HOTAIR) exited the heat exchanger (HXR) and hydrogen concentrator unit for use by the fuel cell system. The cooled, shifted stream (LTSIN) was further shifted in the low-temperature shift reactor (LTS), resulting in a hydrogen-rich stream (LTSOUT). Table 10 below lists the assumptions and operating conditions for the process unit models integrated into the hydrogen concentrator unit model.

**Table 10. Aspen Plus® process unit models used to model the hydrogen concentrator unit**

<b>Unit Operation Model Name &amp; Type</b>	<b>Symbol</b>	<b>Assumptions</b>	<b>Operating Condition</b>
HTS <i>Equilibrium reactor</i>		<ol style="list-style-type: none"> <li>1.) Adiabatic</li> <li>2.) Chemical equilibrium reached for WGS reaction</li> <li>3.) Negligible pressure drop</li> <li>4.) Only WGS reaction occurs in reactor</li> </ol>	<ol style="list-style-type: none"> <li>1.) Heat Duty: 0 BTU/hr</li> <li>2.) <math>\Delta P=0</math> psia</li> </ol>
LTS <i>Equilibrium reactor</i>		<ol style="list-style-type: none"> <li>1.) Adiabatic</li> <li>2.) Chemical equilibrium reached for WGS reaction</li> <li>3.) Negligible pressure drop</li> <li>4.) Only WGS reaction occurs in reactor</li> </ol>	<ol style="list-style-type: none"> <li>1.) Heat Duty: 0 BTU/hr</li> <li>2.) <math>\Delta P=0</math> psia</li> </ol>
HXR <i>Heat Exchanger</i>		<ol style="list-style-type: none"> <li>1.) Countercurrent</li> <li>2.) Negligible pressure drop</li> </ol>	<ol style="list-style-type: none"> <li>1.) Hot stream outlet temperature: 190 °C</li> <li>2.) <math>\Delta P=0</math></li> </ol>

### 4.3.3 Hydrogen Separation Unit (HSU)

The gas exiting the hydrogen concentrator unit enters the hydrogen separation unit (HSU) at an incompatible temperature and pressure for the pressure swing adsorption system. The low-temperature shift outlet (LTSOUT) stream is at approximately 200 °C and must eventually be cooled to 10 °C and compressed from 17 psia to 150 psia before entering the pressure swing adsorption unit. Therefore, two electric chillers, a two-stage syngas compressor, and two knockout drums prepare the hydrogen-rich stream for purification in the PSA. The following process flow diagram in Figure 13 illustrates the hydrogen separation unit modeled:

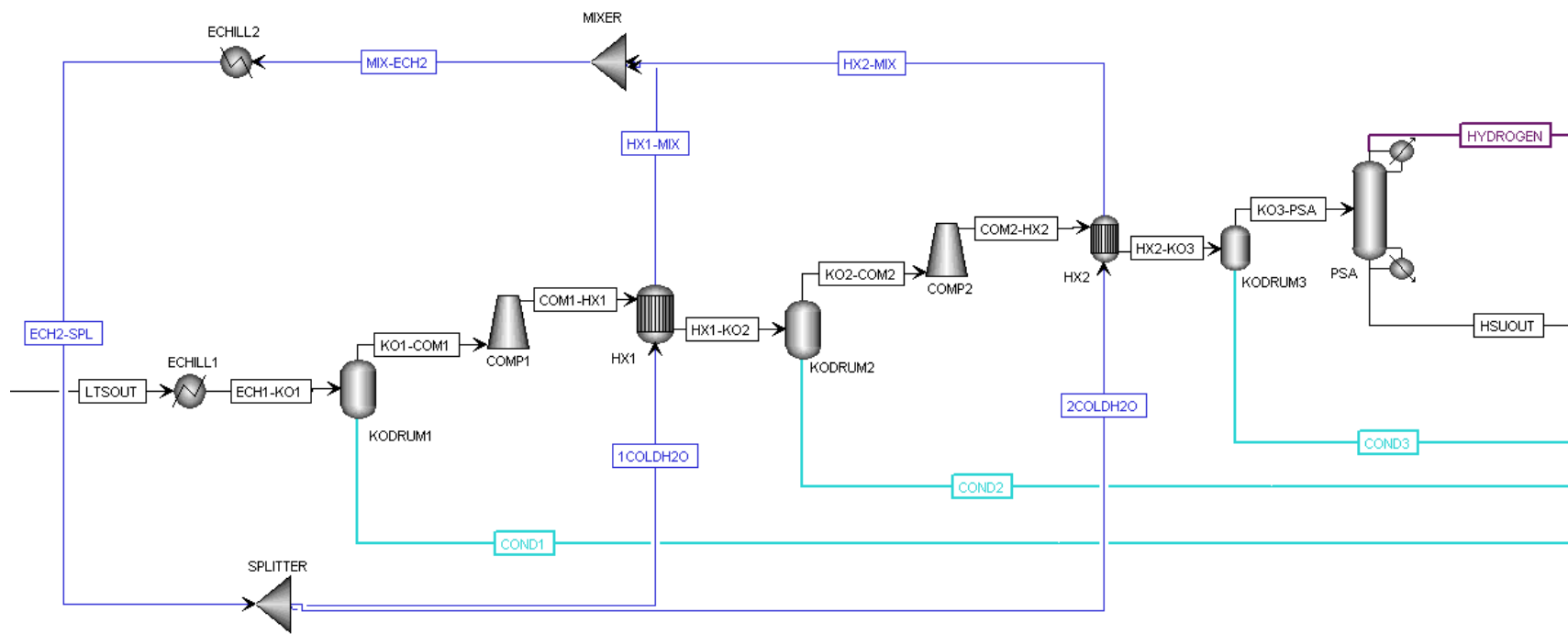


Figure 13. Aspen Plus® model of the hydrogen separation unit



### 4.3.3.1 Syngas Compressor

A two-stage syngas compressor was needed to increase the pressure of the stream exiting the low-temperature water-gas shift reactor from 2 psig to 150 psig before entering the PSA. Due to the heat created by compression, it is necessary to cool both the compression cylinders and the compressed gas. A cooling fan pushes air across the heads and cylinders, but it was not modeled due to its relevance to the entire system as a low-value excess heat stream. The inter-cooler and after-cooler are water-cooled and considered relevant to the system as it affected the PSA inlet stream. Chilled water at atmospheric pressure and 10 °C entered the inter-cooler at a rate of 112 lbmol/hr. The after-cooler received 168 lbmol/hr of water also at atmospheric pressure and 10 °C. The process flow diagram of the modeled system is illustrated in Figure 14.

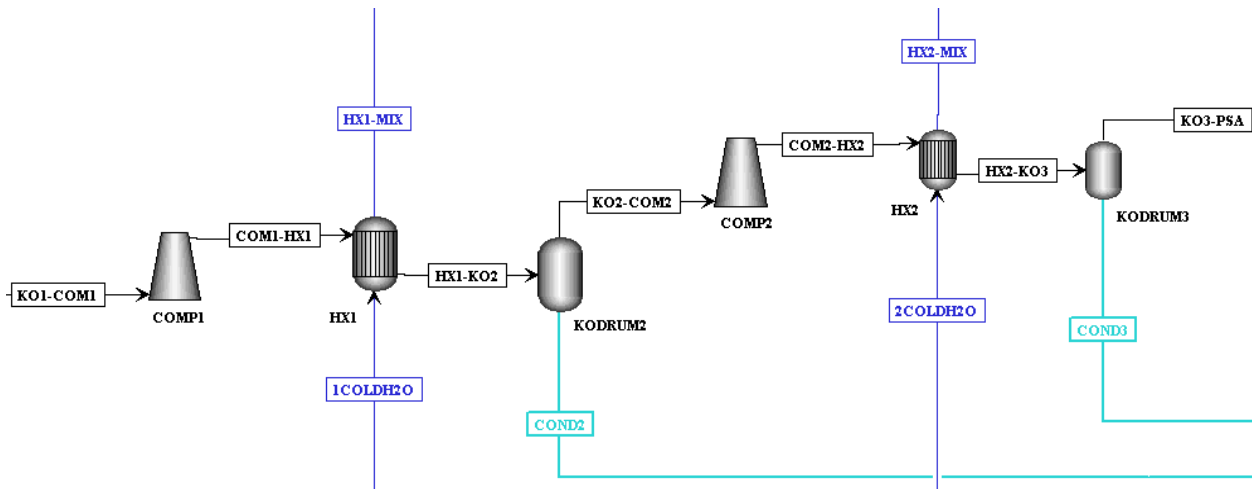
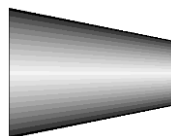
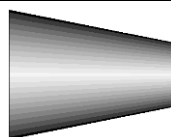



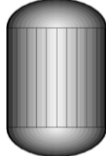


Figure 14. Two-stage compressor with water-cooling modeled in Aspen Plus®

The low-temperature water-gas shift reactor exhaust first entered a knockout drum (not shown) before entering the first compressor (COMP1) as KO1-COM1. The compressed stream

(COM1-HX1) left at the set COMP1 discharge pressure and at a higher temperature tolerable for the second compressor (COMP2). Chilled water (1COLDH20) exchanged heat with the hot compressed exhaust (COM1-HX1) in the inter-cooler (HX1). The heated cold stream (HX1-MIX) exited the inter-cooler (HX1) was later cooled with the use of an electric chiller. The cooled compressed exhaust (HX1-KO2) entered a knockout drum (KODRUM2) to remove condensed water. The drier compressed stream (KO2-COM2) enters the second compressor (COMP2). Chilled water (2COLDH20) exchanged heat with the hot compressed exhaust (COM2-HX2) in the after-cooler (HX2). The heated cold stream (HX2-MIX) exited the heat after-cooler (HX2) was later cooled with the use of an electric chiller. The cooled compressed exhaust (HX2-KO3) entered the next knockout drum (KODRUM3) to further remove condensed water before entering the PSA (not shown) as a high-pressure, low-moisture gas (KO3-PSA). The condensate from KODRUM2 (COND2) and KODRUM3 (COND3) enter the water cycle loop for the system. Table 12 below lists the assumptions and operating conditions for the process unit models discussed above.

**Table 11. Aspen Plus<sup>®</sup> process unit models used to model the two-stage syngas compressor.**

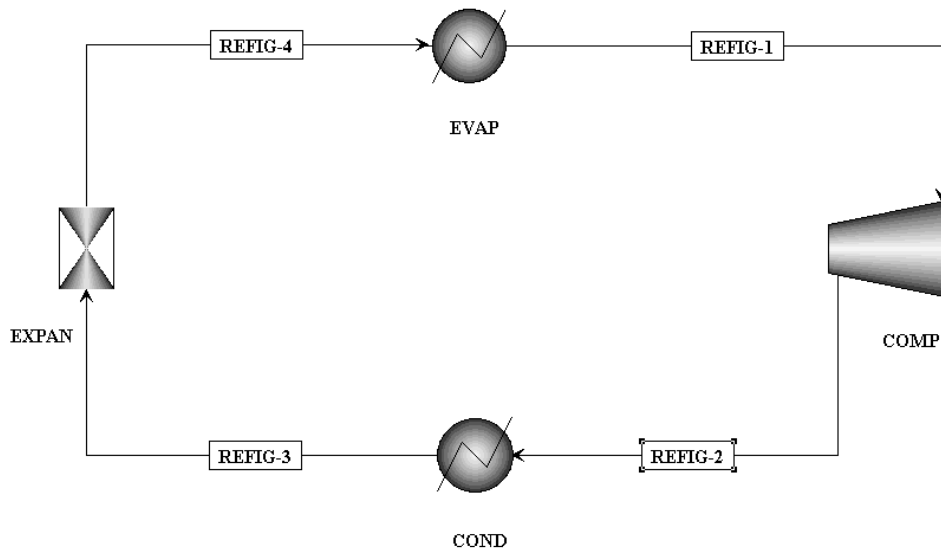
<b>Unit Operation Model Name &amp; Type</b>	<b>Symbol</b>	<b>Assumptions</b>	<b>Operating Condition</b>
COMP 1 <i>Compressor</i>		1.) Isoentropic compression and user-defined efficiency	1.) Efficiency: 72% 2.) Discharge Pressure: 35 psig
COMP 2 <i>Compressor</i>		1.) Isoentropic compression and user-defined efficiency	1.) Efficiency: 72% 2.) Discharge Pressure: 150 psig
KODRUM2 <i>Knock out drum</i>		1.) Adiabatic	1.) Heat Duty: 0 BTU/hr 2.) $\Delta P=0$ psia
KODRUM3 <i>Knock out drum</i>		1.) Adiabatic	1.) Heat Duty: 0 BTU/hr 2.) $\Delta P=0$ psia
HX1 <i>Heat Exchanger</i>		1.) Countercurrent 2.) Negligible pressure drop	1.) Hot stream outlet temperature: 21 °C 2.) $\Delta P=0$ psia
HX2 <i>Heat Exchanger</i>		1.) Countercurrent 2.) Negligible pressure drop	1.) Hot stream outlet temperature: 15 °C 2.) $\Delta P=0$ psia

#### 4.3.3.2 Electric Chillers

Two identical commercial electric chillers were incorporated into the model using the vapor-compression refrigeration cycle. One electric chiller cooled the gaseous stream entering the hydrogen separation unit suitable for the two stage compressor. The other chiller reduced the temperature of the water used for cooling the discharge gases from the two-stage syngas

compressor, which is further discussed in 4.3.3.1 Syngas Compressor. Each electrical chiller had a refrigeration capacity of 320,000 BTU/hr. The refrigerant 1,1,1,2-Tetrafluoroethane, commonly referred to as R-134a, flowed through the refrigeration circuit at 22 lbmol/hr.

Electric chillers operate on the vapor-compression refrigeration cycle, where an electrically driven compressor powered the cycle. The vapor-compression refrigeration cycle modeled in Aspen Plus is shown below in Figure 15:

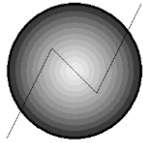
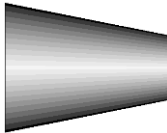
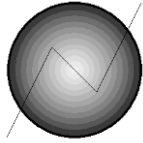
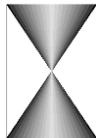


**Figure 15. Electric chiller refrigeration cycle modeled in Aspen Plus®**

The refrigerant cycled through four units represented in Figure 15: evaporator (EVAP), compressor (COMP), condenser (COND), and expansion valve (EXPAN). The refrigerant liquid (REFIG-4) was first evaporated at reduced pressure by absorbing heat from the cooling load stream, which in the model is the low-temperature shift outlet (LTSOUT) stream in Figure 13. A compressor then increased the pressure of the refrigerant vapor (REFIG-1) to the desired

condenser pressure. The compressed refrigerant vapor (REFIG-2) was condensed through the transfer of heat to a medium temperature environment. The model assumes the surrounding environment acted as a heat sink for the condensation of the refrigerant. Lastly, the pressure of the refrigerant (REFIG-3) was reduced to the evaporator pressure after the cooling fluids passed through an expansion valve. The reduced-pressure refrigerant (REFIG-4) entered the evaporator and continued the described vapor-compression refrigeration cycle. Table 12 below lists the assumptions and operating conditions for the process unit models discussed above.

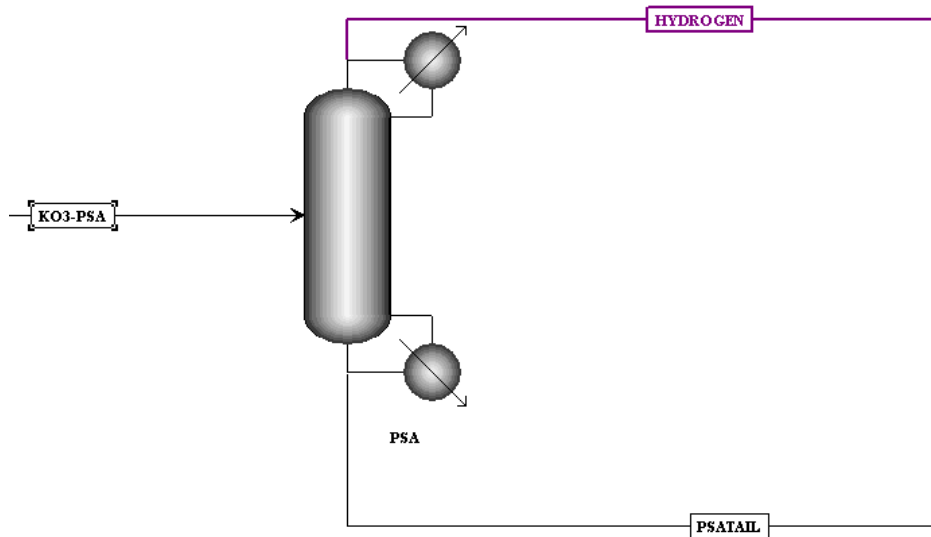
**Table 12 Aspen Plus<sup>®</sup> process unit models used to model the electric chillers**

<b>Unit Operation Model Name &amp; Type</b>	<b>Symbol</b>	<b>Assumptions</b>	<b>Operating Condition</b>
EVAP <i>Heater</i>		1.) Electrical chiller operating at full load 2.) Pressure drop negligible	1.) Heat duty: 320,000 BTU/hr 2.) $\Delta P=0$ psia
COMP <i>Compressor</i>		1.) Isoentropic compression and user-defined efficiency	1.) Efficiency: 72% 2.) Discharge Pressure 85 psig
COND <i>Condenser</i>		1.) Exiting stream only in liquid phase 2.) Pressure drop negligible	1.) Vapor fraction: 0 2.) $\Delta P=0$ psia
EXPAN <i>Expansion valve</i>		1.) Adiabatic flash at the valve outlet pressure	1.) Outlet Pressure: 7 psig

#### 4.3.3.3 Pressure Swing Adsorption (PSA) System

For vehicle fueling, the hydrogen stream must be at least 99.97 % pure with less than 0.1 ppm of carbon monoxide to avoid adversely affecting the PEMFC used in a fuel cell electric vehicle [53]. A pressure swing adsorption unit is used to separate molecular hydrogen from the syngas mixture. The syngas entering the PSA was composed largely of hydrogen, carbon dioxide, water, carbon monoxide and nitrogen, with less than 1 volume percent of oxygen and methane. Simulating all of the chemical and physical processes of a PSA would have required complex modeling that would not have significantly fulfilled the goal of this research to assess the system performance of a tri-generating fuel cell plant. The PSA was simplified into a separation process with overall operating and performance characteristics expected of current PSA technology, verified by comparison to the performance observed in the field.

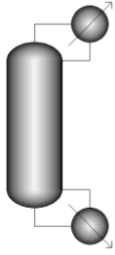
The feed to the pressure swing adsorption unit entered at 150 psig and 15 °C [54] following compression, cooling, and condensation. The tail gas from the PSA (CO<sub>2</sub>, H<sub>2</sub>O, and unconverted methane) was recycled to the fuel cell cathode. The hydrogen product was exported to the fueling station after it was compressed further. Both streams exited the PSA at 140 psig. The modeled pressure swing adsorption unit is shown below as Figure 16.



**Figure 16. Pressure swing adsorption system modeled in Aspen Plus®**

High-pressure, low-moisture, cool feed (KO3-PSA) entered the separator (PSA) after condensation (not shown in Figure 16). Pure hydrogen product (HYDROGEN) exited the PSA for export. The hydrogen-depleted stream (PSATAIL) exited from the PSA and was recycled to the fuel cell system. Table 13 below lists the assumptions and operating conditions for the process unit model discussed above.

**Table 13. Aspen Plus® process unit models used to simulate the PSA unit**

Unit Operation Model Name & Type	Symbol	Assumptions	Operating Condition
PSA Separator		<ol style="list-style-type: none"> <li>1.) PSA hydrogen recovery is 85 % [54]</li> <li>2.) PSA produces hydrogen at 100 % purity</li> <li>3.) PSA pressure drop is 10 psia [26]</li> </ol>	<ol style="list-style-type: none"> <li>1.) Fraction of H<sub>2</sub> in the feed going to outlet stream: 0.85</li> <li>2.) ΔP=10 psia</li> <li>3.) Outlet temperature: 15 °C</li> </ol>

#### 4.4 Efficiency of Tri-Generating High-Temperature Fuel Cell

The efficiency for the HTFC tri-generation system can be evaluated on an overall and/or a single co-product basis. The overall efficiency is defined as a combined hydrogen and power generation efficiency and is expressed as  $\eta_{CH2P}$  in Equation (3-33),

$$\eta_{CH2P} = \frac{P_{net} + H}{E_{tot}} \quad \text{Equation (3-33)}$$

where  $P_{NET}$  is the net power generated (kWh),  $H$  is the hydrogen produced (kWh based on LHV), and  $E_{TOT}$  is energy of the input fuel (kWh based on LHV). The inputs and outputs of the system are known and the overall efficiency is simple to calculate. The portion of input fuel associated with a particular co-product is difficult to quantify. Margalef et al. [55] established three methodologies to express hydrogen, electrical, and thermal efficiency, but the supplemental inputs method will be discussed below. The Supplemental Inputs Method defines the hydrogen production efficiency,  $\eta_{H2}$ , in Equation (3-34),



$$\eta_{H2} = \frac{H}{(U_F - U_{F,H2ES})E_{tot} + \frac{P_{PSA}}{\eta_{CC}}} \quad \text{Equation (3-34)}$$

where, the  $U_F$  is the normal fuel utilization factor of a typical co-generating HTFC (assumed to be 90 %),  $U_{F,H2ES}$  is the fuel utilization factor for a tri-generating HTFC,  $P_{psa}$  is the power consumed to separate the hydrogen, and  $\eta_{cc}$  is the combined cycle efficiency (assumed to be 60 %). The difference of the utilization factors multiplied by  $E_{TOT}$ ,  $(U_F - U_{F,H2ES}) E_{TOT}$ , corresponds to the additional fuel necessary for hydrogen production. The ratio of  $P_{psa}$  to  $\eta_{cc}$  represents the actual power necessary for the hydrogen separation unit based on a state-of-the-art combined cycle efficiency. The  $\eta_{cc}$  was chosen as a means to compare conventional to tri-generation hydrogen production.

The electrical efficiency,  $\eta_{electrical}$ , is expressed by Equation (3-35):

$$\eta_{electrical} = \frac{P_{net}}{E_{tot} - \left( (U_F - U_{F,H2ES})E_{tot} + \frac{P_{PSA}}{\eta_{CC}} \right)} \quad \text{Equation (3-35)}$$

## Chapter 5:      **Model Verification**

In order for the tri-generation model to be verified, simulated tri-generation operation on natural gas and anaerobic digester gas must match real system data. The molten carbonate fuel cell system, the largest and most significant system component of the model, must be proven accurate at typical operating conditions where hydrogen is not separated and exported, which has been termed as “normal operation.” This is the first step to verifying the model because previously published research on a tri-generation system using a DFC<sup>®</sup> molten carbonate fuel cell system does not exist for comparison. Thus, it was assumed that verifying the performance of the modeled DFC<sup>®</sup> in “normal operation” would also confirm that the modeled fuel cell contained sufficient performance characteristics that would hold true in “tri-generation mode.” Consequently, results pertaining to the fuel cell performance in “tri-generation mode” would warrant discussions unburdened by the question of accurate fuel cell construction. The following sections will prove and discuss:

- DFC<sup>®</sup> fuel cell system construction, including
  - Fuel cell stack simplification
  - Anode discretization
- Stream compositions
  - Anode exhaust
  - Cathode feed
  - Cathode exhaust

- High-temperature shift exhaust
- Low-temperature shift exhaust
- Voltage
- Power generation
- Parasitic losses

## 5.1 Verification of FuelCell Energy Direct FuelCell® Model

The intention of this study was to accurately model a tri-generation system with a molten carbonate fuel cell that performs like a FuelCell Energy 300 kW Direct FuelCell®. The molten carbonate fuel cell modeled in Aspen Plus® was detailed in 4.3.1 Molten Carbonate Fuel Cell. The internal reforming molten carbonate fuel cell stack was uniquely constructed by simplifying the stack into a single direct internal reforming fuel cell and discretizing the anode. The stack simplification and discretization methodology was described in 4.3.1.4 Simplified Fuel Cell Stack Model and 4.3.1.8 Anode Discretization respectively. To verify the constructed molten carbonate fuel cell stack simplification and discretization strategy, the results from this study had to be compared to the research conducted by Lukas et al. [40].

A thermodynamic model for an internal reforming molten carbonate fuel cell power plant was discussed in “Modeling and Cycling Control of Carbonate Fuel Cell Power Plants” by Lukas et al.[40]. The dynamic model was based on physical data obtained from a 2 MW DFC® designed and manufactured by FuelCell Energy. Thermal and chemical time-dependent

processes for the fuel cell stack, heat recovery, fuel processing, and power generation were numerically computed in the lumped-parameter model. Reforming reaction kinetics, mass storage, and cell polarization losses were also applied to the fuel cell characterization.

The verification of the internal reforming molten carbonate fuel cell stack built in the likeness of a DFC<sup>®</sup> depended on replicating the results from the work of Lukas et al [40]. The tri-generation model was first simplified by excluding the hydrogen concentrator and hydrogen separation unit, as the inlet and outlet cathode stream composition would otherwise not be congruent with “normal operation” performance. This remedy would not compromise the actual characterization and performance of the fuel cell system in “tri-generation mode” as the discrepancy associated with the incoming and outgoing cathode was only attributed to the processes increasing hydrogen concentration and removing hydrogen from the fuel cell system. Thus, internal reforming molten carbonate fuel cell stack will be verified using the aforementioned model simplification.

The following operating conditions from Lukas et al. [40] were applied to the simplified fuel cell model demonstrating “normal operation” of a DFC<sup>®</sup> unit:

- Fuel utilization factor
- Fuel cell stack temperature
- Fuel cell stack pressure
- Natural gas, steam, and air flow rate

The values for the fuel utilization factor, fuel cell stack temperature and pressure specified by Lukas et al. [40] are listed in Table 14 below.

**Table 14. Operating properties for DFC<sup>®</sup> verification**

Parameter	Symbol	Description	Operating Condition
Fuel Utilization Factor	$U_F$	Fraction of hydrogen consumed electrochemically in fuel cell to the amount of hydrogen available to react	0.75
Fuel Cell Stack Temperature	$T_s$	Average temperature of fuel cell stack	676.7 °C
Fuel Cell Stack Pressure	$P_s$	Operating pressure inside stack	17 psia

Table 15 lists the stream conditions for the fuel, air, and water entering the fuel cell system in the model constructed by Lukas et al. [40].

**Table 15. Input stream conditions for DFC<sup>®</sup> verification**

Stream	Flow Rate	Pressure	Temperature
Fuel	2361.6 lbmol/hr	15 psia	700 F
Air	35293.8 lbmol/hr	15 psia	91 F
Water	4176.2 lbmol/hr	15 psia	211 F

The fuel used was natural gas, which was composed purely of methane. The air composition was assumed to be only composed of oxygen and nitrogen. Also, the water entering the fuel cell

system was free of impurities. The fuel, air, and steam stream composition is summarized in Table 16 below.

**Table 16. Input stream composition for verification of DCF<sup>®</sup> model**

<b>Stream</b>	<b>O<sub>2</sub></b> vol%	<b>N<sub>2</sub></b> vol%	<b>H<sub>2</sub></b> vol%	<b>CO</b> vol%	<b>CO<sub>2</sub></b> vol%	<b>CH<sub>4</sub></b> vol%	<b>H<sub>2</sub>O</b> vol%
Fuel	0	0	0	0	0	100	0
Air	21	79	0	0	0	0	0
Water	0	0	0	0	0	0	100

Lukas et al. [40] predicted the anode and cathode exhaust composition of the internal reforming molten carbonate fuel cell at operating conditions specified in Table 14, Table 15, and Table 16. These data will be used to verify both the fuel cell stack simplification and the anode discretization. First, the anode discretization will be proven by comparing the anode and cathode exhaust composition of a single-stage anode and a seven-stage anode (the basis of the fuel cell model studied in this work and justified in 4.3.1.8 Anode Discretization) to the values predicted by Lukas et al. [40]. Then, the magnitude of the percent error associated with the modeled anode and cathode exhaust composition of the seven-stage anode will determine the accuracy of the fuel cell system integrated into the tri-generation model.

The actual composition, the modeled anode exhaust composition for the single-stage and seven-stage anode simulation, and the percent error linked to the modeled results are listed in Table 17 below.

**Table 17. Measured and modeled stream compositions for anode exhaust**

Species	Measured (vol %)	Single-stage (vol %)	Seven-stage (vol %)	Single-stage (% error)	Seven-stage (% error)
H <sub>2</sub>	7.85	9.39	7.85	19.6	0.05
CO	4.89	5.66	4.87	15.9	0.47
CO <sub>2</sub>	45.63	44.22	46.05	3.08	0.91
H <sub>2</sub> O	42.30	40.72	41.24	3.73	2.5
N <sub>2</sub>	<<0.001	---	---	---	---
CH <sub>4</sub>	<0.002	---	---	---	----

The results reveal that not only does the seven-stage anode predict the anode composition more accurately than the single-stage anode, but the prediction for each component is close to the true value. Thus, discretization was determined to be a vital addition to the modeling effort as it better captured the simultaneous chemical and electrochemical reactions and physical processes occurring in the anode. An error less than 5 percent for each component suggests that the seven-staged anode predicts the anode exhaust composition of a DFC<sup>®</sup> fuel cell reasonably well.

Although the anode was discretized, the cathode model was left as a single stage reactor for reasons justified in section 4.3.1.8 Anode Discretization. The cathode exhaust composition is still evaluated since any steam composition improvements in the anode compartment positively affects the accuracy of the cathode exhaust composition. Table 18 below lists the resulting cathode exhaust composition for the single-stage and seven-stage anode model, the measured composition, and the percent error linked to the modeled results.

**Table 18. Measured and modeled stream compositions for cathode exhaust**

Species	Measured (vol %)	Single-stage (vol %)	Seven-stage (vol %)	Single-stage (% error)	Seven-stage (% error)
H <sub>2</sub>	<<0.001	---	---	---	---
CO	<<0.001	---	---	---	---
CO <sub>2</sub>	5.657	4.903	5.589	13.3	2.7
H <sub>2</sub> O	22.12	21.53	21.90	2.66	0.99
N <sub>2</sub>	66.40	67.46	65.79	1.60	0.91
O <sub>2</sub>	6.997	6.099	6.896	12.8	1.4

The results for the cathode exhaust comparison reaffirms that the seven-stage anode better represents measured performance than the single-stage anode model. An error less than 5 percent for each component suggests that the seven-staged anode model allows for more accurate prediction of the cathode exhaust composition of a DFC<sup>®</sup> fuel cell.

Simplifying the fuel cell stack into a single fuel cell with direct internal reforming capability is valid due to the reasonable agreement between measured and modeled exhaust compositions for both the anode and cathode. It also suggests that the pre-reformer and indirect internal reformation model were captured well and contributed the overall accuracy seen with the fuel cell exhaust compositions. The anode discretization methodology led to results much more comparable to FuelCell Energy data for a fuel cell operating normally than a single-stage model. The results suggest that discretizing the anode simulates the progression of reactions across the cell accurately and single-stage fuel cell models should be discretized. This is especially necessary/true for fuel cells stacks with direct internal reforming. Consequently, the fuel cell stack simplification and anode discretization methodologies are valid and should correctly predict the FuelCell Energy 300 kW DFC<sup>®</sup> in “tri-generation mode.”



## **5.2 Verification of Tri-generating FuelCell Energy Direct FuelCell®**

The hydrogen energy station at Orange County Sanitation District presented a valuable opportunity to collect data for the verification of the tri-generation model discussed in Chapter 4: Model Development. The following sections describe the verification of the tri-generation model operating on two different fuels: natural gas and anaerobic digesters gas. The operating conditions, assumptions, and results for each case will be discussed in the following sections.

### **5.2.1 Verification of Tri-generating Direct FuelCell® using Natural Gas**

The steady-state operating conditions for the tri-generation system fueled by natural gas are listed in Table 19.

**Table 19. Model operating conditions for tri-generation fuel cell using natural gas**

Parameter	Symbol	Description	Operating Condition
Fuel Utilization Factor	$U_F$	Fraction of hydrogen consumed electrochemically in fuel cell to the amount of hydrogen available to react	0.65
Current Density	$j$	Quantity of electric current flowing per unit cross-sectional area	1200 A / m <sup>2</sup>
Steam-to-Carbon Ratio	S/C	Molar. ratio of water to atomic carbon	2
Fuel Cell Stack Temperature	$T_s$	Average temperature of fuel cell stack	676.7°C
Fuel Cell Stack Pressure	$P_s$	Operating pressure inside stack	16 psia
PSA pressure	$P_{PSA}$	Operating pressure of PSA	150 psia
PSA inlet temperature	$T_{PSA}$	Operating temperature of PSA	15 °C

The fuel utilization, current density, and steam-to-carbon ratio was data obtained for the existing tri-generation fuel cell system operating at OCSD. The fuel cell stack temperature and pressure were not available for the existing tri-generation fuel cell system, so it was assumed to be the same as the verified fuel cell model in “normal operation” from 5.1 Verification of FuelCell Energy Direct FuelCell® Model. The PSA temperature and pressure values were explained in 4.3.3.3 Pressure Swing Adsorption (PSA) System.

Table 20 lists the stream conditions for the fuel, air, and water entering the tri-generating fuel cell system.

**Table 20. Input stream conditions for tri-generation fuel cell using natural gas**

Stream	Flow Rate	Pressure	Temperature
Fuel	5.44 lbmol/hr	46 psia	94 °F
Air	61.6 lbmol/hr	15 psia	91 °F
Water	10.9 lbmol/hr	15 psia	211 °F

The fuel used was natural gas, which was composed mostly of methane with a fraction of ethane (C<sub>2</sub>H<sub>6</sub>) and propane (C<sub>3</sub>H<sub>8</sub>). The air composition was composed of oxygen and nitrogen, but also contained moisture. Also, the water entering the fuel cell system was free of impurities. The fuel, air, and water stream composition is summarized in Table 21 below.

**Table 21. Input stream composition for verification of tri-generating DCF<sup>®</sup> model operating on natural gas**

Stream	O <sub>2</sub> vol%	N <sub>2</sub> vol%	H <sub>2</sub> vol%	CO vol%	CO <sub>2</sub> vol%	CH <sub>4</sub> vol%	C <sub>2</sub> H <sub>6</sub> vol%	C <sub>3</sub> H <sub>8</sub> vol%	H <sub>2</sub> O vol%
Fuel	0	0.308	0	0	1.28	96.1	1.94	0.372	0
Air	78.3	20.7	1.01	0	0	0	0	0	0
Water	0	0	0	0	0	0	0	0	100

The measured stream compositions were determined through gas chromatography performed by FuelCell Energy. The stream must be dry as possible for the gas to be analyzed. Therefore, the percent by volume of water is not available for most stream composition comparisons. The measured anode exhaust composition, modeled composition, and percent error for the tri-generation simulation are listed in Table 22 below.

**Table 22 Measured and modeled anode exhaust composition for natural gas case**

<b>Species</b>	<b>Measured (vol%)</b>	<b>Model (vol%)</b>	<b>Percent Error</b>
<b>H<sub>2</sub></b>	20.12	20.09	0.15
<b>CO<sub>2</sub></b>	70.46	68.64	2.58
<b>CO</b>	8.49	11.19	31.8

The concentration of methane and nitrogen are negligible at the exit of the anode. The amount of hydrogen in the modeled anode exhaust was slightly lower than the measured volume percent. The amount of carbon dioxide modeled was lower than the measured value, whereas the concentration of carbon monoxide in the modeled exhaust was lower in the than measured quantity. These results indicate that more of the carbon monoxide was shifted inside the measured fuel cell than the modeled fuel cell. The opposite was true for the fuel cell model evaluated in 5.1 Verification of FuelCell Energy Direct FuelCell® Model. The modeled anode stream contained slightly more carbon dioxide and marginally less carbon monoxide. It may be conjectured that modeled fuel cell stack temperature may be too high relative to the actual temperature of the anode compartment at its exit. The water-gas shift reaction favors the reactants, water and carbon dioxide, at high temperatures. The composition of the anode exhaust would be affected by the water-gas shift reaction even if the modeled anode operated merely 20 ° C higher than the measured temperature. Also, the percent error for the carbon monoxide seems large, but is actually acceptable. The molar flow rate of carbon monoxide in the anode exhaust is relatively small compared to water, hydrogen, and carbon dioxide. Therefore, a change in the quantity of carbon monoxide greatly impacts the mole fraction of the component in the stream compared to the same change in quantity for water, hydrogen, and carbon dioxide.

The sample exhaust had to be cooled down in order and stripped of water vapor and condensed water before it was analyzed for it to be analyzed. Although water made up a significant percentage of the anode exhaust, it was physically removed from the anode exhaust sample to avoid interfering with the gas chromatography analysis. It could be conjectured that the removal of water from the measured anode exhaust may have also removed some carbon dioxide, which lowered the concentration of carbon dioxide in the sample stream. The lower temperature may have also shifted the sample slightly. Either scenario could have contributed to a small change in quantity of carbon dioxide that affected the measured mole fraction more sizably. Both the percent error and mole fraction of the modeled carbon monoxide compared to carbon dioxide differs by one magnitude.

The measured high-temperature shift reactor exhaust composition, modeled composition, and percent error for the tri-generation simulation are listed in Table 23 below.

**Table 23. Composition of measured and modeled HTS reactor exhaust**

<b>Species</b>	<b>Measured (vol%)</b>	<b>Model (vol%)</b>	<b>Percent Error</b>
<b>H<sub>2</sub></b>	<b>24.90</b>	<b>26.62</b>	<b>8.12%</b>
<b>CO<sub>2</sub></b>	<b>72.69</b>	<b>71.33</b>	<b>1.88%</b>
<b>CO</b>	<b>1.71</b>	<b>1.68</b>	<b>1.55%</b>

The amount of hydrogen in the modeled HTS exhaust was much higher than the measured volume percent. That may be due to the ideal performance of the modeled reactor versus a real water-gas shift reactor and catalyst. The amount of carbon dioxide and carbon

monoxide modeled were lower than the measured value. Carbon dioxide volume and error percentage did not change significantly from the anode exhaust results since it is a major component of the moisture-free high-temperature shift and anode exhaust. The carbon monoxide percent error changed was significantly closer to the true value compared to the modeled anode exhaust. That may have occurred because carbon monoxide in the stream shifted at a temperature that may be comparable to the same temperature the measured samples were taken.

Only the water-gas shift reaction was specified to occur in the HTS reactor. Therefore, the consumption and generation of the species was solely based on water-gas shift stoichiometry and equilibrium constant at the reactor temperature. It is helpful to look at the molar flow rate of the modeled inlet and outlet stream composition for the high-temperature shift reactor to better understand the results seen in Table 23. For that reason, the molar flow rate of hydrogen, steam, carbon monoxide, and carbon dioxide entering and exiting the HTS reactor, as well as the percent converted of each species is listed in Table 24.

**Table 24. Modeled inlet and outlet HTS molar flow rate of species**

<b>Species</b>	<b>Inlet (lbmol/hr)</b>	<b>Outlet (lbmol/hr)</b>	<b>Production (%)</b>
<b>H<sub>2</sub></b>	<b>4.95</b>	<b>6.93</b>	<b>39.9</b>
<b>CO<sub>2</sub></b>	<b>16.9</b>	<b>18.9</b>	<b>11.7</b>
<b>CO</b>	<b>2.76</b>	<b>0.784</b>	<b>-71.6</b>
<b>H<sub>2</sub>O</b>	<b>16.9</b>	<b>14.9</b>	<b>-14.2</b>

The modeled reactor converted 71.6 % of the carbon monoxide in the high-temperature inlet stream (also known as the anode exhaust stream), whereas the real reactor may not convert as much carbon monoxide. Although the amount of carbon dioxide increased 11.7 %, the mole fraction of carbon dioxide only increased by 2.69 percent between the inlet and outlet of the HTS reactor based on the values listed in Table 22 and Table 23. That result is expected due to the large concentration of carbon dioxide in the high-temperature shift outlet stream. It can also be seen that steam is the next largest constituent of the HTS outlet stream, which indicates that extensive drying was needed before running the exhaust through the gas chromatograph. Therefore, the percent errors between the modeled and measured species concentration may differ due to errors introduced by the analytical chemistry methodology and instrument.

The measured low-temperature shift reactor exhaust composition, modeled composition, and percent error for the tri-generation simulation are listed in Table 25 below.

**Table 25. Measured and modeled exhaust composition of LTS reactor**

<b>Species</b>	<b>Measured (vol%)</b>	<b>Model (vol%)</b>	<b>Percent Error</b>
<b>H<sub>2</sub></b>	<b>24.8</b>	<b>27.9</b>	<b>12.8</b>
<b>CO<sub>2</sub></b>	<b>73.4</b>	<b>71.7</b>	<b>2.26</b>
<b>CO</b>	<b>1.08</b>	<b>0.229</b>	<b>79.4</b>

The amount of hydrogen in the modeled LTS exhaust was much higher than the measured volume percent because much more hydrogen was produced in the modeled HTS reactor upstream. The other reason may be due to the sub-par performance of the measured low-

temperature shift reactor. The fraction of carbon dioxide in the modeled LTS outlet stream was lower than the measured value, which is a result of the overly high hydrogen yield predicted by the model. The mole fraction of carbon dioxide only increased 0.37 between the inlet and outlet of the LTS reactor based on the values listed in Table 23 and Table 25. The 3 percent increase in hydrogen concentration also indicates that a large amount of carbon monoxide was shifted. As a matter of fact, the volume percent of carbon monoxide on a dry basis decreased by 1.451 in the low-temperature shift reactor. The carbon monoxide volume percent is significantly erroneous. It may be that high for the same reason stated for the anode exhaust error. A change in the quantity of carbon monoxide affects the percent error considerably compared to other species in the stream. Again, it is best to evaluate the molar flow rate of the modeled inlet and outlet stream composition for the low-temperature shift reactor to better understand the results seen in Table 25. For that reason, the molar flow rate of hydrogen, steam, carbon monoxide, and carbon dioxide entering and exiting the LTS reactor, as well as the percent converted of each species is listed in Table 26.

**Table 26. Modeled inlet and outlet LTS molar flow rate of species**

<b>Species</b>	<b>Inlet (lbmol/hr)</b>	<b>Outlet (lbmol/hr)</b>	<b>Conversion (%)</b>
<b>H<sub>2</sub></b>	<b>6.93</b>	<b>7.64</b>	<b>10.3</b>
<b>CO<sub>2</sub></b>	<b>18.9</b>	<b>19.6</b>	<b>3.78</b>
<b>CO</b>	<b>0.784</b>	<b>0.070</b>	<b>91.1</b>
<b>H<sub>2</sub>O</b>	<b>14.9</b>	<b>14.1</b>	<b>4.80</b>



The modeled reactor converted 91.1 % of the carbon monoxide in the low-temperature shift inlet stream, whereas the real reactor did not convert as much carbon monoxide. The conversion of carbon monoxide is reasonable and LTS reactors have been modeled with 90 % CO conversion [36]. The amount of carbon dioxide only increased 3.78 % between the inlet and outlet of the LTS reactor. The low-temperature shift stream still retained a high percentage of steam, with only 4.8 percent converted. Much of that moisture needed to be condensed out before entering the two-stage syngas compressor. The low-moisture stream then was mostly composed of hydrogen and carbon dioxide before entering the PSA. A portion of the hydrogen was removed for use as a transportation fuel through pressure swing adsorption processes. The CO<sub>2</sub>-rich PSA tail gas entered an oxidizer with pre-heated air. Any remaining hydrocarbons and hydrogen were burned in the oxidizer. The exiting stream was used as the oxidant for the cathode.

The measured molar flow rate of oxygen, steam, nitrogen, and carbon dioxide exiting the cathode is known and compared to the modeled stream. The composition for these streams as well as the percent error of each species is listed in Table 27.

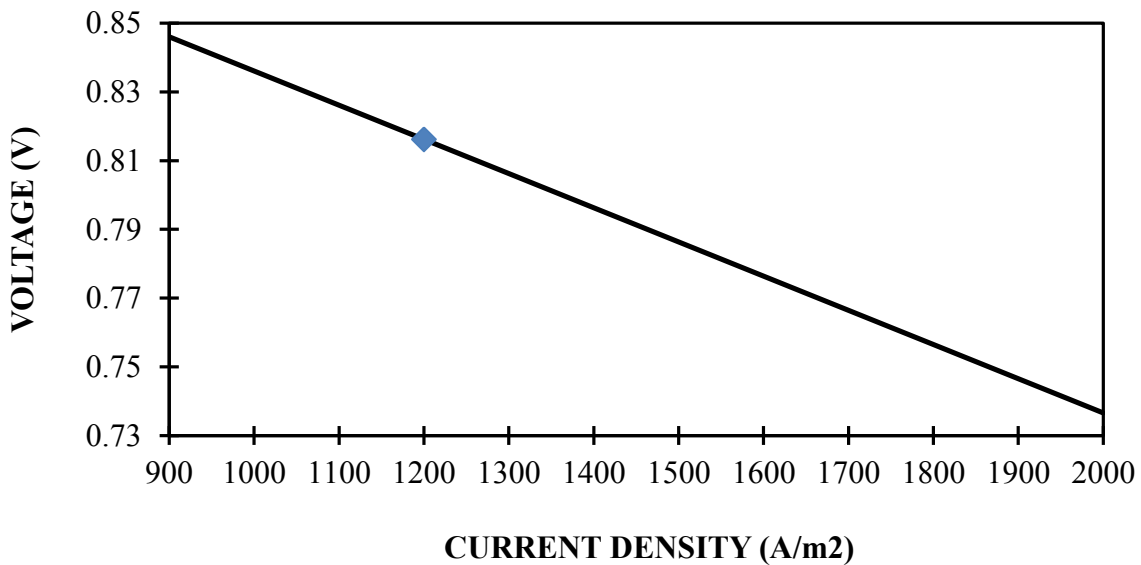
**Table 27. Measured and modeled cathode exhaust molar flow rate and percent error**

<b>Species</b>	<b>Measured (lbmol/hr)</b>	<b>Model (lbmol/hr)</b>	<b>Percent Error</b>
O <sub>2</sub>	3.67	3.71	1.28
CO <sub>2</sub>	5.60	5.30	5.35
H <sub>2</sub> O	4.89	4.61	5.69
N <sub>2</sub>	48.24	48.25	0.01

The amount of carbon dioxide exiting the modeled cathode is lower than the measured molar flow rate. That is expected since the concentration of carbon dioxide for the modeled tri-generation system was consistently lower than the recorded value. The error was expected to carry over and increase downstream. Although the percent error for the flow rate of carbon dioxide with respect to the measured value is 5.35 %, the modeled value is still a reasonable prediction. The error for the steam flow rate cannot be tracked as the other species, since the other measured stream compositions were analyzed on a dry basis. However, based on the stoichiometry of the electrochemical reaction at the anode, it is expected that the difference between the measured and modeled steam flow rate is almost equivalent to the difference between the measured and modeled carbon dioxide flow rate. There is a slight difference between the measured and modeled rate of oxygen and nitrogen, which may be due to experimental error and is not significant enough to warrant serious consideration.

The voltage for the modeled MCFC tri-generation system was determined by the approach defined in 4.3.1.10 Voltage. The cathode polarization equation listed in 4.3.1.10 had to be first modified to fit the known data for the system based on the assumptions and reasoning presented in the same section. A multiplier or “fudge factor” was suggested as a manner to modify the cathode resistance. The calculated voltage was compared to the measured average voltage of the DFC<sup>®</sup> fuel cell at known operating conditions. The cathode resistance was then multiplied by a factor that would in turn match the modeled voltage to the empirical value. Since the modeled voltage was higher than the measured voltage, the cathode resistance was multiplied by a factor of 2.99 to increase the irreversible losses in the fuel cell and account for the contact resistance, bipolar plate resistance, and other resistive losses in the complete full-scale fuel cell

stack. It was anticipated in 4.3.1.10 Voltage that the modeled cathode resistance would need to be increased, in particular, due to the effect of the assumed electrolyte composition on the cathode performance. The predicted cathode resistance resulting from the modified cathode polarization expression, as well as the unmodified anode and internal resistance, seemed valid compared to previous research [56, 57, 58]. Since the most significant polarization in a molten carbonate fuel cell is associated with the cathode, modifying the cathode polarization expression was a reasonable method to describe the DFC<sup>®</sup> fuel cell performance. The voltage for the modeled MCFC system operating in “tri-generation mode” for various current densities is shown in Figure 17 below.



**Figure 17. The fuel cell voltage dependence on current density for NG operation**

The average fuel cell voltage, power generated, and parasitic loads for the modeled and measured MCFC tri-generation system at specific operating conditions (refer to Table 19, Table 20, Table 21 ) is shown below in Table 28.

**Table 28. Measured and modeled voltage and power of the tri-generation system using NG**

<b>Output</b>	<b>Measured</b>	<b>Model</b>
Cell Voltage (Volts)	0.816	0.816
Gross DC Power (kW)	---	281.4
Gross AC Power (kW)	268.3	266.9
Hydrogen Separation Unit Load (kW)	61.5	58.9
Mechanical Balance-of-Plant Load (kW)	18.8	20.4
Net AC Power	188.0	187.6

The modeled values fit the measured values well since the model was modified for this particular operating condition.

### **5.2.2 Verification of Tri-generating Direct FuelCell<sup>®</sup> using Anaerobic Digester Gas**

The steady-state operating conditions for the tri-generation system fueled by anaerobic digester gas are listed in Table 29.

**Table 29. Model operating conditions for tri-generation fuel cell using ADG**

Parameter	Symbol	Description	Operating Condition
Fuel Utilization Factor	$U_F$	Fraction of hydrogen consumed electrochemically in fuel cell to the amount of hydrogen available to react	0.62
Current Density	$j$	Quantity of electric current flowing per unit cross-sectional area	1200 A / m <sup>2</sup>
Steam-to-Carbon Ratio	S/C	Molar. ratio of water to atomic carbon	2
Fuel Cell Stack Temperature	$T_s$	Average temperature of fuel cell stack	676.7°C
Fuel Cell Stack Pressure	$P_s$	Operating pressure inside stack	16 psia
PSA pressure	$P_{PSA}$	Operating pressure of PSA	150 psia
PSA inlet temperature	$T_{PSA}$	Operating temperature of PSA	15 °C

The fuel utilization, current density, and steam-to-carbon ratio was data obtained by the measured system operating at OCSD. The fuel cell stack temperature and pressure were not available for the measured system, so it was assumed to be the same as the verified fuel cell model in “normal operation” from 5.1 Verification of FuelCell Energy Direct FuelCell® Model. The PSA temperature and pressure values were explained in 4.3.3.3 Pressure Swing Adsorption (PSA) System.

Table 30 lists the stream conditions for the fuel, air, and water entering the tri-generating fuel cell system.

**Table 30. Input stream conditions for tri-generation fuel cell using ADG**

Stream	Flow Rate	Pressure	Temperature
Fuel	9.47 lbmol/hr	46 psia	85 °F
Air	72.4 lbmol/hr	15 psia	91 °F
Water	11.0 lbmol/hr	15 psia	211 °F

The fuel used was anaerobic digester gas, which was composed mostly of methane and carbon dioxide. The air composition was composed of oxygen and nitrogen, but also contained moisture. Also, the water entering the fuel cell system was free of impurities. The fuel, air, and water stream composition is summarized in Table 31 below.

**Table 31. Input stream composition for tri-generating DCF<sup>®</sup> model operating on ADG**

Stream	O <sub>2</sub> vol%	N <sub>2</sub> vol%	H <sub>2</sub> vol%	CO vol%	CO <sub>2</sub> vol%	CH <sub>4</sub> vol%	H <sub>2</sub> O vol%
Fuel	0.01000	0.6500	2.680	1.220	35.42	60.02	0
Air	78.30	20.70	1.010	0	0	0	0
Water	0	0	0	0	0	0	100.0

Again, the measured stream compositions were determined through gas chromatography performed by FuelCell Energy and the streams must be dry as possible for the gas to be analyzed. Therefore, the percent by volume of water is not available for most stream composition comparisons. The measured anode exhaust composition, modeled composition, and percent error for the tri-generation simulation are listed in Table 32 below.

**Table 32 Measured and modeled anode exhaust composition for ADG case**

<b>Species</b>	<b>Measured (vol%)</b>	<b>Model (vol%)</b>	<b>Percent Error</b>
H <sub>2</sub>	17.64	18.48	4.76
CO <sub>2</sub>	69.07	69.41	0.492
CO	9.16	11.88	29.7

The concentration of methane and nitrogen are negligible at the exit of the anode. The amount of hydrogen in the modeled anode exhaust was slightly higher than the measured volume percent. The volume percent of carbon dioxide and carbon monoxide modeled were also higher than the measured quantity. These results would have not made sense with the natural gas case because the volume percent of these species would have been strongly connected to the water-gas shift reaction. In this case, the high volume of carbon dioxide in the anaerobic digester gas adds complexity to the analysis of the stream results. The higher hydrogen concentration may indicate not enough of the hydrogen was utilized, raising concerns about the user-defined method of setting the fuel utilization. However, the “normal operation” and “tri-generating” cases on natural gas predicted hydrogen concentrations within 0.15 %, which is precise enough to discard the notion that the input fuel utilization is the cause of error. Carbon monoxide was grossly over-predicted, which would have indicated that not enough carbon monoxide was shifted in the previous cases. That is not true for this analysis, as the amount of hydrogen modeled should be less than the measured amount. However, the percent error associated with the carbon monoxide concentration for the modeled tri-generation system using natural gas is within 1 percent of the predicted value for this case. Therefore, the predicted value for carbon monoxide may be reasonable considering the same arguments made for the natural gas case applies equally in this

scenario. Carbon dioxide is interestingly within 1 percent of the measured value, but that level of accuracy is misleading. The anode exhaust is mostly composed of carbon dioxide, so the concentration does not vary as drastically as it does for species like hydrogen and carbon monoxide. Therefore, a change in the quantity of carbon monoxide or hydrogen impacts the mole fraction of the component in the stream compared to the same change in quantity for carbon dioxide. The discretization of the anode also does not explain the error in the predictions. The stream composition between the last DIR stage and the last reformation did not differ greatly, which indicates that the number of discretizing steps was sufficient to characterize the anode.

The measured high-temperature shift reactor exhaust composition, modeled composition, and percent error for the tri-generation simulation are listed in Table 33 below.

**Table 33. Composition of measured and modeled HTS reactor exhaust**

<b>Species</b>	<b>Measured (vol%)</b>	<b>Model (vol%)</b>	<b>Percent Error</b>
H <sub>2</sub>	21.97	24.66	12.2
CO <sub>2</sub>	72.33	71.73	0.830
CO	4.23	3.404	19.5

The amount of hydrogen in the modeled HTS exhaust was much higher than the measured volume percent. That may be due to the ideal performance of the modeled reactor versus a real water-gas shift reactor and catalyst. The amount of carbon dioxide and carbon monoxide modeled were lower than the measured value. Carbon dioxide volume and error percentage did not change significantly from the anode exhaust results since it is a major



component of the moisture-free high-temperature shift and anode exhaust. The carbon monoxide percent error changed was significantly closer to the true value compared to the modeled anode exhaust. That may have occurred because carbon monoxide in the stream shifted at a temperature that may be comparable to the same temperature the measured samples were taken.

The measured low-temperature shift reactor exhaust composition, modeled composition, and percent error for the tri-generation simulation are listed in Table 34 below.

**Table 34. Measured and modeled exhaust composition of LTS reactor**

<b>Species</b>	<b>Measured (vol%)</b>	<b>Model (vol%)</b>	<b>Percent Error</b>
H <sub>2</sub>	22.77	26.91	18.2
CO <sub>2</sub>	75.53	72.57	3.92
CO	3.250	0.3185	90.2

The amount of hydrogen in the modeled LTS exhaust was much higher than the measured volume percent because much more hydrogen was produced in the modeled HTS reactor upstream. The other reason may be due to the sub-par performance of the measured low-temperature shift reactor. The fraction of carbon dioxide in the modeled LTS outlet stream was lower than the measured value, which is a result of the overly high hydrogen yield predicted by the model. The 2 percent increase in hydrogen concentration also indicates that a large amount of carbon monoxide was shifted. The carbon monoxide volume percent is significantly erroneous. It may be that high for the same reason stated for the anode exhaust error. A change in the quantity

of carbon monoxide affects the percent error considerably compared to other species in the stream.

The measured cathode inlet composition for oxygen, nitrogen, and carbon dioxide is known and compared to the modeled stream. The measured and modeled composition and percent error for the tri-generation simulation for the cathode stream is listed in Table 35 below.

**Table 35 Measured and modeled cathode inlet composition and associated percent error**

<b>Species</b>	<b>Measured (vol%)</b>	<b>Model (vol%)</b>	<b>Percent Error</b>
O <sub>2</sub>	13.35	14.25	6.74
CO <sub>2</sub>	17.30	24.91	44.0
N <sub>2</sub>	67.14	60.85	9.37

The percent error associated with the modeled carbon dioxide concentration is extremely different. This result is odd as the carbon dioxide predications in most of the analyzed streams for all three cases have been fairly accurate. The oxygen concentrations are within ten percent, but again that is rare in contrast to previous results. The measured cathode inlet includes 2.12 percent by volume of methane, 0.03 percent by volume of ethane, and 0.04 percent by volume of hydrogen, which does not seem accurate as these concentrations were below or zero in the low-temperature shift exhaust. Thus the errors associated with this set of results will be regarded as loosely accurate, as there are no other additional sources of data to assist the analysis of the cathode inlet.

The measured cathode exhaust composition for oxygen, nitrogen, and carbon dioxide is known and compared to the modeled stream. The measured and modeled composition and percent error for the tri-generation simulation for the cathode stream is listed in Table 36 below.

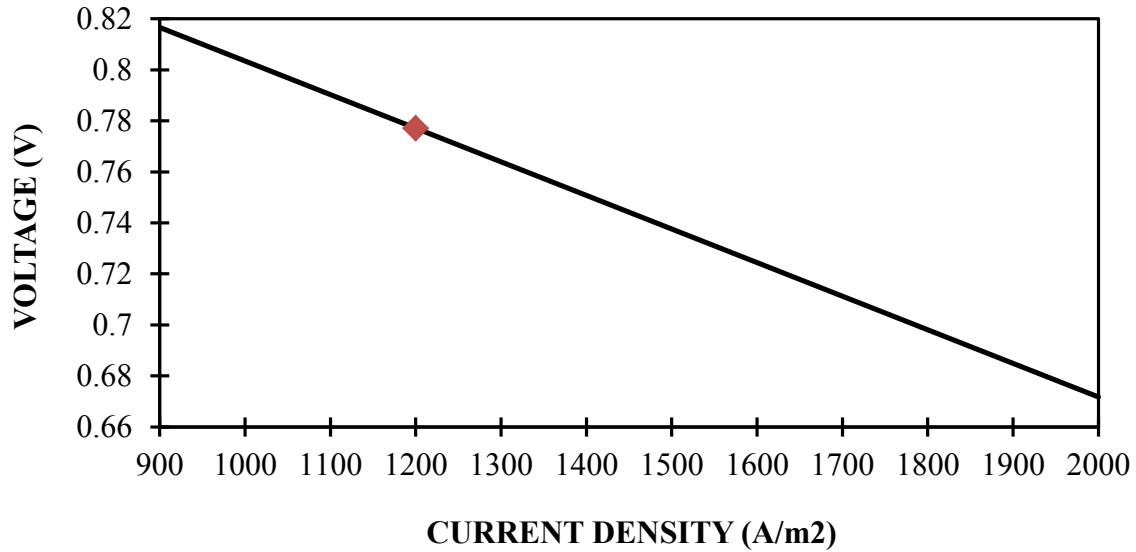
**Table 36. Measured and modeled cathode inlet composition and percent error**

<b>Species</b>	<b>Measured (vol%)</b>	<b>Model (vol%)</b>	<b>Percent Error</b>
O <sub>2</sub>	9.970	8.532	14.4
CO <sub>2</sub>	9.540	12.40	30.0
N <sub>2</sub>	78.03	79.07	1.33

The amount of carbon dioxide exiting the modeled cathode is much higher than the measured composition, but percent error dropped 44% from the cathode inlet to 30% in the cathode exhaust. The higher concentration of carbon dioxide was expected since the concentration of carbon dioxide for the modeled tri-generation system was consistently higher than the recorded value. There is a slight difference between the measured and modeled composition of nitrogen, which is a significant improvement from the 9.37 percent error seen in the analysis of the cathode inlet. The percent error for the modeled and measured oxygen in the cathode exhaust more than doubled from the error calculated for the cathode inlet. If the fuel utilization was not high enough, as discussed for the hydrogen composition error in the anode exhaust, the predicted percent of higher should have been higher, not lower than the measured value. Again, there is a discrepancy with the data collected for the cathode exhaust. The measured cathode outlet includes 2.40 percent by volume of methane, 0.04 percent by volume of

ethane, and 0.01 percent by volume of hydrogen, which does not seem accurate as there were no detectable quantities of those species in the cathode exhaust for the natural gas case at similar operating conditions. At least for the modeled tri-generation system operating on anaerobic digester gas, the predicted cathode inlet and outlet streams may not be representative of the measured streams.

The voltage for the modeled MCFC tri-generation system operating on anaerobic digester gas was determined in the same fashion as the natural gas case described in 5.2.1 Verification of Tri-generating Direct FuelCell<sup>®</sup> using Natural Gas. The anode resistance was multiplied by a factor of 7.02 so that the modeled voltage matched the empirical value for the operating conditions listed in Table 29, Table 30, and Table 31. The cathode resistance was multiplied by the same factor as the natural gas case. The voltage for the modeled MCFC system operating on anaerobic digester gas in “tri-generation mode” for various current densities is shown in Figure 18 below.



**Figure 18. The fuel cell voltage dependence on current density for ADG operation**

The average fuel cell voltage, power generated, and parasitic loads for the modeled and existing MCFC tri-generation system at specific operating conditions (refer to Table 29, Table 30, and Table 31) is shown below in Table 37.

**Table 37. Measured and modeled voltage and power for tri-generation system using ADG**

<b>Output</b>	<b>Measured</b>	<b>Model</b>
Cell Voltage (Volts)	0.777	0.777
Gross DC Power (kW)	---	270.7
Gross AC Power (kW)	260	259.9
Hydrogen Separation Load (kW)	66	65.3
Mechanical Balance-of-Plant Load (kW)	20	19.6
Net AC Power	175	175.0

The modeled values fit the measured values well, which is to be expected since the model was tuned for this particular operating condition.

## Chapter 6:      **Model Evaluation**

Parametric studies were performed to evaluate the performance characteristics of a tri-generating fuel cell using natural gas and anaerobic digester gas. The model generated values for the following 18 variables:

1. Average fuel cell operating cell voltage
2. Nernst voltage
3. Average cathodic cell loss
4. Average anodic cell loss
5. Average ohmic cell loss
6. Average total cell loss
7. Gross power
8. Net power
9. DC-AC conversion load
10. Mechanical balance-of-plant power load
11. Hydrogen separation unit load
12. Hydrogen production rate
13. Waste heat availability
14. Electrical efficiency
15. Hydrogen production efficiency
16. Combined power and hydrogen efficiency

for fuel utilizations between 0.4 and 0.9 (equivalently 40 to 90 percent) and current densities between 900 and 2000 A/m<sup>2</sup>. The fuel, air, and water inputs were held constant for the parametric studies. Two parametric studies were run for four different hydrogen production rates for each fuel. The hydrogen production rate was based on hydrogen recovery percentage for the PSA unit, which was a user input option for the model. The four scenarios included hydrogen recovery percentages of 60, 70, 80, and 90.

The evaluation focuses on characterizing and distinguishing the performance of the tri-generation fuel cell system operating on two different fuels, natural gas and anaerobic digester gas, in conjunction with varying rates of hydrogen export. Therefore, eight different cases will be evaluated in this chapter:



**Table 38. List of scenarios resulting from parametric studies**

<b>Case Number</b>	<b>Case Name</b>	<b>Fuel Type</b>	<b>Hydrogen Recovery Percentage</b>
1	NG90	Natural Gas	90
2	NG80	Natural Gas	80
3	NG70	Natural Gas	70
4	NG60	Natural Gas	60
5	ADG90	Anaerobic Digester Gas	90
6	ADG80	Anaerobic Digester Gas	80
7	ADG70	Anaerobic Digester Gas	70
8	ADG60	Anaerobic Digester Gas	60

In order to directly compare the performance of the tri-generation fuel cell system operating on natural gas to the system using anaerobic digester gas, the operating conditions and feed streams must be the equivalent. The operating conditions used in the parametric studies for tri-generating fuel cell model using either natural gas or anaerobic digester gas are shown in Table 39.

**Table 39. Operating conditions for parametric studies of tri-generating fuel cell**

<b>Parameter</b>	<b>Symbol</b>	<b>Description</b>	<b>Operating Condition</b>
Fuel Cell Stack Temperature	$T_s$	Average temperature of fuel cell stack	676.7 °C
Fuel Cell Stack Pressure	$P_s$	Operating pressure inside stack	16 psia
PSA pressure	$P_{PSA}$	Operating pressure of PSA	150 psia
PSA inlet temperature	$T_{PSA}$	Operating temperature of PSA	15 °C

The fuel, air, and water input for the natural gas case discussed in 5.2.1 Verification of Tri-generating Direct FuelCell® using Natural Gas is used as the basis for the parametric studies. The energy content for both fuels must be equivalent for the accurate comparison of the extrinsic variables of the system. Thus, the lower heating value for the exact composition of anaerobic digester gas utilized was calculated and used to derive the equivalent flow rate of ADG. The fuel, air, and water inputs for the parametric studies are provided in Table 40.

**Table 40. Input stream conditions for parametric studies of a tri-generating fuel cell**

<b>Stream</b>	<b>Flow Rate</b>	<b>Pressure</b>	<b>Temperature</b>
Natural Gas	5.44 lbmol/hr	46 psia	94 °F
Anaerobic Digester Gas	8.95 lbmol/hr	46 psia	94 °F
Air	62.0 lbmol/hr	15 psia	91 °F
Water	11.0 lbmol/hr	15 psia	211 °F

The following sections contain the results of the parametric studies.

## 6.1 Nernst Voltage

The Nernst voltage for an individual molten carbonate fuel cell in “tri-generation mode” at varying fuel utilizations for each scenario is illustrated in Figure 19.

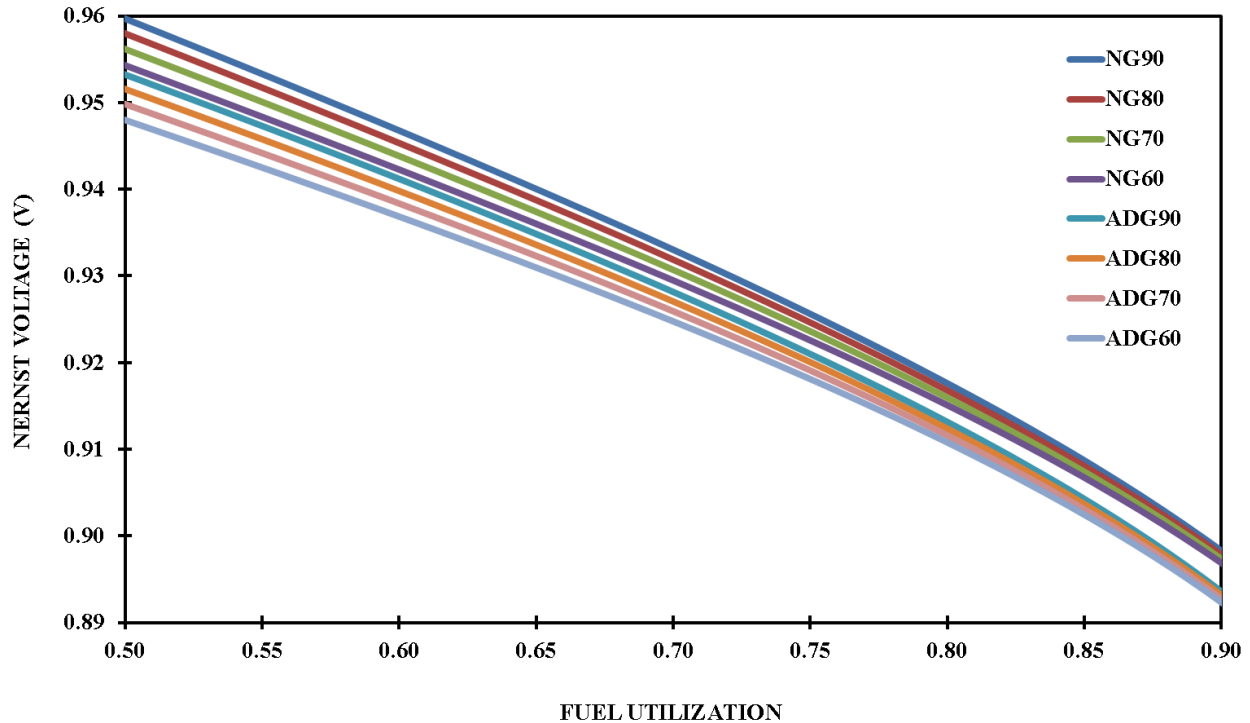


Figure 19. Nernst voltage for eight cases at varying fuel utilization

The Nernst voltage, presented as Equation 3-19, is a function of the partial pressures of hydrogen in the anode, oxygen in the cathode, carbon dioxide in the anode and cathode, and water in the anode. The increase in the partial pressures of hydrogen in the anode, and oxygen and carbon dioxide in the cathode leads to an increase in Nernst voltage. The partial pressure of

hydrogen in the anode decreases as more hydrogen is utilized to produce electricity. Therefore, the Nernst voltage decreases with increasing fuel utilization for every modeled case.

The Nernst voltage decreases with increasing partial pressures of carbon dioxide and water in the anode. Carbon dioxide approximately composes 35 percent of anaerobic digester gas versus one percent of natural gas, which results in a significantly larger carbon dioxide partial pressure in the anode and cathode for anaerobic digester gas operation than natural gas operation. Therefore, the Nernst voltage for the tri-generation fuel cell system is always higher for natural gas operation than anaerobic digester gas operation.

For both fuels, larger hydrogen recovery percentages result in higher Nernst voltages. Since the hydrogen exported is separated from the anode exhaust, the partial pressure of hydrogen in the anode is not affected by the hydrogen recovery percentage. However, the oxygen and carbon dioxide partial pressures in the cathode are directly affected by the hydrogen recovery percentage. The flow rate of air, and therefore flow rate of oxygen, entering the tri-generation system is constant. The air is heated in the hydrogen concentration unit and then enters the oxidizer to react with hydrogen and carbon monoxide remaining in the hydrogen separation unit exhaust. The oxidizer exhaust then enters the cathode as the fuel cell oxidant stream. The concentration of hydrogen in the hydrogen separation unit exhaust decreases with increasing hydrogen recovery percentages. Since less oxygen is consumed to oxidize hydrogen in the oxidizer, the partial pressure of oxygen in the cathode increases for greater hydrogen recovery percentages. Consequently, the Nernst voltage increases with increasing percentages of hydrogen recovery.

The difference between the Nernst voltage for each hydrogen recovery case decreases with fuel utilization. This phenomenon is due to the decreasing availability of hydrogen to recover for export at increasing fuel utilization. For instance, the quantity of hydrogen in the anode exhaust at 90 percent fuel utilization is significantly less than the quantity available at 60 percent. In turn, the hydrogen remaining after separation at 90 percent fuel utilization is also significantly less than the quantity available at 60 percent fuel utilization regardless of the percentage of hydrogen exported. Therefore, less oxygen is consumed at higher fuel utilizations, reducing the effect that hydrogen recovery has in increasing the partial pressures of oxygen in the cathode. Thus, the effect of 60, 70, 80, 90 percent hydrogen recovery on the Nernst voltage decreases significantly for higher fuel utilizations.

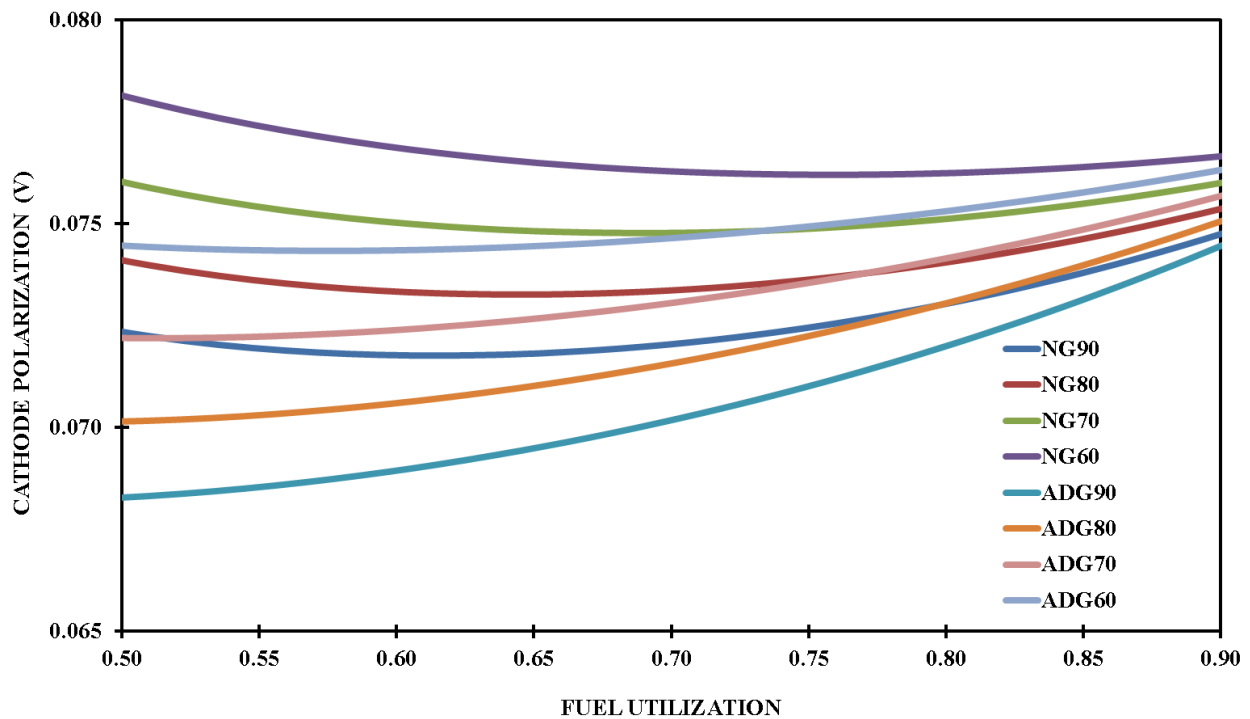
The Nernst voltage does not account for irreversible losses in the fuel cell. The next section will discuss the fuel cell irreversibilities for the eight scenarios resulting from the parametric studies

## 6.2 Voltage Losses

Three types of irreversible fuel cell losses were described in 4.3.1.10 Voltage: cathode polarization, anode polarization, and ohmic loss. The sum of these losses results in the difference between the Nernst voltage and fuel cell operating voltage. The cathode, anode, and total cell loss will be presented below. The ohmic loss, as expressed in Equation 3-22, is only a function of the fuel cell stack temperature. The modeled scenarios operate at the same fuel cell stack

temperature, thus the ohmic loss for every scenario is identical and a graphical depiction is redundant. For reference, the value for the ohmic loss is 0.0337 volts.

The most significant irreversibility in the cell is the cathode polarization. The cathode polarization for each scenario is shown in Figure 20.



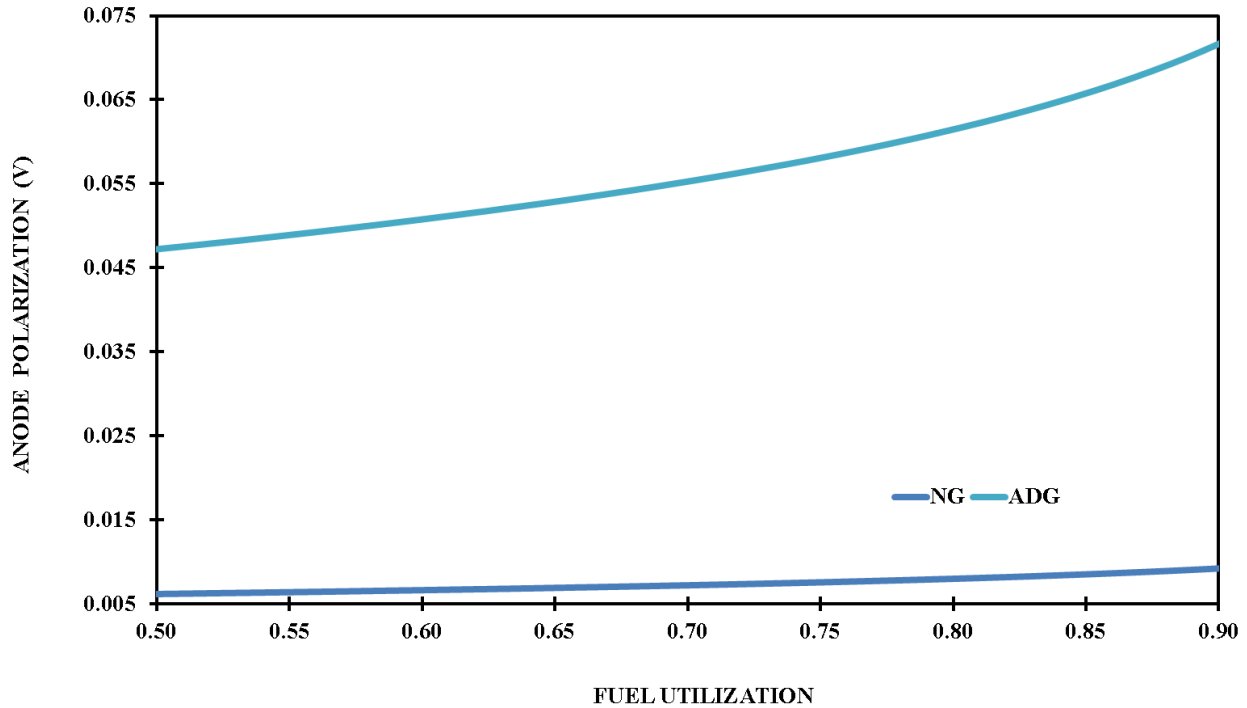
**Figure 20. Cathode polarization for tri-generation fuel cell system at various fuel utilizations and hydrogen recovery percentages**

The expression for the cathode polarization was presented as Equation 3-21 in 4.3.1.10 Voltage. The cathode polarization increases with increasing partial pressures of carbon dioxide

in the cathode. Increasing the partial pressure of oxygen in the cathode decreases the cathode polarization. The following trends occur due to these relationships:

- As explained in the previous section, the partial pressure of carbon dioxide is significantly larger for anaerobic digester gas than natural gas in both the anode and cathode compartments. The cathode polarization associated with ADG operation is less than natural gas use at a specific hydrogen recovery percentage. However, the difference between the natural gas and anaerobic digester gas cathode polarizations at a specific hydrogen recovery percentage decreases with increasing polarization, and nearly converges at 90 percent fuel utilization.
- As discussed in the previous section, higher percentages of hydrogen recovery lead to higher partial pressures of oxygen in the cathode. Therefore, the cathode polarization for a tri-generating MCFC decreases with higher hydrogen recovery.
- The effect hydrogen recovery has on the partial pressure of oxygen in the cathode decreases with increasing fuel utilization, as stated in 6.1 Nernst Voltage. The cathode polarization curves for each fuel roughly converges at 90 percent fuel utilization due to the diminishing effect of hydrogen recovery at higher fuel utilizations. Hence, the effect of hydrogen recovery on cathode polarization decreases with increasing fuel utilization.

The anode polarization composes a substantial fraction of the total irreversible cell losses and is presented in Figure 21.



**Figure 21. Anode polarization for tri-generation fuel cell system at various fuel utilizations and hydrogen recovery percentages**

The expression for the anode polarization was presented as Equation 3-20 in 4.3.1.10 Voltage. The anode polarization decreases as the partial pressure of hydrogen in the anode increases. Hydrogen recovery does not affect the hydrogen partial pressure found in the anode, therefore anode polarization in the fuel cell is independent of hydrogen recovery. As a result of this relationship, the following trends are true for the anode polarization of a tri-generating molten carbonate fuel cell:

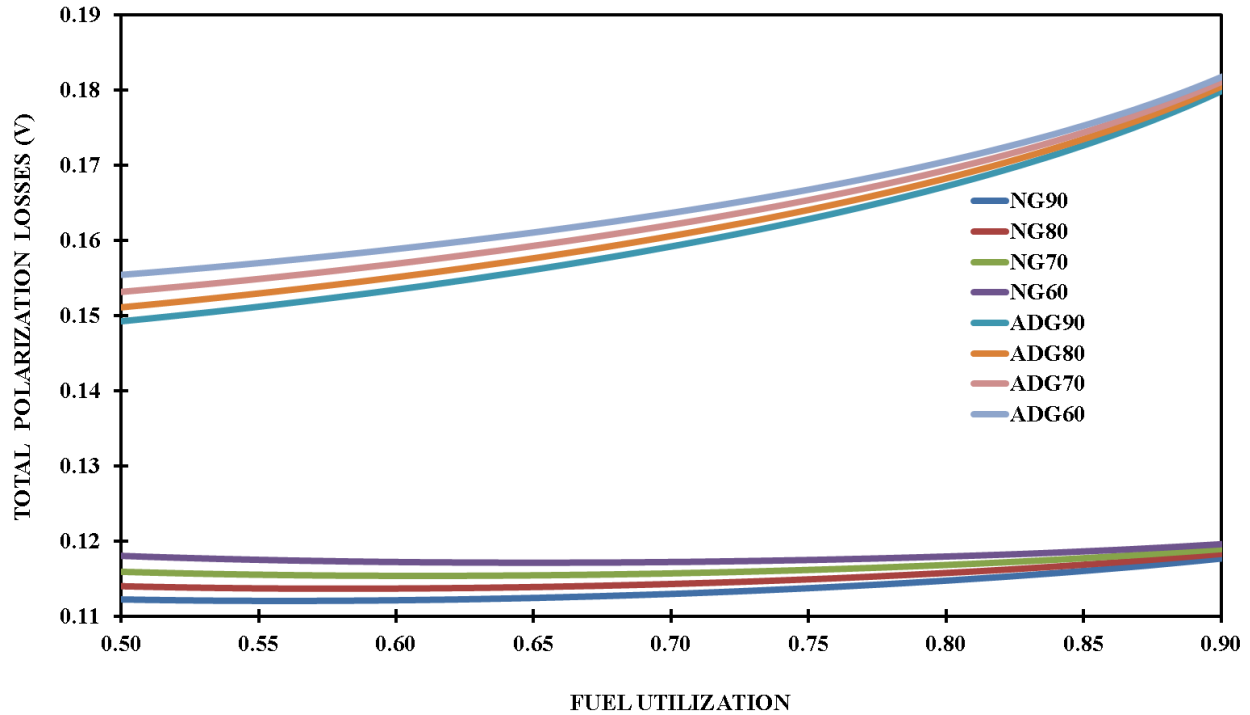
- The concentration of hydrogen decreases in the anode with increasing fuel utilization regardless of the fuel type. Since the partial pressure of hydrogen is directly proportionally to concentration, the partial pressure also decreases for



increasing fuel utilization. Thus, the anode polarization increases with fuel utilization.

- The hydrogen available in anaerobic digester gas or natural gas is derived from its main chemical constituent, methane. The percentage of methane in ADG is 65 percent, which is considerably less than the 96 percent found in NG. Thus, the amount of hydrogen produced by direct and indirect internal reformation during ADG operation is lower than the amount of hydrogen produced when operating on NG. The partial pressure of hydrogen in the anode for a tri-generating fuel cell is lower for NG operation versus operation on ADG as a result.

Based on the modeled values for each polarization, the cathodic loss is twice the magnitude of the ohmic loss and over four times the magnitude of the anodic loss. These results are consistent with the losses observed in modeled molten carbonate fuel cells [47, 58, 59], as well as the measured cathode polarization for a FCE molten carbonate fuel cell [49]. The losses increase with higher fuel utilizations, which is also typical of a molten carbonate fuels [59] and fuel cells in general [17]. Since the sum of the three irreversible fuel cell losses is described as the total polarization loss, the characterization of the total polarization losses is deemed realistic. Figure 22 below depicts the total polarization loss for each scenario at fuel utilizations ranging from 0.4 to 0.9.



**Figure 22. Total polarization losses for modeled scenarios at varying fuel utilizations**

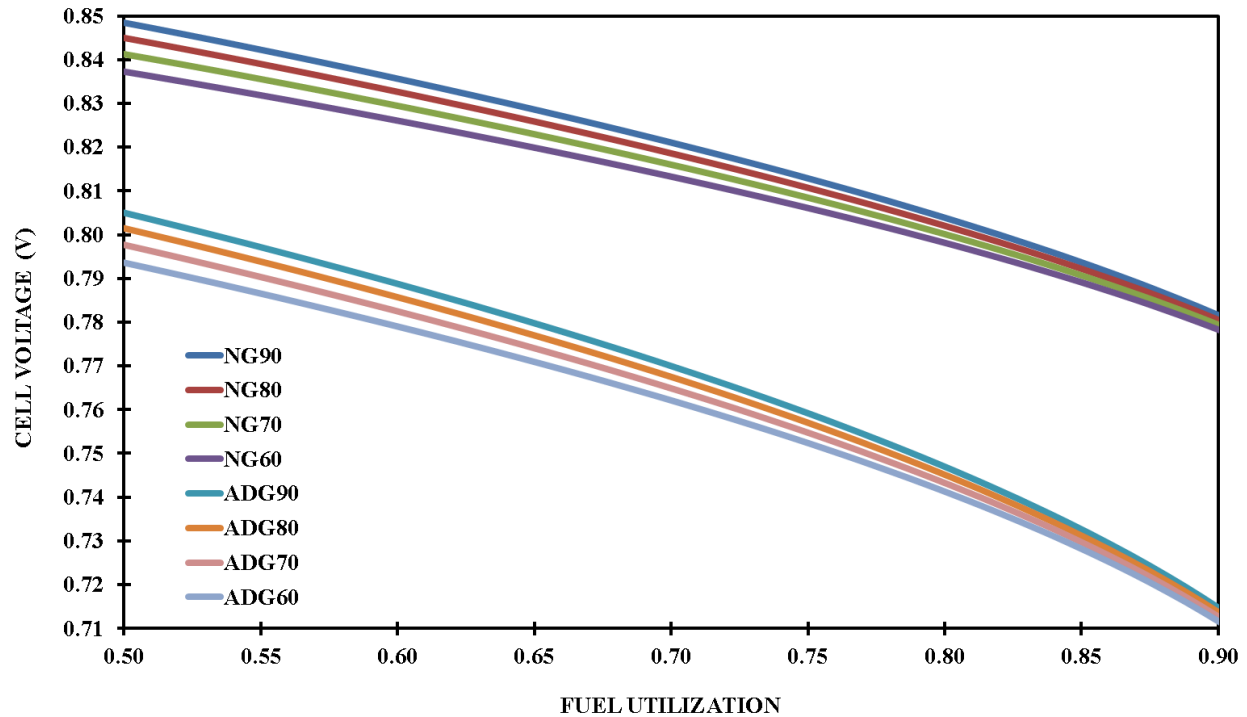
The effects of all three irreversibilities determine the magnitude of the total polarization. Since the total polarization is the sum of the irreversibilities, the overall trend for the total polarization is also a sum of the trends seen for the cathode, anode, and ohmic polarization. The cathode polarization is the only cell loss that is affected by hydrogen recovery, therefore the relationship between total polarization and hydrogen recovery is solely dictated by the cathode polarization-hydrogen recovery correlation. The losses at the cathode and anode were greater for ADG operation in comparison to NG use. Therefore, the following conclusions are true of a tri-generating MCFC :

- The total polarization decreases with higher hydrogen recovery.

- The effect of hydrogen recovery on total polarization decreases with increasing fuel utilization.
- The total polarization associated with anaerobic digester gas usage is greater than operating on natural gas.

### 6.3 Fuel Cell Operating Voltage

The fuel cell operating voltage is the difference between the Nernst voltage discussed in 6.1 Nernst Voltage and the irreversible voltage losses covered in section 6.2 Voltage Losses. The results for the fuel cell operating voltages associated with the eight modeled scenarios are display in Figure 23.



**Figure 23. Fuel cell operating voltage for varying fuel utilizations for eight tri-generation cases**

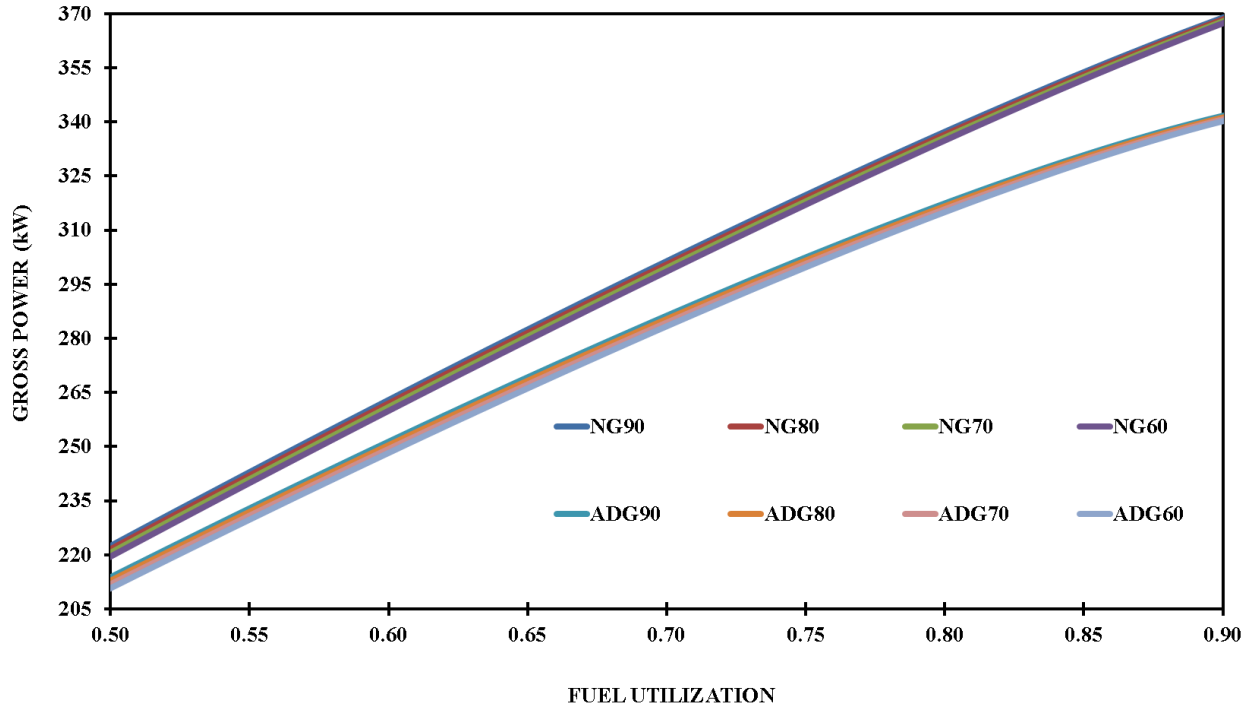
The fuel cell operating voltage is a product of the relationships described for the reversible voltage in 6.1 Nernst Voltage and each polarization loss in 6.2 Voltage Losses. The following conclusions are true for a tri-generating MCFC:

- The fuel cell operating voltage decreases with increasing fuel utilization for every modeled case.
- The fuel cell operating voltage is approximately 5 percent higher for natural gas operation than anaerobic digester gas operation.
- The fuel cell operating voltage increases with increasing percentages of hydrogen recovery.

- The effect of hydrogen recovery on the fuel cell operating voltage decreases with increasing fuel utilization.

## 6.4 Gross Power

The gross power generated by a molten carbonate fuel cell stack in “tri-generation mode” at varying fuel utilizations for each scenario is illustrated in Figure 24.



**Figure 24. Gross power generation for tri-generating MCFC at various fuel utilizations**

The gross power, presented as Equation 3-29 in 4.3.1.11 Power Generation and Parasitic Loads, is a directly proportional to the fuel cell operating voltage and rate of oxygen

consumption. The oxygen electrochemically reacted in the fuel cell is dictated by the fuel utilization fraction. The gross power increases with fuel utilization because more fuel and oxygen is consumed to generate electricity. Therefore, the gross power increases with increasing fuel utilization for every modeled case.

The gross power for NG operation is clearly greater than ADG operation when analyzing Figure 24. This result is explainable since gross power is proportional to cell voltage and the cell voltage for ADG operation is lower than NG use. Thus, the gross power for a tri-generation MCFC operating on natural gas is greater than using anaerobic digester gas.

A closer look at Figure 24 would provide a better opportunity to analyze the results. The following figure shows gross power results for fuel utilizations between 0.6 and 0.7.

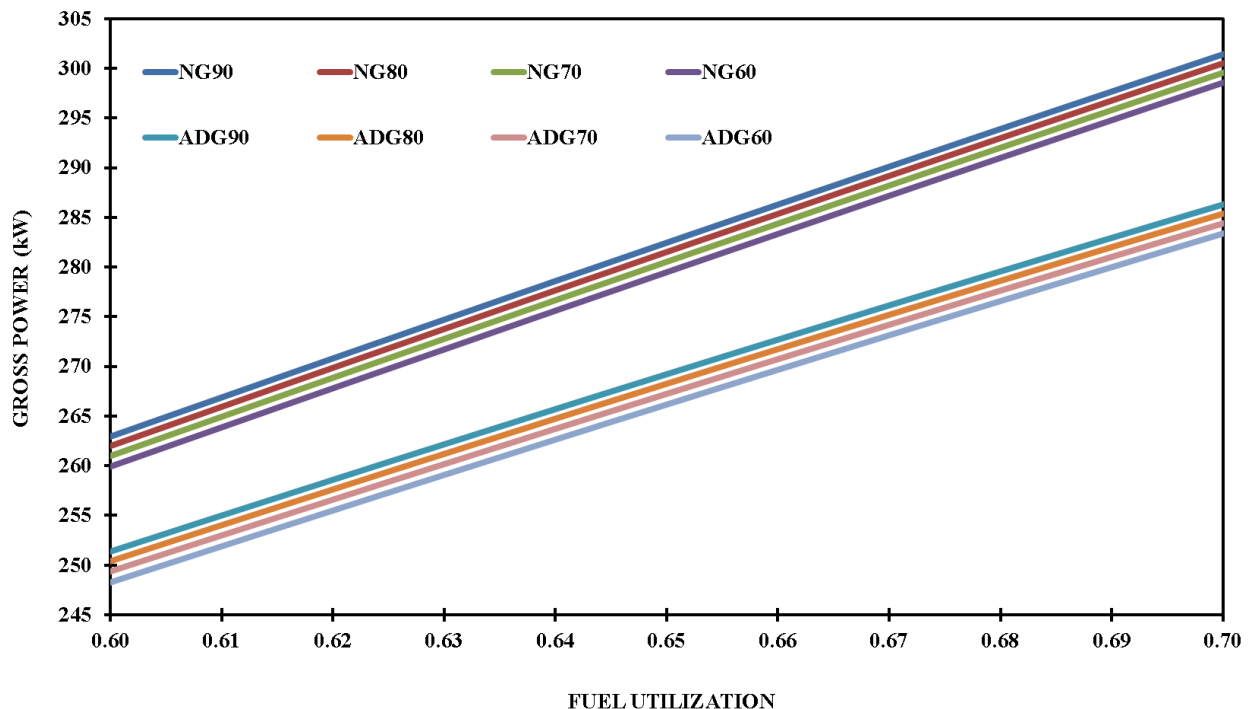


Figure 25. Gross power generation for tri-generating MCFC at 0.6 to 0.7 fuel utilization

The fuel utilization range was narrowed down to 0.6 and 0.7, since it is most viable operation range for a tri-generation fuel cell system. The DFC does not normally operate beyond 75 percent utilization and would not most likely exceed 70 percent fuel utilization in “tri-generation mode” for the purposes of exporting hydrogen. The lower boundary of 60 percent is a conservative assessment of the minimum fuel utilization for a DFC system without supplemental heat or power. Nonetheless, the trends occurring in the 0.6—0.7 range are still representative of entire fuel utilization range.

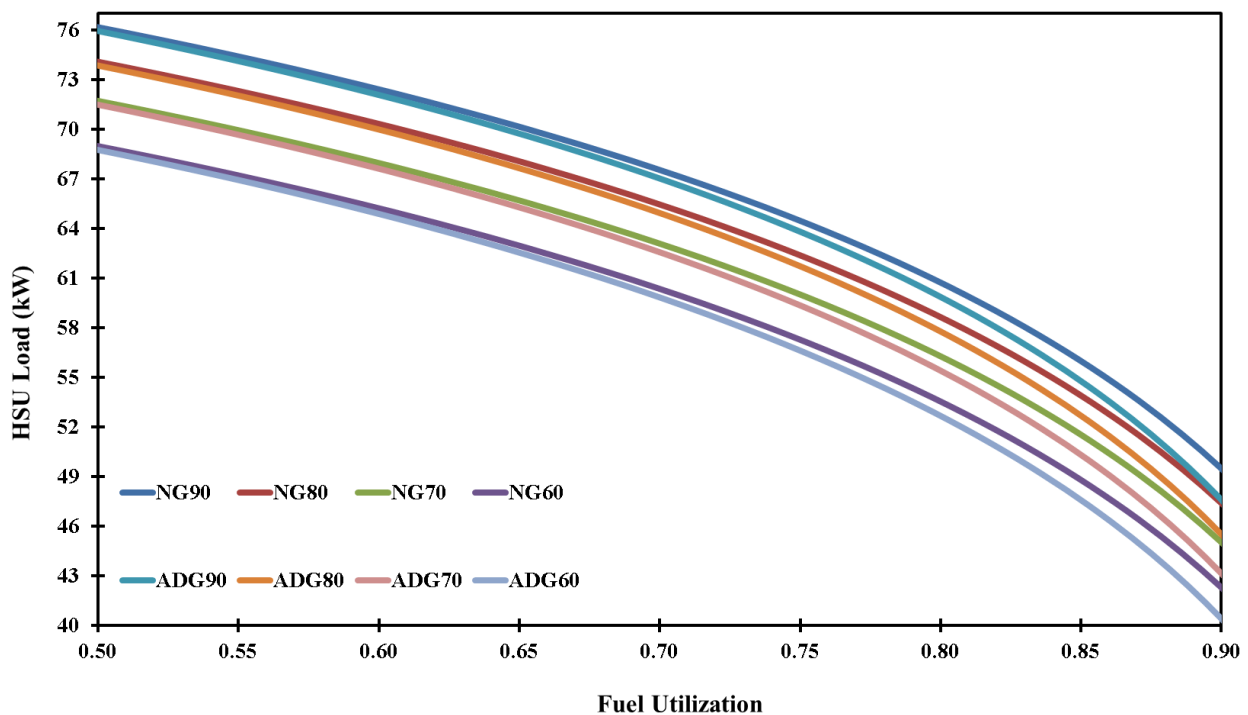
For both fuels, larger hydrogen recovery percentages result in higher gross power generation. Gross power is proportional to the fuel cell operating voltage and the fuel cell operating voltage increases for greater hydrogen recovery. Consequently, gross power increases with increasing percentages of hydrogen recovery.

The difference between the fuel cell operating voltage for each hydrogen recovery case decreases with fuel utilization and was discussed in 6.3 Fuel Cell Operating Voltage. It is not evident in Figure 25 that a convergence similar to the results in Figure 19, Figure 20, Figure 22, and Figure 23 exists. However, a detailed inspection of data revealed that the phenomenon subtly carries on in the generation of power. Thus, the effect of 60, 70, 80, 90 percent hydrogen recovery on gross power decreases for higher fuel utilizations.

## 6.5 Parasitic Loads

Three types of parasitic loads were described in 4.3.1.11 Power Generation and Parasitic Loads: HSU, mBOP, and DC—AC conversion. The sum of these losses results in the difference between the gross power and net power. The HSU, mBOP, and DC—AC conversion loads will be presented below.

The major parasitic load in the system is the HSU and is depicted in Figure 26 for the eight scenarios.



**Figure 26. HSU load for varying fuel utilizations and hydrogen recovery percentages**

The expression for the HSU load was presented as Equation 3-31 in 4.3.1.11 Power Generation and Parasitic Loads. The HSU load increases with greater rates of exported hydrogen. Therefore, the HSU load increases with higher hydrogen recovery percentages.



As mentioned in 6.2 Voltage Losses, the amount of hydrogen produced by direct and indirect internal reformation during ADG operation is lower than the amount of hydrogen produced when operating on NG. That results in less hydrogen being available for separation from the tri-generation system operating on ADG than for the system operating on natural gas. Consequently, the HSU load for a tri-generating molten carbonate fuel cell system using natural gas is greater than operating on anaerobic digester gas.

The difference between ADG and NG HSU loads at the same hydrogen recovery percentage increases with increasing fuel utilization. The divergence occurs due to the decreasing availability of hydrogen at high fuel utilizations for the ADG-fueled tri-generation systems. Therefore, the HSU load for a tri-generating molten carbonate fuel cell system using anaerobic digester gas is increasingly less than using natural gas operation at higher fuel utilizations.

The mBOP contributes substantially to the total parasitic load on the system and is presented in Figure 27 below.

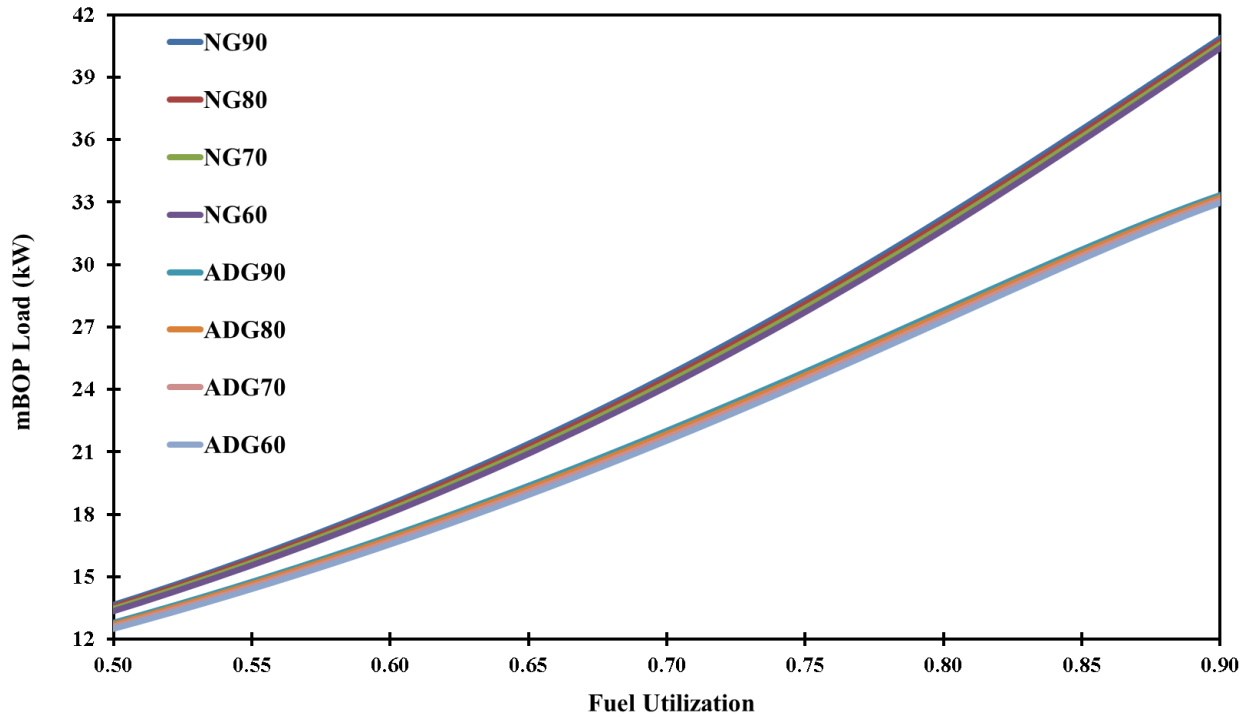
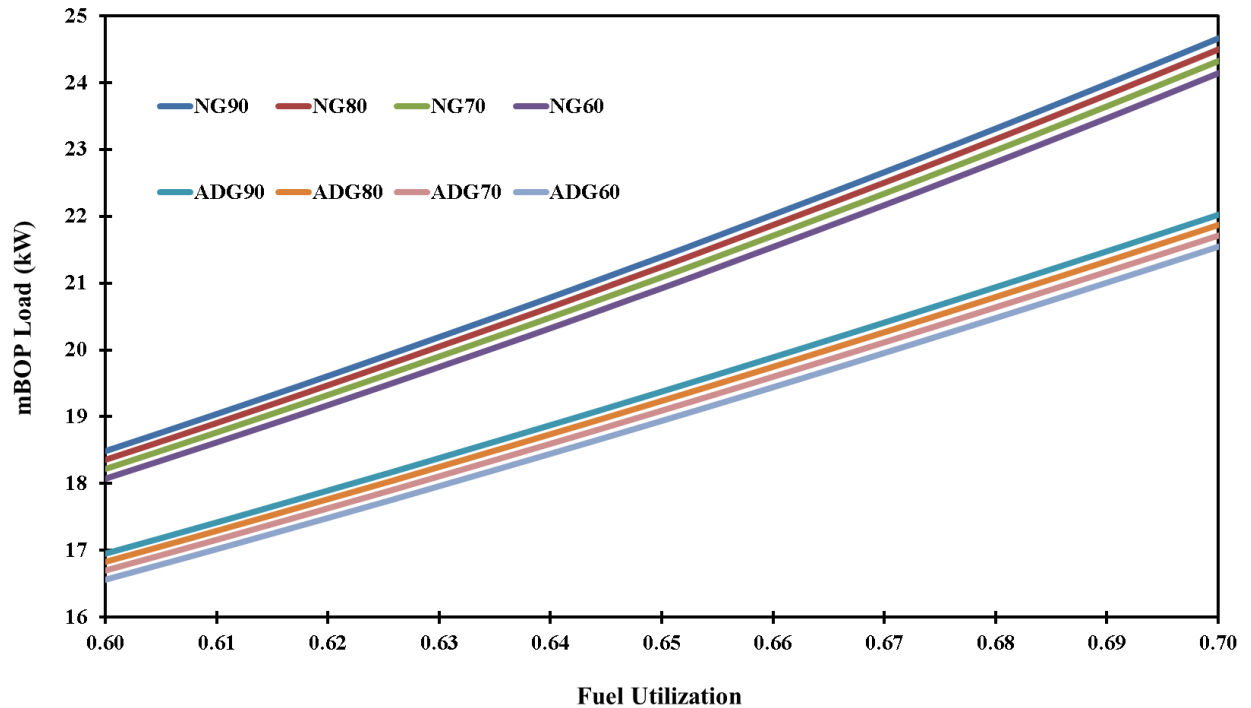


Figure 27. mBOP load for varying fuel utilizations and hydrogen recovery percentages

The expression for the mBOP load was presented as Equation 3-30 in 4.3.1.11 Power Generation and Parasitic Loads. The mBOP load increases with greater power production. As mentioned in the last section, gross power increases with increasing fuel utilization. Therefore, the mBOP load increases with increasing fuel utilization.

The gross power for NG operation is greater than ADG operation. Since the mBOP load is proportional to gross power, the greater load for NG-fueled tri-generation system seen in Figure 27 is expected. Thus, the mBOP load for a tri-generation MCFC operating on natural gas is greater than using anaerobic digester gas.

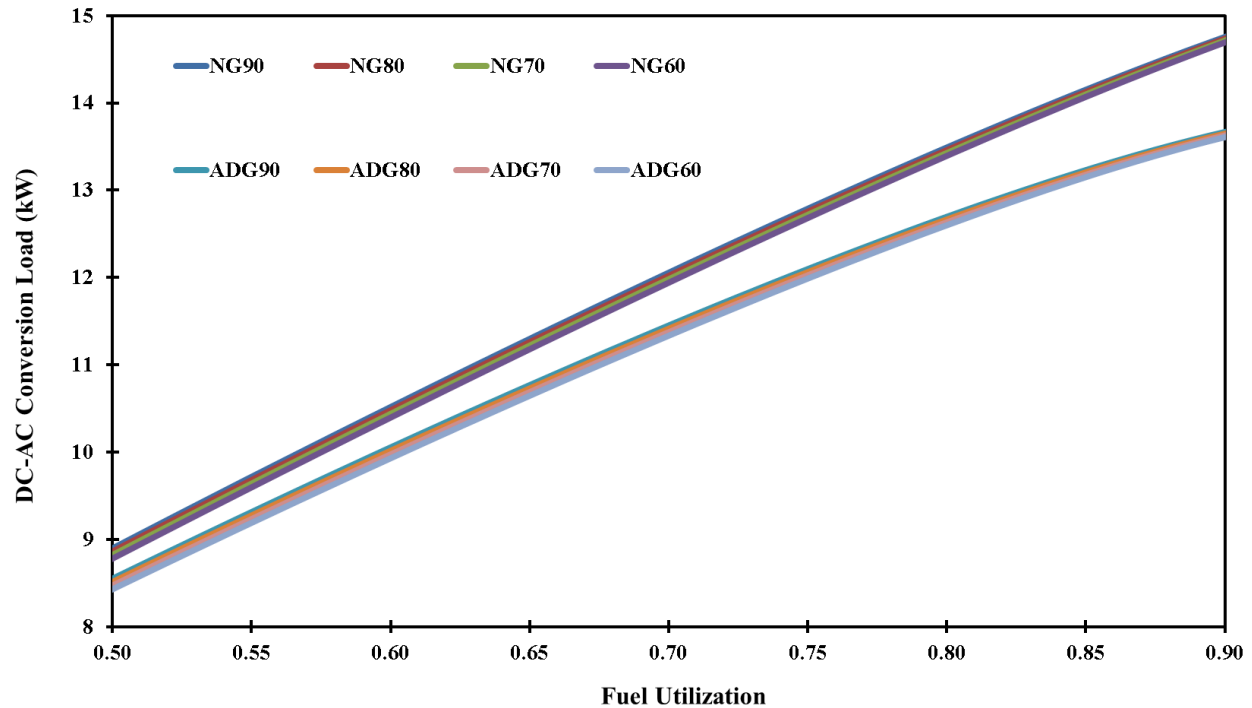
A closer look at Figure 27 would provide a better opportunity to analyze the results. Figure 28 shows gross power results for fuel utilizations between 0.6 and 0.7.



**Figure 28. mBOP load for fuel utilizations between 0.6 and 0.7**

Larger hydrogen recovery percentages result in higher mBOP loads for both fuels. The mBOP load is proportional to gross power and gross power increases for greater hydrogen recovery. Consequently, the mBOP load increases with increasing percentages of hydrogen recovery.

Lastly, the DC—AC conversion load is shown in Figure 29 below for eight scenarios.



**Figure 29. DC—AC conversion load for varying fuel utilizations and hydrogen recovery**

The DC—AC conversion load is directly proportional to gross power production. The following relationships can be stated based on the correlation between gross power and the DC—AC conversion load:

- The DC—AC conversion load increases with increasing fuel utilization.
- The DC—AC conversion load for a tri-generation MCFC operating on natural gas is greater than using anaerobic digester gas.

A closer look at Figure 29 would provide a better opportunity to analyze the results.

Figure 30 shows the DC—AC conversion load for fuel utilizations between 0.6 and 0.7.

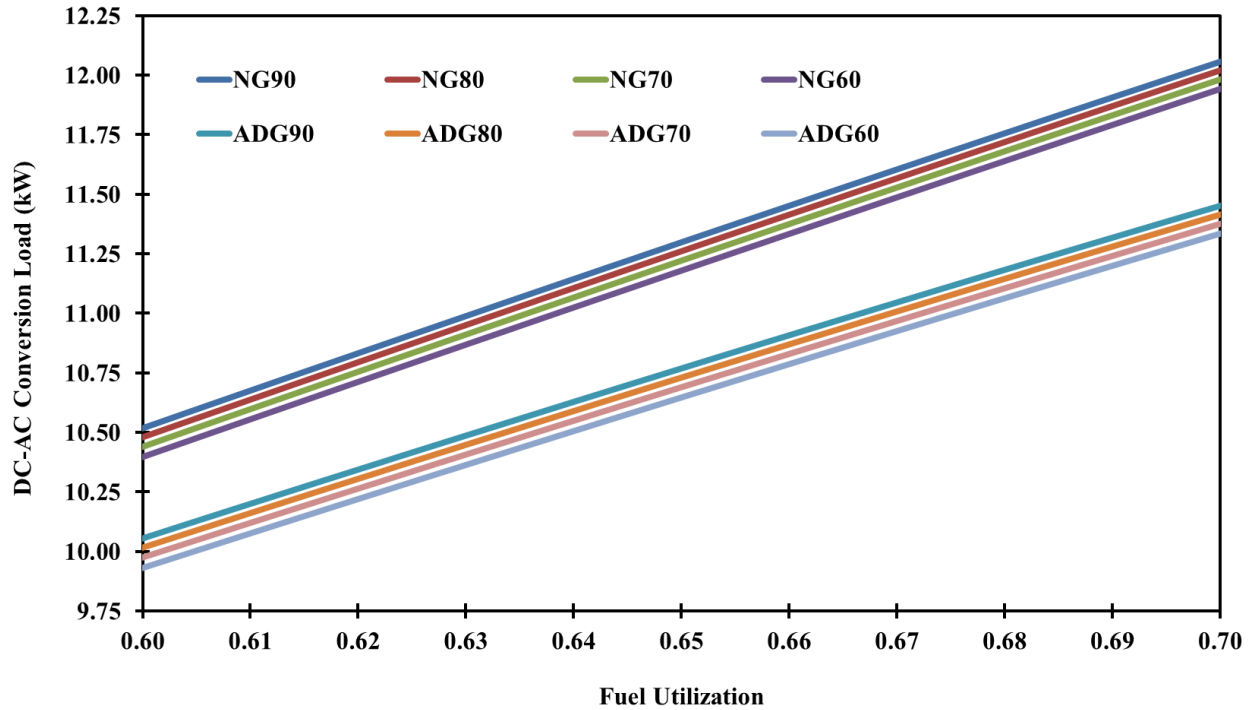


Figure 30. DC—AC conversion load for 0.6—0.7 fuel utilization

Larger hydrogen recovery percentages result in higher DC—AC conversion loads for both fuels. The DC—AC conversion load is proportional to gross power and gross power increases for higher hydrogen recovery. Consequently, the DC—AC conversion load increases with increasing percentages of hydrogen recovery.

## 6.6 Net Power

The net power is the difference between the gross power discussed in 6.4 Gross Power and parasitic loads covered in 6.5 Parasitic Loads. The results for the net power associated with the eight modeled scenarios are display in Figure 31.

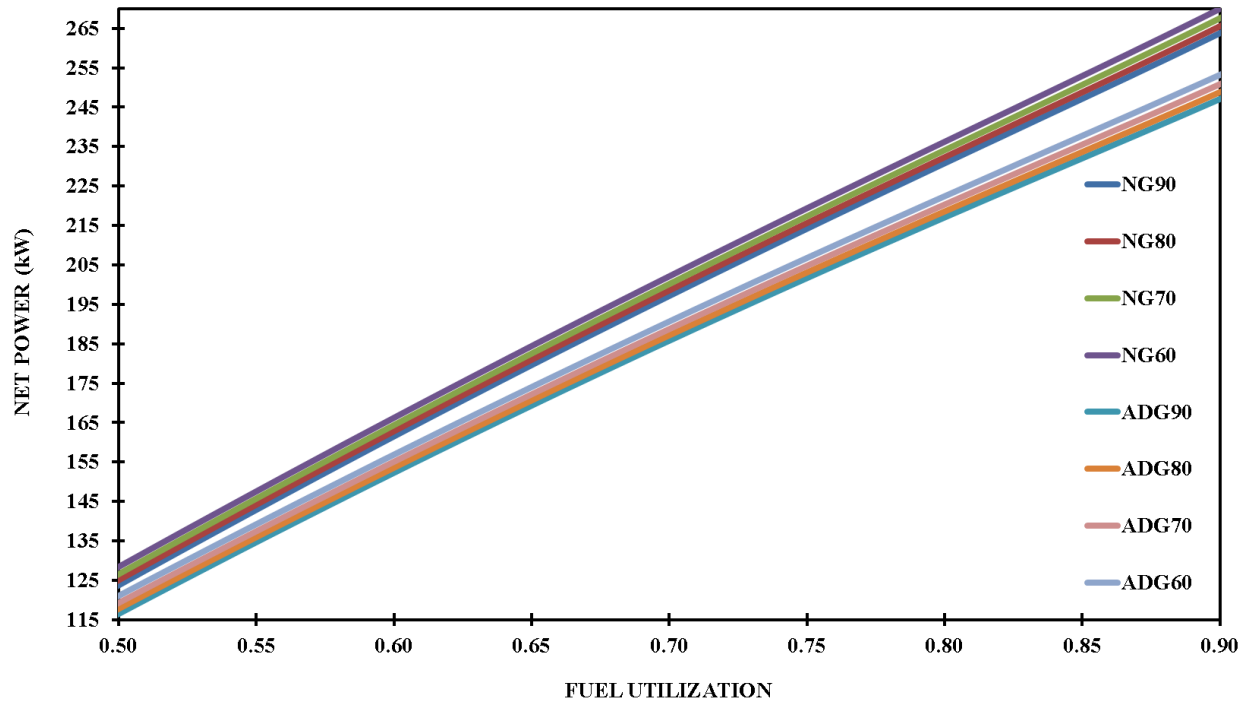
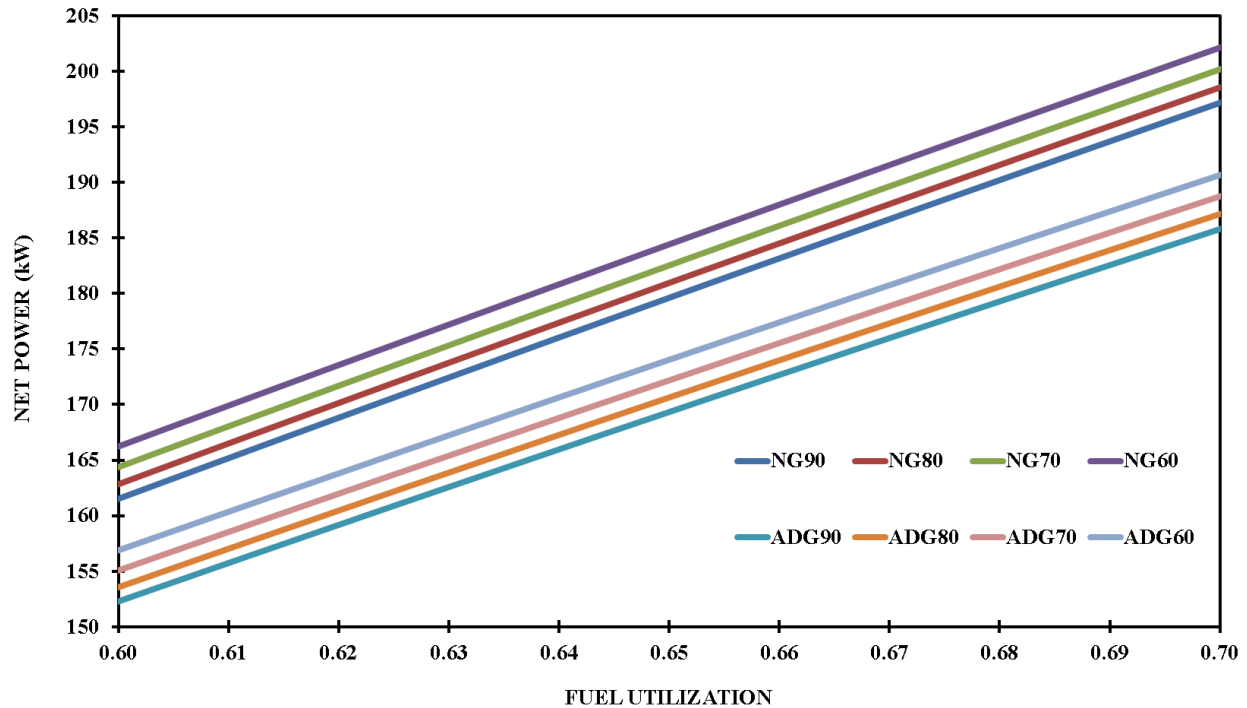


Figure 31. Net power for varying fuel utilizations for eight tri-generation cases

For greater clarity of the system performance, Figure 32 shows the net power produced for fuel utilizations between 0.6 and 0.7.



**Figure 32. Net power production for 0.6—0.7 fuel utilization**

The net power is directly affected by the relationships described for the gross power discussed in 6.4 Gross Power and parasitic loads in 6.5 Parasitic Loads. It should be noted that the parasitic load associated with the purification of ADG was not considered in this study, but does represent a notable fraction of the losses incurred by any system fueled by ADG or any other biogas. The following conclusions are true for a tri-generating MCFC:

- Net power increases with increasing fuel utilization for every modeled case.
- Net power is higher for natural gas operation than anaerobic digester gas operation. It should be noted that the parasitic load associated with the purification of ADG was not considered in this study, but does represent a notable fraction of the losses incurred by any system fueled by ADG or any other biogas.

- Net power increases with decreasing percentages of hydrogen recovery.

## 6.7 Hydrogen Production Rate

The hydrogen production rate for MCFC in “tri-generation mode” at varying fuel utilizations for each scenario is illustrated in Figure 33.

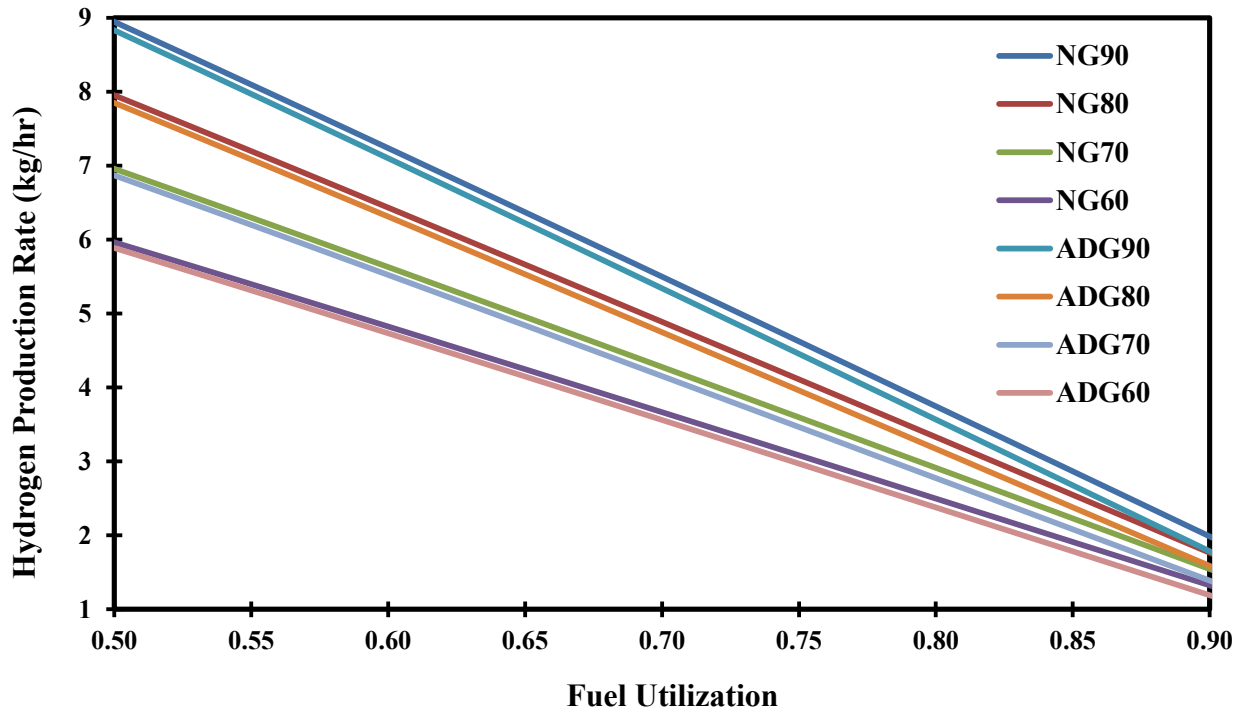


Figure 33. Hydrogen production rate for tri-generating MCFC at varying fuel utilizations



The fuel utilization dictates the amount of fuel consumed for power generation, leaving the remaining fuel available for export. Thus, the hydrogen production rate is explicitly a function of fuel utilization. Based on Figure 33 the following relationships are apparent:

- The hydrogen production rate increases with increasing percentages of hydrogen recovery.
- The hydrogen production rate decreases with increasing fuel utilization for every modeled case.
- The hydrogen production rate is higher for natural gas operation than anaerobic digester gas operation.

Lastly, the difference between hydrogen production rates for ADG and NG at the same hydrogen recovery percentage increases with increasing fuel utilization. The divergence occurs due to the decreasing availability of hydrogen at high fuel utilizations for the ADG-fueled tri-generation systems. Therefore, the hydrogen production rate for a tri-generating molten carbonate fuel cell system using anaerobic digester gas is increasingly less than using natural gas operation at higher fuel utilizations.

## 6.8 Waste Heat Availability

The available waste heat from the tri-generation fuel cell system at varying fuel utilizations for several scenarios is shown below in Figure 34.

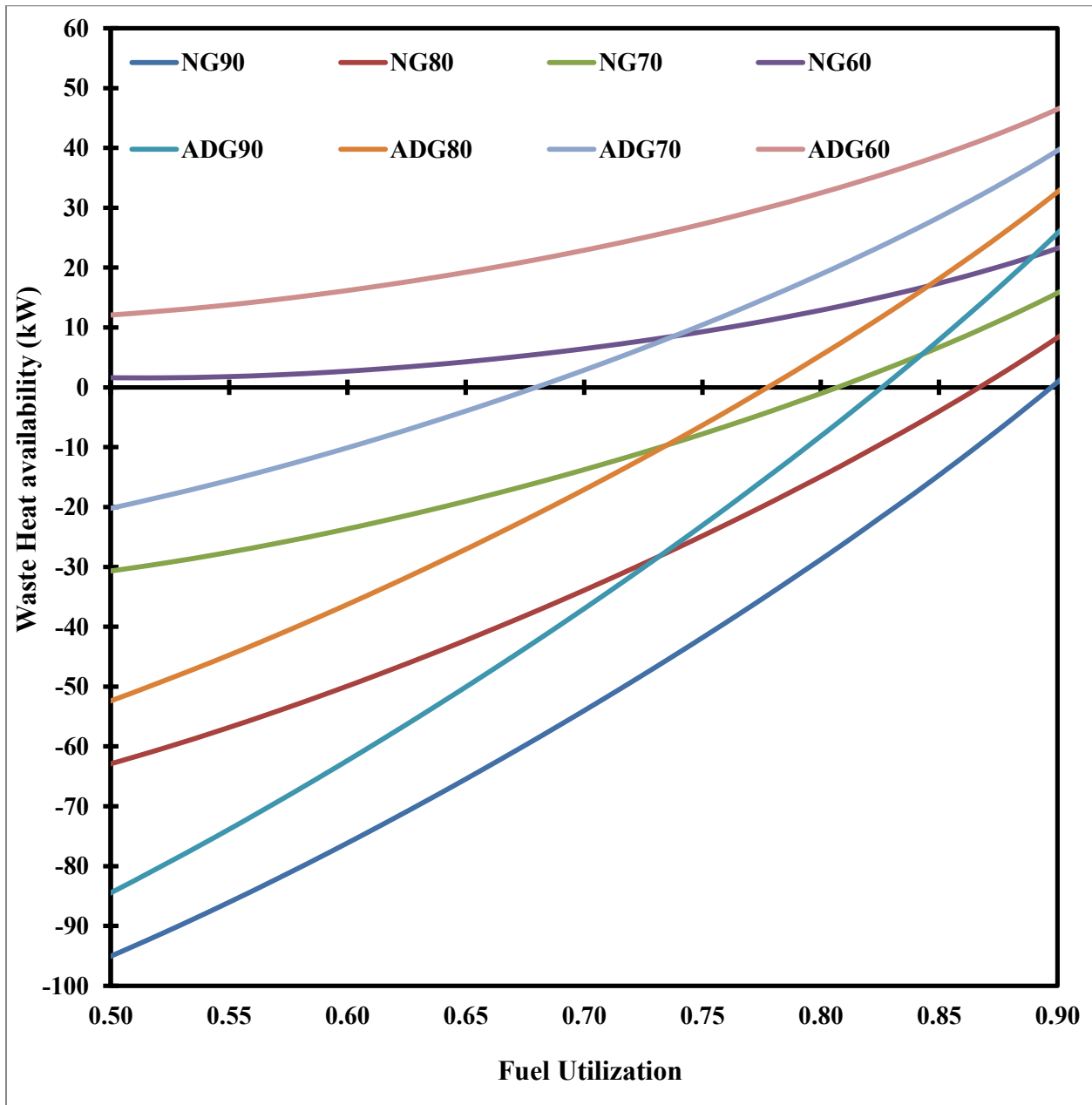


Figure 34. Available waste heat generated by tri-generating fuel cell system

The assessment of available waste heat is critical to the thermal management of a fuel cell system, especially a tri-generating fuel cell system. The electrochemical fuel cell reactions are

exothermic and must balance the endothermicity of internal SMR, as discussed in 4.3.1.2 Thermal Management of Fuel Cell Stack. Figure 34 is insightful since it provides a visual understanding of the fuel utilizations and hydrogen recovery percentages that will destabilize the thermal balance of the tri-generation fuel cell system. Negative values for waste heat availability are indicative of a fuel cell system that requires supplemental heat. The following ranges of operation in Table 41 should be observed to ensure the fuel cell system is thermally balanced or has excess waste heat available for other applications.

**Table 41. Range of fuel utilizations for thermally balancing tri-generation fuel cell system**

<b>Fuel</b>	<b>Hydrogen Recovery Percentage</b>	<b>Minimum Fuel Utilization for Waste Heat Availability</b>
Natural Gas	90	0.90
Natural Gas	80	0.87
Natural Gas	70	0.81
Natural Gas	60	ALL
Anaerobic Digester Gas	90	0.82
Anaerobic Digester Gas	80	0.78
Anaerobic Digester Gas	70	0.69
Anaerobic Digester Gas	60	ALL

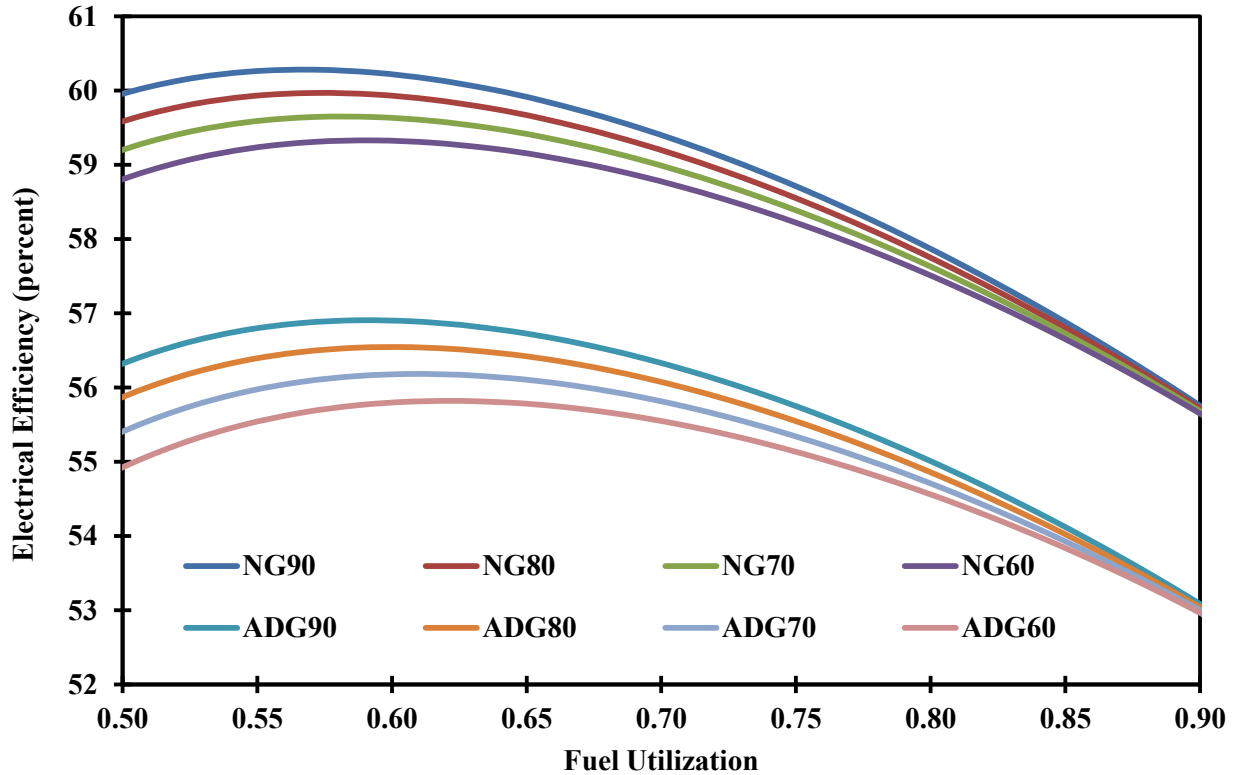
The following conclusions can be made based on data presented in Figure 34:

- The utilization of hydrogen for a fuel cell system is critical to its thermal balance. The majority of the heat in the system is generated from either the electrochemical oxidation of hydrogen in the fuel cell or combustion in the oxidizer, thus the export of hydrogen reduces the most substantial contribution to heat generation in the fuel cell system. Therefore, the waste heat availability for a tri-generation fuel cell system decreases with increasing percentages of hydrogen recovery.
- Heat generation via electrochemical oxidation of hydrogen is directly proportional to the fuel utilization factor. Thus, the waste heat availability for a tri-generation fuel cell system increases with increasing fuel utilization for every modeled case.
- The removal of hydrogen from the system reduces the availability of waste heat in the system. Since the hydrogen production rate for the ADG-fueled system is slightly lower than the NG-fueled MCFC system at the same hydrogen recovery percentage, the waste heat availability for the ADG case should be slightly higher than the NG scenario. That trend is apparent in Figure 34. However, there is a significant difference between the ADG and NG curves. The attributable factor is fuel composition. Methane composes over 98 percent of the natural gas simulated in this model. For every molecule of methane reformed, 4 molecules of hydrogen and one molecule of carbon dioxide are formed. Virtually all of the methane undergoes reformation, resulting in a hydrogen-rich reformat. Conversely, the reformat for the ADG-fueled MCFC is much more dilute due the lower methane concentration in ADG. Not only is there more hydrogen to remove for an NG-fueled system than an ADG-fueled system at the same hydrogen recovery percentage, but there is also a larger fraction of the material stream removed from the

system. The removal of a material stream with the potential for high quality heat recovery negatively affects the waste heat available to a system. Therefore, the waste heat availability for anaerobic digester gas operation is greater than natural gas operation for all fuel utilizations.

## 6.9 Electrical Efficiency

The electrical efficiency for MCFC in “tri-generation mode” at varying fuel utilizations for each scenario is illustrated in Figure 35.



**Figure 35. Electrical efficiency for each scenario for various fuel utilizations**

The expression for electrical efficiency for a tri-generating high-temperature fuel cell was provided as Equation (3-35) in 4.4 Efficiency of Tri-Generating High-Temperature Fuel Cell. The electrical efficiency of a system is proportional to net power exported from the system. It should be noted that the electrical efficiency of an ADG-fueled tri-generation MCFC system would be less than the values shown in Figure 35 for all fuel utilizations if the parasitic load associated with ADG purification is considered.

The optimal fuel utilization for the most efficient production of electricity is located at the maximum point of each curve in Figure 35. The curvature of the natural gas scenarios is similar to the trend apparent for the anaerobic digester gas cases, but the maximum point for the natural gas cases is at slightly lower fuel utilization value than the anaerobic digester gas scenarios. This

shift is due to the lower methane content of the ADG. The optimal fuel utilization for each modeled scenario is listed in Table 42 below.

**Table 42. Fuel utilization for optimal electrical efficiency**

<b>Fuel</b>	<b>Hydrogen Recovery Percentage</b>	<b>Fuel Utilization</b>
Natural Gas	90	0.57
Natural Gas	80	0.57
Natural Gas	70	0.57
Natural Gas	60	0.59
Anaerobic Digester Gas	90	0.59
Anaerobic Digester Gas	80	0.61
Anaerobic Digester Gas	70	0.61
Anaerobic Digester Gas	60	0.62

The following conclusions can be made based on data presented in Figure 35:

- The electrical efficiency for a tri-generation fuel cell system increases with increasing percentages of hydrogen recovery.

- The electrical efficiency for anaerobic digester gas operation is lower than natural gas operation for all fuel utilizations.
- The effect of hydrogen recovery on electrical efficiency decreases with increasing fuel utilization.

## 6.10 Hydrogen Production Efficiency

The hydrogen production efficiency for MCFC in “tri-generation mode” at varying fuel utilizations for each scenario is illustrated in Figure 36



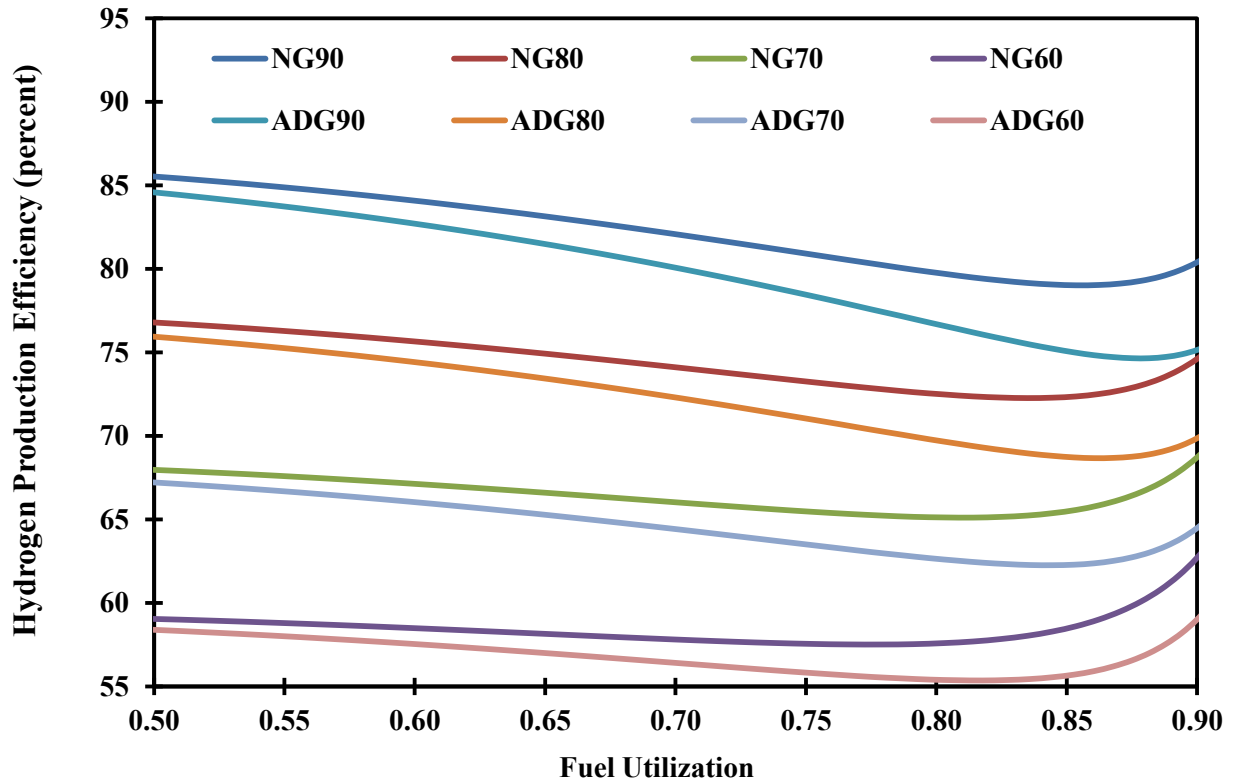


Figure 36. Hydrogen production efficiency for each scenario for various fuel utilizations

The expression for hydrogen production efficiency for a tri-generating high-temperature fuel cell was provided as Equation (3-34) in 4.4 Efficiency of Tri-Generating High-Temperature Fuel Cell. The utilization factor for a typical co-generating HTFC was set to 90 % and the combined cycle efficiency was assumed to be 60 % for the calculation of the hydrogen production efficiency. The hydrogen production efficiency of a system is proportional to hydrogen production rate and inversely proportional to the energy required for hydrogen purification. The optimal fuel utilization for the most efficient production of hydrogen is located at either the maximum or minimum fuel utilization modeled based on Figure 36. The optimal fuel utilization for each modeled scenario is listed in Table 43 below.

**Table 43. Fuel utilization for optimal hydrogen production efficiency**

<b>Fuel</b>	<b>Hydrogen Recovery Percentage</b>	<b>Fuel Utilization</b>
Natural Gas	90	0.5
Natural Gas	80	0.5
Natural Gas	70	0.9
Natural Gas	60	0.9
Anaerobic Digester Gas	90	0.5
Anaerobic Digester Gas	80	0.5
Anaerobic Digester Gas	70	0.5
Anaerobic Digester Gas	60	0.9

Referring to Figure 26, the HSU load for all cases is lowest at 0.9 fuel utilization. Also, the maximum hydrogen production rate for all cases is at 50 percent fuel utilization according to Figure 33. The optimal fuel utilization for natural gas and anaerobic digester gas at 80 and 90 percent hydrogen recovery is 0.5. In other words, an ADG or NG fueled tri-generation system with a set hydrogen recovery of 80 or 90 percent is exporting the most hydrogen per unit of energy expended on the separation of the hydrogen at 50 percent fuel utilization. Those results indicate that recovering the maximum amount of hydrogen available is the most efficient use of the large HSU loads associated with 80 and 90 percent hydrogen recovery. For the cases of natural gas and anaerobic digester gas operation at 60 percent hydrogen recovery, the maximum

fuel utilization of 90 percent is more efficient. The least amount of hydrogen can be recovered at 0.9 fuel utilization, thus the optimal hydrogen production for 60 % hydrogen recovery is at the minimum hydrogen production rate. Since the HSU load is proportional to hydrogen production rate, the minimum HSU load is at 0.9 fuel utilization. The hydrogen production efficiency for natural gas case at 70 percent hydrogen recovery is also optimal at 0.9 utilization based on the same reasoning. Since there less hydrogen in ADG, the 70 percent hydrogen recovery case produced hydrogen most efficiently at 0.5 fuel utilization rather than 0.9 seen in the natural gas scenario.

The following conclusions can be made based on data presented in Figure 36:

- The hydrogen production efficiency for a tri-generation fuel cell system increases with increasing percentages of hydrogen recovery.
- The hydrogen production efficiency for anaerobic digester gas operation is lower than natural gas operation for all fuel utilizations.
- The effect of hydrogen recovery on hydrogen production efficiency increases with increasing fuel utilization.

## 6.11 Combined Hydrogen and Power Efficiency

The combined hydrogen and power efficiency for MCFC in “tri-generation mode” at varying fuel utilizations for each scenario is illustrated in Figure 37.

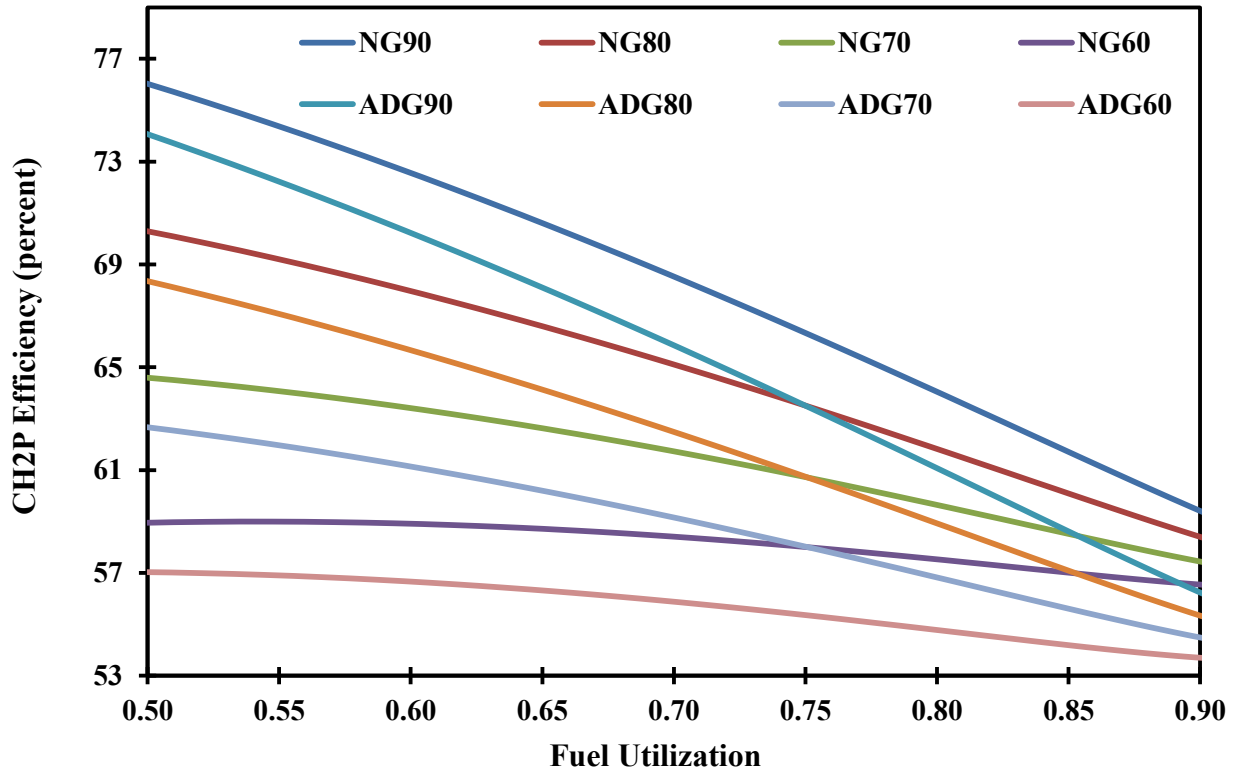


Figure 37 Combined hydrogen and power production efficiency for various fuel utilizations

The expression for combined hydrogen and power efficiency for a tri-generating high-temperature fuel cell was provided as Equation (3-33) in 4.4 Efficiency of Tri-Generating High-Temperature Fuel Cell. The optimal fuel utilization for the most efficient production of hydrogen and electricity is at 0.50 for all cases, except the tri-generation MCFC using natural gas case with 60 percent recovery has maximum combined hydrogen and power efficiency at 0.54 fuel utilization.

The following conclusions can be made based on data presented in Figure 37:

- The combined hydrogen and power efficiency for a tri-generation fuel cell system increases with increasing percentages of hydrogen recovery.
- The combined hydrogen and power for anaerobic digester gas operation is lower than natural gas operation for all fuel utilizations.
- The effect of hydrogen recovery on combined hydrogen and power efficiency decreases with increasing fuel utilization.

## Chapter 7:      **Discussion**

The results of eight parametric studies were discussed in Chapter 6: Model Evaluation. Table 44 below summarizes the optimal fuel utilizations found for waste heat availability and electrical, hydrogen production, and combined hydrogen and power efficiency.

**Table 44. Minimum Fuel utilization for optimal hydrogen production efficiency**

<b>Fuel</b>	<b>Hydrogen Recovery Percentage</b>	<b>Waste Heat Availability</b>	<b>Electrical Efficiency</b>	<b>Hydrogen Production Efficiency</b>	<b>CH<sub>2</sub>P Efficiency</b>
NG	90	0.90	0.57	0.5	0.5
NG	80	0.87	0.57	0.5	0.5
NG	70	0.81	0.57	0.9	0.5
NG	60	ALL	0.59	0.9	0.54
ADG	90	0.82	0.59	0.5	0.5
ADG	80	0.78	0.61	0.5	0.5
ADG	70	0.69	0.61	0.5	0.5
ADG	60	ALL	0.62	0.9	0.5

To properly characterize the system performance for different hydrogen recovery fractions and fuels, operating constrictions must be identified. The waste heat availability is the most

constricting parameter for scenarios with greater than 70 percent hydrogen recovery. Assuming supplemental heat is not available for the system, the minimum fuel utilization for a thermally-balanced system is equivalent to the absolute minimum operational fuel utilization. The optimal fuel utilization for each scenario will depend on the valued parameter. The following five parameters are most likely to be maximized if valued by the tri-generation fuel cell system operator:

1. **Hydrogen production rate:** this parameter should determine the operating fuel utilization if maximum hydrogen export is most valued
2. **Net power generation:** this parameter should determine the operating fuel utilization if maximum power export is most valued
3. **Electrical efficiency:** this parameter should determine the operating fuel utilization if the maximum electrical efficiency is valued more than the quantity of power exported
4. **Hydrogen production efficiency:** this parameter should determine the operating fuel utilization if hydrogen production efficiency is valued more than the quantity of hydrogen exported
5. **Maximum combined hydrogen and power efficiency:** this parameter should determine the operating fuel utilization if combined hydrogen and electrical efficiency is valued more than the quantity of hydrogen and power exported

The maximum hydrogen production rate always occurs at the lowest fuel utilization, which is 0.5 in this body of research. Since hydrogen production is inversely related to power generation, the maximum net power generated occurs at 0.9 fuel utilization. Since the hydrogen production rate and net power generation decrease and increase linearly with increasing fuel utilization respectively, the limitation of waste heat availability is straightforward. For instance, a tri-generation MCFC system operating on natural gas with 70 percent hydrogen recovery should operate at 0.81 fuel utilization or greater to be thermally-balanced. The maximum hydrogen production rate for that system is at the lowest operating fuel utilization possible, therefore the maximum hydrogen production will coincide with the minimum operating fuel utilization for a thermally-balanced tri-generation MCFC system. Since the net power generation is maximized at 0.9 fuel utilization for every scenario and every case is thermally-balanced at 0.9, the optimum operating fuel utilization for net power generation remains at 90 percent. The electrical and hydrogen production efficiency do not linearly increase or decrease with increasing fuel utilization, so the maximum efficiency may not occur at the minimum fuel utilization for a thermally-balanced system. The combined hydrogen and power efficiency does decrease for increasing fuel utilization, so the minimum fuel utilization for a thermally-balanced system coincides with the fuel utilization associated with the maximal combined hydrogen and power efficiency. The optimal fuel utilization for each thermally-balanced MCFC system tri-generating hydrogen, electricity, and heat valuing a specific parameter is shown in the Table 45.



**Table 45. Optimal operating fuel utilization for different system outcomes**

<b>Fuel</b>	<b>Hydrogen Recovery Percentage</b>	<b>Hydrogen Production Rate</b>	<b>Net Power Generation</b>	<b>Electrical Efficiency</b>	<b>Hydrogen Production Efficiency</b>	<b>CH<sub>2</sub>P Efficiency</b>
NG	90	0.90	0.90	0.90	0.90	0.90
NG	80	0.87	0.90	0.87	0.87	0.87
NG	70	0.81	0.90	0.81	0.90	0.81
NG	60	0.50	0.90	0.59	0.90	0.54
ADG	90	0.82	0.90	0.82	0.82	0.82
ADG	80	0.78	0.90	0.78	0.78	0.78
ADG	70	0.69	0.90	0.69	0.69	0.69
ADG	60	0.50	0.90	0.62	0.90	0.50

The operating fuel utilization range for each scenario is summarized in Table 46.

**Table 46. Range of fuel utilizations for modeled scenarios**

<b>Fuel</b>	<b>Hydrogen Recovery Percentage</b>	<b>Operating Fuel Utilization Range</b>
Natural Gas	90	0.90
Natural Gas	80	0.87—0.90
Natural Gas	70	0.81—0.90
Natural Gas	60	0.50—0.90
Anaerobic Digester Gas	90	0.82—0.90
Anaerobic Digester Gas	80	0.78—0.90
Anaerobic Digester Gas	70	0.69—0.90
Anaerobic Digester Gas	60	0.50—0.90

The tri-generation MCFC system operating on natural gas with 90 percent hydrogen recovery is the only scenario where the optimal fuel utilization is the same for all parameters. It is apparent that the range of operational fuel utilizations increases with decreasing hydrogen recovery percentages. For both fuels, 60 percent hydrogen recovery allows for the most flexible operation.

The operating fuel utilization range for each scenario was identified in Table 46. The tri-generation of hydrogen, electricity, and heat for the operating fuel utilization range for each scenario is listed in Table 47.

**Table 47. Hydrogen, electricity, and heat generation for operating fuel utilization range**

<b>Fuel</b>	<b>Hydrogen Recovery Percentage</b>	<b>Operating Fuel Utilization Range</b>	<b>Hydrogen Production Rate (kg/hr)</b>	<b>Net Power Generation (kW)</b>	<b>Waste Heat Availability (kW)</b>
NG	90	0.90	1.88	265	2.98
NG	80	0.87—0.90	2.23—1.67	255—266	0.869—9.94
NG	70	0.81—0.90	2.79—1.46	238—267	1.05—17.0
NG	60	0.50—0.90	6.00—1.25	127—270	1.63--24.1-
ADG	90	0.82—0.90	3.08—1.73	226—252	0.38—27.8
ADG	80	0.78—0.90	3.38—1.50	213—254	2.11—34.3
ADG	70	0.69—0.90	4.02—1.40	187—256	4.25—39.5
ADG	60	0.50—0.90	5.92—1.19	119—258	12.0—46.5

## Chapter 8:      **Summary**

A steady-state molten carbonate fuel cell 0-D model was constructed in Aspen Plus<sup>®</sup>. The model simulated the tri-generation of hydrogen, electricity, and heat using a Direct FuelCell<sup>®</sup> molten carbonate fuel cell technology developed by FuelCell Energy. The simulation incorporated operating data from an actual installation. The internal reforming molten carbonate fuel cell model was uniquely integrated with hydrogen concentrating and purifying equipment to facilitate tri-generation of hydrogen, electricity, and heat.

The DFC<sup>®</sup> molten carbonate fuel cell co-producing hydrogen and electricity was the first model verified. The model simulating the DFC<sup>®</sup> molten carbonate fuel cell tri-generating hydrogen, electricity, and heat operating on 1) natural gas and 2) anaerobic digester gas was verified using data collected from the existing installation.

A parametric study for the fuel utilization and recovered hydrogen were performed and presented. Thus, the tri-generation system performance was characterized for two different fuels, natural gas and anaerobic digester gas, and hydrogen recoveries.

## Chapter 9:      **Conclusions**

This research led to the following conclusions regarding the performance of an internal reforming molten carbonate fuel cell system that tri-generates hydrogen, electricity, and heat fueled by 1) natural gas and 2) anaerobic digester gas:

- **Internal reforming fuel cell models in Aspen Plus<sup>®</sup> should be discretized**

Aspen Plus<sup>®</sup> does not contain built-in functions that can model fuel cell electrochemical reactions. Hence, simulating the SMR, WGS, and electrochemical reactions for a steady-state internal reforming fuel cell in Aspen Plus<sup>®</sup> is challenging due to the reactions that simultaneously occur, the interconnectedness of those reactions, and the inability for Aspen Plus to model electrochemical reactions. To artificially restore the interconnectedness of the electrochemical, SMR, and WGS reactions, iterations of the decoupled modeling strategy minimized the gross error associated with a single iteration or “single-stage reactor.” This new strategy essentially led to the discretization of the anode, which resulted in more accurately predicted the anode exhaust composition of a DFC<sup>®</sup> fuel cell than single-stage anode model.

- **Waste heat availability is a limiting parameter for the tri-generating MCFC system at 70 percent hydrogen recovery and greater**

The export of hydrogen removes heat from the tri-generation MCFC system, thus thermally-balancing the system is an important consideration. The waste heat availability is a parameter that indicates if the tri-generation molten carbonate fuel cell system is thermally-balanced. The fuel utilization associated to the very minimum waste heat needed to thermally-balance became the most significant limitation to the operating fuel utilization range for cases that recovered over 70 percent of the hydrogen available for export. For scenarios where 60 percent or less of the hydrogen in the anode exhaust was recovered, the tri-generation system was thermally-balanced for fuel utilizations between 0.5 to 0.9 at a current density of  $1200 \text{ A/m}^2$ , which indicates that waste heat availability did not limit the operating fuel utilization range.

- **Tri-generating MCFC system is less efficient when fueled by anaerobic digester gas**

The hydrogen, electrical, and combined hydrogen and power efficiency for a molten carbonate fuel cell tri-generating hydrogen, electricity, and heat is lower for ADG operation than NG operation for fuel utilizations between 0.5 to 0.9 at a current density of  $1200 \text{ A/m}^2$ . The lower performance is attributed to the lower Nernst and fuel cell operating voltage, hydrogen production rate, gross power for ADG operation in relation to natural gas.

- **Tri-generating MCFC system is more efficient at higher hydrogen recovery percentages**

For both fuels at fuel utilizations between 0.5 to 0.9 at a current density of 1200 A/m<sup>2</sup>, larger hydrogen recovery percentages result in higher Nernst potential and fuel cell operating voltages; gross and net power; hydrogen production rates; and electrical, hydrogen production, and combined hydrogen and power efficiencies.

- **A thermally-balanced tri-generating MCFC system must operate within a specific fuel utilization range depending on fuel type and hydrogen recovery percentages**

The operating fuel utilization range at a current density of 1200 A/m<sup>2</sup> for a thermally-balanced tri-generation MCFC system operating on natural gas is: 0.90 for a hydrogen recovery of 90 percent; 0.87—0.90 for a hydrogen recovery of 80 percent; 0.81—0.90 for a hydrogen recovery of 70 percent; and 0.5—0.90 for a hydrogen recovery of 60 percent.

The operating fuel utilization range at a current density of 1200 A/m<sup>2</sup> for a thermally-balanced tri-generation MCFC system operating on anaerobic digester gas is: 0.82—0.90 for a hydrogen recovery of 90 percent; 0.78—0.90 for a hydrogen recovery of 80 percent; 0.69—0.90 for a hydrogen recovery of 70 percent; and 0.5—0.90 for a hydrogen recovery of 60 percent.

## **Chapter 10: Recommendations for Future Work**

The following are recommendations for future work on this research topic:

- Several complete operational data sets from the existing installation would further refine the steady-state model developed.
- There is a need for further characterization of the polarization losses for the DFC<sup>®</sup> molten carbonate fuel cell in “tri-generation mode.”
- The high and low temperature water-gas shift reactor models should be further developed to better predict the performance of the water-gas shift reactors installed.
- There is a need for information regarding the practical operational constraints for the fuel cell and supporting equipment.
- Other hydrogen separation technologies should be incorporated into the system design, especially separation technologies more compatible with the operating conditions of the fuel cell.



## BIBLIOGRAPHY

- [1] Leo, A. "Stationary Fuel Cell Power Systems with Direct FuelCell Technology Tackle Growing Distributed Baseload Power Challenge." FuelCell Energy, Inc.
- [2] Willis, H. L. and Scott, W. G. *Distributed Power Generation: Planning and Evaluation*. NY: Marcel Dekker, Inc., 2000.
- [3] Cook, B. "An Introduction to Fuel Cells and Hydrogen Technology." 2001. Heliocentris.
- [4] Hirst, E. and Brendan, K. "Ancillary Services." 1996. Oak Ridge National Laboratory Oak Ridge.
- [5] Leo, A. and Pais, C. "Biogas Applications for Molten Carbonate Fuel Cells." 2010. Costa Mesa, CA: Proceedings of the International Colloquium on Environmentally Preferred Advanced Power Generation. FuelCell Energy, Inc.
- [6] "Business Rate Summary." June 1, 2008. Southern California Edison. Accessed June 25, 2010. <[http://www.sce.com/NR/rdonlyres/6B523AB1-244D-4A8F-A8FE-19C5E0EFD095/0/090202\\_Business\\_Rates\\_Summary.pdf](http://www.sce.com/NR/rdonlyres/6B523AB1-244D-4A8F-A8FE-19C5E0EFD095/0/090202_Business_Rates_Summary.pdf)>
- [7] "Fact Sheet—Wastewater Sludge: A New Resource for Alternative Energy and Resource Recovery." Water Environment Research Foundation. Accessed June 25, 2010. <[http://www.werf.org/am/template.cfm?section=Search\\_Research\\_and\\_Knowledge\\_Areas&template=/cm/ContentDisplay.cfm&ContentID=7008](http://www.werf.org/am/template.cfm?section=Search_Research_and_Knowledge_Areas&template=/cm/ContentDisplay.cfm&ContentID=7008)>
- [8] "Arab Oil Embargo and United States Pressure against Chile: Economic and Political Coercion and the Charter of the United Nations." The Brosche, Hartmut 7 Case W. Res. J. Int'l L. 3 (1974-1975)
- [9] "Basic Research Needs for the Hydrogen Economy: Report of the Basic Energy Sciences Workshop on Hydrogen Production, Storage, and Use." Argonne National Laboratory. Feb. 2004. 2<sup>nd</sup> ed. Report.
- [10] Leal, E. M. and Brouwer, J. "A Thermodynamic Analysis of Electricity and Hydrogen Co-Production Using a Solid Oxide Fuel Cell." *Journal of Fuel Cell Science and Technology*. 3(2006)137-144
- [11] "Vision for Rollout of Fuel Cell Vehicles and Hydrogen Fuel Stations." 2008. California Fuel Cell Partnership.
- [12] Patel, P. "Demonstration of a Fuel Cell Power Plant for Co-production of Electricity and Hydrogen." FuelCell Energy.
- [13] Air Products and Chemicals, Inc. *Liquid & Bulk Gases: Hydrogen*. Accessed June 29, 2010. <[http://www.airproducts.co.uk/bulkgases/hydrogen\\_industry.htm](http://www.airproducts.co.uk/bulkgases/hydrogen_industry.htm)>.

- 
- [14] “Thrust Area: Co-production of Hydrogen and Electricity.” FuelCell Energy, Inc.
- [15] Leal, E.M. and Brouwer, J. “Production of Hydrogen using High-Temperature Fuel Cell: Energy and Exergy Analysis”, *18th International Congress of Mechanical Engineering*, November 6-11, 2005.
- [16] Climate Lab. *Hydrogen Fuel Cell Diagram*. Accessed February 10, 2012.  
<<http://climatelab.org/@api/deki/files/233/=fuelcell.jpg>>
- [17] O'Hayre, R., Cha, S., Colella, W., and Prinz, F.B. *Fuel Cell Fundamentals*. 2 ed. New Jersey: John Wiley & Sons, Inc., 2009.
- [18] Silberberg, M.S. *Chemistry: The Molecular Nature of Matter and Change*. 4 ed. New York: McGraw-Hill, 2006.
- [19] Office of Fossil Energy. July, 23, 2010. *Today's Hydrogen Production Industry*. U.S. Department of Energy. Accessed: June 30, 2012:  
<<http://www.fossil.energy.gov/programs/fuels/hydrogen/currenttechnology.html>>.
- [20] Energy Efficiency and Renewable Energy. November 20, 2012. *Hydrogen Production: Current Technology—Natural Gas Reforming*. U.S. Department of Energy. Accessed June 1-December 20, 2012].  
<[http://www1.eere.energy.gov/hydrogenandfuelcells/production/natural\\_gas.html](http://www1.eere.energy.gov/hydrogenandfuelcells/production/natural_gas.html)> [accessed June 1-December 20, 2012].
- [21] Larminie, J. and Dicks, A. *Fuel Cell Systems Explained*. 2 ed. England: John Wiley and Sons Ltd., 2003.
- [22] van Beurden, P. “On the Catalytic Aspects of Steam-Methane Reforming: A literature Survey.” Technical Report. Netherlands. ECN. December 2004.
- [23] Energy Efficiency and Renewable Energy. November 20, 2012. *Hydrogen Production: Basics-- Centralized vs Distributed Production*. U.S. Department of Energy. Accessed July 6, 2012. <[http://www1.eere.energy.gov/hydrogenandfuelcells/production/central\\_distributed.html](http://www1.eere.energy.gov/hydrogenandfuelcells/production/central_distributed.html)>.
- [24] The Hydrogen Economy: Opportunities, Costs, Barriers, and R&D Needs. National Academies Press (published by). Authors: Committee on Alternatives and Strategies for Future Hydrogen Production and Use, National Research Council. 2004. Published in Washington, D.C.
- [25] Ruettinger, W. F. and Ilinich, O. (2005) 'Water Gas Shift Reaction (WGSR)', *Encyclopedia of Chemical Processing*, 1: 1, 3205 — 3215
- [26] Miller, Q. M., Stocker, J. "Selection of a hydrogen separation process." NPRA Annual Meeting held March 19-21, 1989.
- [27] Baker, B.S. and Ghezal-Ayagh, H.G. Jul. 30, 1985. “Fuel Cell System.” US 4,532,192. 429/19.

- 
- [28] Ghezal-Ayagh, H. and Jahnke, F.C. Feb. 4, 2010. "Fuel Cell Power Production System with an Integrated Hydrogen Utilization Device." US 2010/0028730 A1. 429/34.
- [29] Jahnke, F.C., Farooque, M., Ghezal-Ayagh, H. Feb. 25, 2010. "High-efficiency Dual-stack Molten Carbonate Fuel Cell System" US 2010/0047641 A1. 429/20.
- [30] Jahnke, F.C. and Parab, S.C. Jun. 13, 2006. "Fuel Cell System with Recycle of Anode Exhaust Gas." UA 7,060,382 B2. 429/34.
- [31] Vollmar, H., Edelmann, W., Schrepfer, W., Nolscher, C. Dec. 19, 2000. Method for Operating a High-Temperature Fuel Cell Installation, and a High-Temperature Fuel Cell Installation. U.S. 6, 162, 556. 429/17.
- [32] Margalef, P., Brown, T., Brouwer, J., Samuelson, S. "Conceptual design and configuration performance analyses of polygenerating high temperature fuel cells." *International Journal of Hydrogen Energy*. **36(16)**, 10044–10056 (2011).
- [33] Verda, V. and Nicolin, F. "Thermodynamic and economic optimization of a MCFC-based hybrid system for the combined production of electricity and hydrogen." *International Journal of Hydrogen Energy*. 35,794-806, (2010).
- [34] Verda, V. and Nicolin, F. "Lifetime optimization of a molten carbonate fuel cell power system coupled with hydrogen production." *Energy*. 36, 2235-2241, (2011).
- [35] Verda, V. and Nicolin, F. "Optimal design and operation of a biogas fuelled MCFC system integrated with an anaerobic digester." *Energy*. 47, 150-157, (2012).
- [36] Molburg, J.C. and Doctor, R.D. "Hydrogen from Steam-Methane Reforming with CO<sub>2</sub> Capture." 20<sup>th</sup> Annual International Pittsburgh Coal Conference. Sept 15-19, 2003.
- [37] Leo, A. and Pais, C. "Biogas Applications for Molten Carbonate Fuel Cells." Feb, 2010. Costa Mesa, CA: Proceedings of the International Colloquium on Environmentally Preferred Advanced Power Generation. FuelCell Energy, Inc.
- [38] Department of Energy. Sept. 15, 2011. "Fuel Station of the Future—Innovative Approach to Fuel Cell Technology Unveiled in California." <<http://energy.gov/articles/fuel-station-future-innovative-approach-fuel-cell-technology-unveiled-california>>
- [39] Lukas, M.D., Lee, K.Y., and Ghezal-Ayagh, H. "An Explicit Dynamic Model for Direct Reforming Carbonate Fuel Cell Stack." *IEEE Transactions on Energy Conversion*. 16.3 (2001) 289-295
- [40] Lukas, M.D., Lee, K.Y., and Ghezal-Ayagh, H. "Modeling and cycling control of carbonate fuel cell power plants." *Control Engineering Practice*. 10 (2002) 197-206.

- 
- [41] Ghezel-Ayagh, H., McInerney, J., Venkataraman, R., Farooque, M., Sanderson, R. "Development of Direct Carbonate Fuel Cell Systems for Achieving Ultrahigh Efficiency." *Journal of Fuel Cell Science and Technology*. 8(3),031011(2011).
- [42] Katikaneni, S., Yuh, C., Abens, S., and Farooque, M. "The direct carbonate fuel cell technology: advances in multi-fuel processing and internal reforming." *Catalysis Today*. 77, 99-106 (2002).
- [43] Patel, P., Dharia, E., and Maru, H. Jan. 28, 1986. "Fuel Cell Employing Non-uniform Catalyst." U.S. Patent 4, 567,117. 429/19.
- [44] Kivisaari, T., Bjornbom, P., Sylwan, C. "Studies of biomass fuelled MCFC systems." *Journal of Power Sources*. 104, 115–124 (2002).
- [45] Li, M., Rao, A.D., Brouwer, J., Samuelsen, G.S. "Design of highly-efficient coal-based integrated gasification fuel cell power plants". *Journal of Power Sources*. 195, 5707–5718 (2010).
- [46] De Simon, G., Parodi, F., Fermeglia, M., Taccani, R. "Simulation of process for electrical energy production based on molten carbonate fuel cells." *Journal of Power Sources*. 115, 210–218 (2003).
- [47] Yoshiba, F., Morita, H., Yoshikawa, M., Mugikura, Y., Izaki, Y., Watanabe, T., Komoda, M., Masuda, Y., and Zaima, N. "Improvement of electricity generating performance and life expectancy of MCFC stack by applying Li/Na carbonate electrolyte: Test results and analysis of 0.44 m<sup>2</sup>/10-kW-and 1.03 m<sup>2</sup>/10kW-class stack." *Journal of Power Sources*. 128, 152-164 (2004).
- [48] Hilmi, A., Yuh, C., Farooque, M. "Carbonate fuel cell matrix and electrolyte developments." *The Electrochemical Society Transactions*. 41 (11), 65-73 (2012).
- [49] Hilmi, A., Yuh, C., Farooque, M. Jan. 26, 2012. "High Performance Electrolyte for Molten Carbonate Fuel Cells" US 2012/0021328 A1. 429/478.
- [50] Lee, C., Yamada, K., Nishina, T., Uchida, I. "In situ NiO dissolution behavior in (Li + Na)CO<sub>3</sub> melts under pressurized oxidant gas atmospheres." *Journal of Power Sources*. 62 (1), 145–147, (1996).
- [51] Antolini, E. "The stability of molten carbonate fuel cell electrodes: A review of recent improvements." *Applied Energy*. 88 (12), 4274–4293, (2011).
- [52] Peelen, W.H.A., Hemmes, K., de Wit, J.H.W. "Diffusion constants and solubility values of Co<sup>2+</sup> and Ni<sup>2+</sup> in Li/Na and Li/K carbonate melts." *Electrochimica Acta*. 42 (15), 2389–2397 (1997).
- [53] US Drive. "Hydrogen Delivery Technical Team Roadmap." June 2013.

- 
- [54] Heydorn, E.C., Patel, P., and Jahnke, F. "Development of a Renewable Hydrogen Energy Station." Feb, 2010. Costa Mesa, CA: Proceedings of the International Colloquium on Environmentally Preferred Advanced Power Generation. Air Products and Chemicals, Inc. and FuelCell Energy, Inc.
- [55] Margalef, P., Brown, T., Brouwer, J., Samuelsen, S. "Efficiency of poly-generating high temperature fuel cells." *Journal of Power Sources*. **196**, 2055–2060 (2011).
- [56] Subramanian, N., Haran, B.S., White, R.E., and Nopov, B.N. "Fuel Cell Mathematical Model of a MCFC." *Journal of The Electrochemical Society*. **150** (10) A1360-A1367 (2003).
- [57] Bosio, B., Costamagna, P., Parodi, F. "Modeling and experimentation of molten carbonate fuel cell reactors in a scale-up process." *Chemical Engineering Science*. **54** 2907-2916 (1999).
- [58] Morita, H., Komoda, M., Mugikura, Y., Izaki, Y., Watanabe, T., Masuda, Y., Matsuyama, T., "Performance Analysis of Molten Carbonate Fuel Cell using a Li/Na Electrolyte," *Journal of Power Sources*. **112** 509-518 (2002).
- [59] Munoz de Escalona, J.M., Sanchez, D., Chacartegui, R., Sanchez, T. "A step-by-step methodology to construct a model of performance of molten carbonate fuel cells with internal reforming," *International Journal of Hydrogen Energy*. **36** 15739-15751 (2011).